

**Low-noise modelocked lasers: pulse dynamics, feedback  
control, and novel actuators**

by

**Chien-Chung Lee**

B.S., National Taiwan University, 2007

A thesis submitted to the  
Faculty of the Graduate School of the  
University of Colorado in partial fulfillment  
of the requirements for the degree of  
Doctor of Philosophy  
Department of Physics

2015

This thesis entitled:  
Low-noise modelocked lasers: pulse dynamics, feedback control, and novel actuators  
written by Chien-Chung Lee  
has been approved for the Department of Physics

---

Thomas R. Schibli

---

Judah Levine

Date \_\_\_\_\_

The final copy of this thesis has been examined by the signatories, and we find that both the content and the form meet acceptable presentation standards of scholarly work in the above mentioned discipline.

Lee, Chien-Chung (Ph.D., Physics)

Low-noise modelocked lasers: pulse dynamics, feedback control, and novel actuators

Thesis directed by Associate Professor Thomas R. Schibli

Modelocked lasers combined with phase-locking techniques have revolutionized optical clocks and precision measurements. The basic but powerful technique that has driven these advances is feedback control, which rids a laser's output of phase or timing fluctuations. Ideally the ultimate noise level is determined by the coherence of external references. In practice, the effectiveness of this active stabilization relies on the available loop gain and bandwidth, both of which not only depend on the properties of the actuator but also on the complex dynamics of pulse evolution, gain-photon coupling, and cross-talk between actuators. In this Thesis, both the pulse dynamics and the actuator aspects of achieving low-noise level are discussed. In particular, a new type of high-bandwidth cavity loss modulator based on graphene is described. A record low-noise fiber frequency comb laser enabled by this new actuator technology is demonstrated with the graphene modulator. The pulse dynamics is analyzed in low-noise settings, which is low intracavity dispersion and nonlinearity. Specifically, an intrinsic power oscillation, arising from the interaction between a solitary pulse and continuum, is studied theoretically and experimentally, and its impact on the noise transfer properties of the laser is studied.

## Contents

### Chapter

<b>1</b>	Introduction	<b>1</b>
<b>2</b>	Basics of modelocking and noise	<b>5</b>
2.1	Rate equations: coupling between gain and photon . . . . .	6
2.2	Linearized model and relaxation oscillation . . . . .	7
2.3	Pulse formation: introducing time-dependent loss . . . . .	9
2.4	Modelocking: Stability . . . . .	10
2.5	Modelocking: Haus master equation . . . . .	11
2.6	Modelocking: Soliton perturbation theory . . . . .	13
2.7	Noise in modelocked lasers: Haus-Mecozzi model . . . . .	15
<b>3</b>	Graphene as a saturable absorber for modelocking	<b>19</b>
3.1	Overview of saturable absorbers . . . . .	20
3.2	Why use graphene? . . . . .	22
3.3	Band structure of graphene . . . . .	22
3.4	Linear absorption in graphene . . . . .	25
3.4.1	Theoretical background . . . . .	25
3.4.2	Sample preparation and characterization . . . . .	27
3.5	Saturable absorption of graphene . . . . .	30
3.5.1	Experimental setup: differential transmission and pump probe . . . . .	30

3.5.2	Results and discussion . . . . .	32
3.5.3	Saturable absorption in chemically-doped graphene . . . . .	35
3.6	Optical damage of graphene . . . . .	37
3.7	Modelocking of an Er:Yb:glass laser with graphene . . . . .	37
3.8	Conclusion . . . . .	39
<b>4</b>	<b>Graphene as an electro-optic modulator</b>	<b>41</b>
4.1	Motivation . . . . .	41
4.2	Physics of electro-absorption modulation in graphene . . . . .	42
4.3	Device implementation . . . . .	44
4.3.1	Design . . . . .	44
4.3.2	Fabrication . . . . .	45
4.3.3	Characterization . . . . .	47
4.4	Integration with a III-V semiconductor saturable absorber mirror . . . . .	49
4.4.1	Motivation . . . . .	49
4.4.2	Fabrication and characterization . . . . .	50
4.5	Conclusion . . . . .	52
<b>5</b>	<b>Stabilization of frequency comb with a graphene modulator</b>	<b>54</b>
5.1	Theoretical background: Transfer functions . . . . .	55
5.2	Experimental setup: Tm: fiber laser . . . . .	57
5.3	Experimental results: phase locking of carrier-envelope-offset frequency . . . . .	58
5.4	Conclusion . . . . .	60
<b>6</b>	<b>Laser dynamics: backaction of continuum on soliton and its implications on the transfer function of a modelocked laser</b>	<b>61</b>
6.1	Motivation . . . . .	61
6.2	Theoretical background . . . . .	62

6.3	Analytic approach . . . . .	63
6.4	Numerical simulation . . . . .	67
6.5	Experiemental results . . . . .	69
6.6	Conclusion . . . . .	70
 <b>Bibliography</b>		<b>71</b>
 <b>Appendix</b>		
<b>A</b>	Chemical vapor deposition of graphene	<b>81</b>
<b>B</b>	Raman spectra of graphene	<b>84</b>

## Figures

### Figure

2.1	Noise transfer pathways from the input to the output in a modelocked laser . . . . .	17
3.1	Graphene's honeycomb lattice and its reciprocal lattice . . . . .	23
3.2	Band structure of graphene . . . . .	24
3.3	Changes to graphene's linear absorption due to doping . . . . .	26
3.4	Scanning electron microscope image of graphene domains and boundaries. . . . .	27
3.5	Transmission spectra of doped graphene as a function of photon energy. . . . .	29
3.6	Differential transmission setup for measuring saturable absorption . . . . .	31
3.7	Degenerate pump probe setup for measuring carrier dynamics in graphene on a transparent substrate . . . . .	32
3.8	Saturable absorption and recovery dynamics in graphene. . . . .	33
3.9	Saturable absorption of graphene at different doping levels . . . . .	36
3.10	Photograph and microscope image of a graphene saturable absorber mirror. . . . .	38
3.11	Laser cavity and optical spectrum of a modelocked Er:Yb:glass laser by using a graphene saturable absorber mirror. . . . .	39
4.1	Concept of tuning of the optical absorption of graphene by electric field-gating. . . .	43
4.2	Graphene modulator: sketch of the device and plot of electric fields in the thin film structure. . . . .	46

4.3	Graphene modulator: a microscopic image and two dimensional heat map of modulation . . . . .	48
4.4	Frequency response of the graphene modulator . . . . .	49
4.5	Hybrid III-V-graphene device for modelocking and noise suppression: device structure, saturable absorption, and carrier relaxation dynamics. . . . .	51
4.6	Frequency response of the graphene modulator . . . . .	52
5.1	Experimental setup of a Tm: fiber laser for the demonstration of comb stabilization with a graphene modulator . . . . .	57
5.2	Comparison of the Bode plots of pump and loss modulation . . . . .	58
5.3	Power spectral density of the phase-locked carrier-envelope-offset frequency and the integrated phase noise. . . . .	59
6.1	Transfer functions of pump power modulation to output power including the back action of continuum back onto the soliton in the case of GF and TPA . . . . .	68
6.2	Experimental and simulated transfer functions of pump power modulation to output power. . . . .	69
A.1	Chemical vapor deposition system for growing monolayer graphene . . . . .	82
B.1	Raman spectrum of graphene: G, D, and 2D transition. . . . .	85
B.2	Raman spectra of graphene: experimental results . . . . .	86



# Chapter 1

## Introduction

Modelocked lasers, which are lasers that generate many highly coherent teeth in the frequency domain and at the same time extremely short pulses in the time domain, have been an indispensable tool for not only fundamental science [1–4] but also for industrial applications [5–7]. Its high coherence between frequency modes descends from the inner workings of pulse formation and dynamics [8,9]. Armed with radio-frequency phase locking techniques, modelocked lasers can further transform into a powerful tool known as the optical frequency comb, which acts as a gearbox that links a radio-frequency oscillator to an optical one. [10–15].

The noise that is centrally concerned with in a frequency comb is the phase or frequency jitter in its mode spacing (pulse repetition rate) and offset frequency (field repetition rate). Noise in intensity or power may be of concern as well for some applications [16,17]. The noise sources can be categorized by their origin: classical and quantum. Classical noise sources, such as acoustic and vibrational interference or thermal drift, tend to dominate at low frequencies, while quantum fluctuations, arising from spontaneous emission and cavity loss, can be revealed at high frequencies.

The free-running noise, either classical or quantum, can be actively suppressed with feedback control. This basic but powerful technique works as the following. First, the output of a modelocked laser is compared to a stable reference such as a narrow-linewidth laser or a low-noise microwave oscillator. Next, the comparison is transformed into an error signal and then filtered and amplified, after which it is sent to the driver for the control knobs of a mode-locked laser. The control knobs are parameters such as the pump power, the length of the laser cavity, or the

tilt of a laser cavity mirror. These macroscopic knobs are used to suppress the noise, provided that the closed loop gain is high enough. Very effective noise suppression has been shown for continuous-wave lasers [18, 19].

The success of the seemingly simple feedback control depends on a number of aspects. Firstly, the free-running state of a laser is predominantly determined by how it is designed and constructed. For low-noise purposes, low cavity loss, short pulses, and high intracavity pulse energy are the top priorities if one wants to reduce the quantum noise. Meanwhile, passive isolation of the laser from the environment is crucial to the reduction of classical noise. These two conditions often cannot be met at the same time. One therefore has to strike a balance between a laser design aimed for low quantum noise, which is typically free-space, bulky, and only survive in a well-maintained lab environment; and a laser design aimed for low classical noise, which is usually compact but may exhibit a high level of quantum noise [20, 21].

Secondly, before closing the feedback loop, it is important to understand where the noise comes from and how it propagates from the origin to the output of the laser, which can be described by transfer functions. Typically, the control knobs are also where technical noises can easily enter, such as changes in pump power, cavity length, or cavity alignment. The knowledge of laser's transfer functions allows one to estimate the influences of a certain noise source or the effect of a control knob. Although the control knobs one possesses may have broad control bandwidth, the actual response of the laser can in some cases be limited due to a long characteristic relaxation time (gain lifetime or cavity photon lifetime). Quantitatively, the knowledge of the spectrum of a noise source can be fed to the transfer function, so noise in the output can be predicted. While transfer functions can be experimentally measured, the interpretation could be challenging due to the complex pulse dynamics and the fact that transfer functions only give a linearized picture. To be able to directly compare the model (analytically and numerically) to the measured results will be a further step towards the better use of the control knobs.

The other aspect of successful noise suppression is the physical limits of the control knobs. The knobs mentioned above have fairly limited bandwidth, and this forbids high loop gain at low

frequencies, due to the onset of loop instability arising from time lag at high frequencies. The bandwidth limitation originates from two factors: the first is laser dynamics, which is given by the transfer function mentioned above; the second factor is the control knobs, also known as actuators. Actuators can have limited bandwidth simply because of their physical constraints. For example, acousto-optic modulators are used commonly for frequency shifting and loss modulation of a laser. Its modulation speed is limited by the acoustic propagation speed. Bandwidth beyond 1 MHz is not possible with the current acousto-optic technology. Another example is the control of cavity length. This is typically achieved with a cavity end mirror mounted on a voltage-controlled piezo actuator. The bandwidth of this mechanical system is limited by the intrinsic resonance in the piezo actuator and the finite mass of the mirror. Thus one needs to resort to very small mirrors and bulky mounts in order to push the resonant frequency to beyond 100 kHz. It is clear that there exists a fundamental limitation for these traditional actuators in achieving high bandwidth. New actuators based on a different operating principle can be attractive to use if they can be integrated with the laser without compromise in the modelocking performance.

In this Thesis, I will touch on all three aspects of reaching low-noise level for a mode-locked laser. Chapter 2 is a brief review of modelocking theory and noise model, which leads to the discussion of requirements for low quantum-limited-noise lasers. Chapter 3 discusses a new type of fast saturable absorber based on graphene. Characterization of the saturable absorption and carrier relaxation dynamics are shown. Modelocking a free-space solid state laser using graphene is also shown. Chapter 4 describes the working principle, design, fabrication, and characterization of an electro-optic modulator based on graphene, which can serve as a low-loss optical element in a laser cavity for fast, pure amplitude modulation. In Chapter 5, the use of a graphene-based loss modulator for stabilizing a fiber frequency comb is shown. With the aid of the graphene modulator, a noise level comparable to the state-of-the-art free-space combs is achieved. The fundamental difference between the traditional pump power control and the new cavity loss control is also discussed. Chapter 6 discusses a resonance in the output power of modelocked lasers in low nonlinearity and low dispersion settings. For low-noise applications, this resonance is of concern

since it affects the laser's transfer function substantially. A complete discussion of its physical origin, which relates to the coupling between soliton and continuum, is given. A good agreement is found between the theory and experiment.

## Chapter 2

### Basics of modelocking and noise

In diving into the study of noise in mode-locked lasers, it is crucial to first understand the mechanism of pulse formation and the delicate balance between the energy of the pulse and the energy stored in the gain medium as well as the effects of dispersion, nonlinearity, gain bandwidth, and saturable absorption. Modelocking refers to the state in which the laser is emitting, in the frequency domain, multiple narrow lines, each corresponding to the adjacent longitudinal modes of the laser cavity, and the relative phase between these modes are fixed. This occurs when an intensity-dependent loss is introduced into the cavity so that the laser tends to emit pulses instead of continuous waves. The intensity-dependent loss, also known as saturable absorption (either real or artificial), should decrease at high intensities for pulsing to occur, which leads to positive-feedback instability (Q-switching) in the laser. In some circumstances this Q-switching instability cannot be fully damped by the gain medium alone (gain saturation) due to the extreme ratio of upper state lifetime of the gain medium ( $10^{-6} - 10^{-3}$  s) to typical cavity roundtrip times ( $10^{-10} - 10^{-8}$  s). What further makes the laser prone to Q-switching instability is the small gain cross section ( $10^{-20}$  cm<sup>2</sup>) of solid state ion-doped gain media and the resulting high saturation energy, which requires high pulse energies for reasonable gain saturation. For low-noise applications, a constant pulse energy (cw modelocking) is desired, so a fast clamping effect has to exist in the laser to stabilize the pulse energy. This can be realized with a finite gain bandwidth, inverse saturable absorption [22], or active feedback [23]. Other physical effects involved in the pulse dynamics include chromatic dispersion, resonant gain phase and higher order effects such as Raman frequency shifting or self

steepening [24–26]. These additional effects are what make the dynamics of modelocked lasers so rich, while at the same time, they restrict the parameters of a laser to a very narrow range if Q-switching-free and low-noise operation is desired. This is the reason why the design, dynamics, and active control of a laser are closely coupled together, and why one should take all the three aspects into consideration to reach a low-noise level.

This Chapter serves as a brief review of modelocking and quantitative ways of describing modelocking (Haus model). The basic laser theory is first introduced mainly for the purpose of defining notations, which will be used throughout this Thesis. Then the master equation for modelocking, known as the Haus equation, is reviewed, which paves the way to the introduction of soliton perturbation theory. Noise in a soliton modelocked laser is discussed and a linearized noise transfer model is shown, after which a low-noise criterion for a modelocked laser is presented.

## 2.1 Rate equations: coupling between gain and photon

To describe a laser, the two most fundamental dynamic quantities are the degree of population inversion (or gain) and the number of photons. Consider the case of a continuous-wave laser, where cavity loss is constant over time. We define the gain of the electric field amplitude per roundtrip ( $T_R$ ) as  $g$  and the loss without any pump as  $\alpha$ , which is zero for a four-level system but positive for a three-level one. The power gain per roundtrip is therefore  $2g$ , given that  $g$  is small, which is valid in most low-gain solid state lasers. The use of amplitude gain rather than power gain will make the later transition to the Haus equation easier (Section 2.5). We also define the intracavity optical power as  $P$ , gain lifetime as  $\tau_L$ , saturation energy as  $E_{\text{sat,L}}$ , pump power as  $P_{\text{pump}}$ , and conversion efficiency from pump to signal light as  $\eta$ . The saturation energy can be expressed by  $E_{\text{sat,L}} = h\nu A_{\text{eff,L}}/\sigma_L$ . Here  $h$  is the Plank constant,  $\nu$  is the center optical frequency of the laser,  $A_{\text{eff,L}}$  is the effective mode area of the laser beam in the gain medium, and  $\sigma_L$  is the effective cross section of the gain medium. Then the conventional rate equations can be formulated in the

following two equations.

$$\frac{\partial g}{\partial t} = -\frac{(\alpha + g)}{\tau_L} - \frac{gP}{E_{\text{sat,L}}} + \frac{\eta P_{\text{pump}}}{2E_{\text{sat,L}}}, \quad (2.1)$$

The three terms on the right side are, first the gain relaxation, second the gain saturation, and third the energy supplied from the pump light (a factor of 2 appears in the denominator due to the use of amplitude gain  $g$  instead of power gain). The pulse energy, denoted by  $W$  or  $E_p$  (used interchangeably in this Thesis), is simply equal to  $P \cdot T_R$ . The equation describing the intracavity power  $P$  is

$$\frac{\partial P}{\partial t} = \left( \frac{2g - 2l}{T_R} \right) \cdot P \quad (2.2)$$

Here the change of optical power is directly proportional to the gain and loss  $l$  (also defined for amplitude, not power).

At the steady state,  $(\partial g / \partial t) = 0$  and  $(\partial P / \partial t) = 0$ , of a laser with constant cavity loss  $l$ , several fundamental textbook results can be obtained with the coupled Eq. 2.1 and 2.2. One result is that, above the laser threshold, the saturated gain  $g$  should be equal to loss  $l$ . Another result is that the optical power also reaches a steady state value  $P_{\text{ss}}$ , if the pump power is over a certain threshold  $P_{\text{pump}}^{\text{th}}$ . By setting  $(\partial g / \partial t) = 0$ , we obtain

$$P_{\text{ss}} = -\left( \frac{\alpha + l}{l} \right) \frac{E_{\text{sat,L}}}{\tau_L} + \frac{\eta}{2l} P_{\text{pump}} \quad (2.3)$$

The pump threshold is obtained by setting  $P_{\text{ss}} = 0$ :

$$P_{\text{pump}}^{\text{th}} = 2 \left( \frac{l + \alpha}{\eta} \right) \frac{E_{\text{sat,L}}}{\tau_L} \quad (2.4)$$

Therefore, when above threshold, the intracavity steady state power is

$$P_{\text{ss}} = \frac{\eta}{2l} (P_{\text{pump}} - P_{\text{pump}}^{\text{th}}), \quad (2.5)$$

Here it is clear that the slope efficiency between intracavity power and pump power is  $\eta/2l$ .

## 2.2 Linearized model and relaxation oscillation

The discussion so far considers that the cavity loss  $l$  does not change with time, which holds true for most continuous-wave lasers. However, intensity dynamics occurs even in cw lasers right

after the laser is turned on. This is the well-known relaxation oscillation, which is closely related to the Q-switching instability in a modelocked laser. The quantitative description can be easily understood by linearizing Eq. 2.1 and Eq. 2.2 around their steady states discussed above. Let us introduce  $g = \bar{g} + \Delta g$  and  $P = \bar{P} + \Delta P$ , where  $\bar{g} = l$  and  $\bar{P} = P_{ss}$  are steady state values, and  $\Delta g$  and  $\Delta P$  are perturbations from the steady-state values. We then obtain the following equation from Eq. 2.1 and 2.2:

$$\frac{\partial}{\partial t} \begin{bmatrix} \Delta g \\ \Delta P \end{bmatrix} = \mathbf{A} \begin{bmatrix} \Delta g \\ \Delta P \end{bmatrix}, \quad (2.6)$$

where  $\mathbf{A}$  is the transfer matrix, which is equal to

$$\mathbf{A} = \begin{bmatrix} -1/T_G & -\bar{g}/E_{\text{sat,L}} \\ 2\bar{P}/T_R & 0 \end{bmatrix}, \quad (2.7)$$

where  $T_G$  can be defined as the stimulated gain lifetime by the relation  $1/T_G = 1/\tau_L + \bar{P}/E_{\text{sat,L}}$ . The stimulated gain lifetime, which takes the stimulated emission into account, is always shorter than  $\tau_L$  when lasing. From Eq. 2.4, one can show that the stimulated gain lifetime in a four level laser ( $\alpha = 0$ ) is given by

$$T_G = \tau_L \cdot (P_{\text{pump}}/P_{\text{pump}}^{\text{th}})^{-1} = \tau_L \cdot (1 + P/P_{\text{sat,L}})^{-1}, \quad (2.8)$$

where  $P_{\text{sat,L}} = E_{\text{sat,L}}/\tau_L$  is defined as the saturation power of the gain medium.

The well-known relaxation oscillation frequency can be reproduced here by finding the eigenvalues of matrix  $\mathbf{A}$ , which gives the characteristic frequencies of the gain-photon coupling. With some straightforward algebra, the relaxation oscillation frequency for lasers well above threshold can be found:

$$f \approx \frac{1}{2\pi} \sqrt{\frac{2\bar{g}\bar{P}}{E_{\text{sat,L}}T_R}} \quad (2.9)$$

Note that the approximation made here is based on the fact that almost all solid state lasers that are relevant to the discussion here have a stimulated gain lifetime ( $T_G$ ) much longer than the cavity roundtrip time ( $T_R$ ).



### 2.3 Pulse formation: introducing time-dependent loss

To generate pulses, a time-dependent loss must exist and provide some positive feedback to the pulse energy. We now modify the constant cavity loss  $l$  to  $l + q$ , where  $q$  is a time-varying amplitude loss that depends on the intracavity power  $P$ . An overview of the actual devices (saturable absorbers) which introduce such a saturable loss will be given in Section 3.1. Here we only consider a simple two level model in which the absorption is saturated when ground and excited state populations are equal. An equation similar to the laser gain can be applied to the saturable loss  $q$ :

$$\frac{\partial q}{\partial t} = \frac{q_0 - q}{\tau_A} - \frac{q \cdot I(t)}{F_{\text{sat},A}}, \quad (2.10)$$

where  $q$  is the saturable loss,  $q_0$  is the insertion loss (when incident power  $P = 0$ ,  $q = q_0$ ),  $\tau_A$  is the relaxation time of the absorber, and  $F_{\text{sat},A} = E_{\text{sat},A}/A_{\text{eff},A}$  is the saturation fluence of the absorber ( $E_{\text{sat},A}$  is the saturation energy, and  $A_{\text{eff},A}$  is the effective mode area on the absorber). The saturation energy is given by  $E_{\text{sat},A} = h\nu A_{\text{eff},A}/\sigma_A$ , where  $\sigma_A$  is the absorption cross section of the saturable absorber. Here we use the variable  $I(t) = P(t)/A_{\text{eff},A}$  instead of  $P(t)$  since physically the saturable absorption is proportional to the intensity of light.

It is helpful to obtain an approximate formula from Eq. 2.10 when one makes assumptions about the relaxation time of the absorber  $\tau_A$ . For  $\tau_A$  much shorter than the pulse width (fast absorber approximation), the saturable loss is slaved to the pulse's intensity. With the definitions of intensity for the absorber  $I = P/A_{\text{eff},A}$  and saturation intensity of the absorber  $I_{\text{sat},A} = P_{\text{sat},A}/A_{\text{eff},A}$ , one can derive the following relation [27]:

$$q(t) = q_0 \cdot (1 + I(t)/I_{\text{sat},A})^{-1}, \quad (2.11)$$

which is a function of time  $t$ . For the following discussion of modelocking stability, it is more convenient to express the saturable loss  $q$  as a function of incident power or pulse energy. The

function  $q(W)$  can be obtained by integrating the loss over the period of pulse:

$$\tilde{q}(W) = \int_{-\infty}^{+\infty} q(t) \cdot |A(t)|^2 dt \quad (2.12)$$

For a sech<sup>2</sup>-shaped pulse, which will be relevant to the discussion of noise in the following sections, reflecting from a fast absorber, the total amplitude loss  $\tilde{q}$  is

$$\tilde{q}(S) = \frac{q_0}{\sqrt{S(1+S)}} \tanh^{-1} \left( \sqrt{\frac{S}{1+S}} \right), \quad (2.13)$$

where  $q_s$  is the saturable loss,  $q_{ns}$  is the non-saturable loss, and  $S$  is the ratio of the pulse peak intensity to the saturation intensity  $I_{\text{sat,A}}$ .

In the other limit where  $\tau_A$  is much longer than the pulse width (slow absorber approximation), the saturable loss is slaved to the pulse energy, independent of the pulse shape:

$$\tilde{q}(W) = q_0 \frac{1 - e^{-W/E_{\text{sat,A}}}}{W/E_{\text{sat,A}}} \quad (2.14)$$

## 2.4 Modelocking: Stability

After introducing time-varying loss in the laser, we can now rewrite Eq. 2.2 with the addition of saturable absorption:

$$\frac{\partial W}{\partial t} = \frac{2[g - l - q(W)]}{T_R} \cdot W, \quad (2.15)$$

where  $l$  is now the part of cavity loss that is invariant, such as an output coupler, residual reflection from a Brewster angle gain medium, and non-saturable loss from the saturable absorber. Here  $q(W)$  represents the amplitude saturable loss and changes the incident pulse energy. For the discussions from now on,  $q$  is treated as a function of  $W$  only. Note that we have just reduced the complexity of three coupled equations to the two (Eq. 2.1 and 2.15) by integrating Eq. 2.10.

The system (Eq. 2.1 and 2.15) can now be linearized near their steady state values:

$$\frac{\partial}{\partial t} \begin{bmatrix} \Delta g \\ \Delta W \end{bmatrix} = \mathbf{A} \begin{bmatrix} \Delta g \\ \Delta W \end{bmatrix}, \quad (2.16)$$

where  $\mathbf{A}$  is the transfer matrix equal to

$$\mathbf{A} = \begin{bmatrix} -1/T_G & -\bar{g}/E_{\text{sat,L}} \\ 2\bar{W}/T_R & -2\bar{W}(\partial q/\partial W)/T_R \end{bmatrix}. \quad (2.17)$$

For this coupled system to be stable, the eigenvalues of matrix  $\mathbf{A}$  have to lie on the left side of the complex plane, which is equivalent to having the trace of  $\mathbf{A}$  be negative. Note that the laser could have either two real eigenvalues (overdamped) or one pair of conjugate eigenvalues (underdamped).

We now have the condition for the laser to be stable against Q-switching instability:

$$-2\bar{W}\left(\frac{\partial q}{\partial W}\right) < \frac{T_R}{T_G} \quad (2.18)$$

Since saturable absorption implies that  $(\partial q/\partial W) < 0$  (positive feedback to pulse energy), the left hand side of the condition is positive and nearly always exceed  $T_R/T_G$  in solid state lasers due to their long upper-state lifetime and small gain cross section. Note that as long as the slope  $(\partial q/\partial W) < 0$  is reversed, which can be achieved by using two-photon absorption, free carrier absorption, or excited state absorption in the saturable absorber [22], the stability condition will always be met. In fact, inverse saturable absorption can also be provided by the finite bandwidth of the gain medium. With the variable  $P$ , it is not straightforward to describe effects such as finite gain bandwidth. In the following Section, we replace the variable in Eq. 2.15 by the electric field amplitude  $A$ . The use of field amplitude is necessary if effects such as finite gain bandwidth, chromatic dispersion, or a nonlinear index of refraction are to be included. We normalize the unit of  $A$  such that

$$P(t) = |A(t)|^2, \quad (2.19)$$

and the pulse energy  $W$  is

$$W = \int_{-T_R/2}^{T_R/2} |A(t)|^2 dt. \quad (2.20)$$

## 2.5 Modelocking: Haus master equation

To fully account for finite gain bandwidth, chromatic dispersion, and self phase modulation, the pulse energy  $W$  or power  $P$ , used in conventional rate equations, is no longer suitable. H. Haus

developed a master equation for describing modelocking with the electric field amplitude as the independent variable [28, 29]:

$$T_R \frac{\partial A}{\partial T} = \left[ -iD \frac{\partial^2 A}{\partial t^2} + i\delta |A|^2 A \right] + \mathbf{R}A, \quad (2.21)$$

where  $A = A(T, t)$  is the slowly-varying field envelope, with  $T$  and  $t$  being the time variables at a time scale of the roundtrip time ( $T_R$ ) and pulse duration respectively. The first term in the bracket is group velocity dispersion (GVD), where  $D$  is the total group delay dispersion experienced by the pulse per roundtrip. The second term in the bracket is self phase modulation, where  $\delta$  is the SPM coefficient given by  $2\pi n_2 \ell_L / \lambda_0 A_{\text{eff,L}}$ . Here  $n_2$  is the intensity-dependent refractive index,  $\ell_L$  and  $A_{\text{eff,L}}$  are the effective path length and mode area, and  $\lambda_0$  is the center wavelength.  $\mathbf{R}$  represents all the other effects including, but not restricted to, gain bandwidth, mirror bandwidth, linear gain, linear loss, and saturable loss. The effects of GVD and SPM are isolated from other ones for the convenience of discussing soliton perturbation theory in later Sections. Now we can explicitly write  $\mathbf{R}$  out for a typical modelocked solid state laser:

$$\mathbf{R} = \left[ g - l + \frac{g}{\Omega_g^2} \frac{\partial^2}{\partial t^2} - q - \Gamma_{\text{TPA}} |A|^2 \right] \sum_{m=-\infty}^{\infty} \delta(T - mT_R), \quad (2.22)$$

where  $g$ ,  $l$ , and  $q$  are the amplitude gain, loss, and saturable loss per roundtrip,  $\Omega_g$  is the half-width half-maximum of the gain bandwidth, and  $\Gamma_{\text{TPA}} = \beta_{\text{TPA}} \ell_{\text{TPA}} / A_{\text{eff,A}}$  is the TPA coefficient that has taken the TPA coefficient ( $\beta_{\text{TPA}}$ ), effective layer thickness ( $\ell_{\text{TPA}}$ ), and mode area into account ( $A_{\text{eff,A}}$ ). Here the sum of delta functions represent the effect of periodic perturbations of pulses, which can be ignored if only stable solutions are concerned. The effect of periodic perturbation is crucial for understanding continuum generation, which will be discussed in Chapter 6. Note that when  $\mathbf{R} = 0$ , the equation becomes the nonlinear Schrödinger's equation (NSE).

General analytic solutions cannot be obtained from the master equation. As in the discussion of Haus and Mecozzi [8], we focus on the unchirped solution due to its simplicity in theoretical treatment. This is also an important regime to study for compact low-noise solid state lasers because of its ease of applicability to the generation of sub-picosecond pulses in a high-repetition-

rate laser. The unchirped steady-state closed form solution to Eq. 2.21 and 2.22 is soliton, which can be expressed as the following [30, 31]:

$$A_s(T, t) = A_0 \text{sech}(x) e^{i\theta}, \quad (2.23)$$

$$x = \frac{1}{\tau} \left( t - 2|D|p_0 \frac{T}{T_R} - t_0 \right), \quad (2.24)$$

$$\theta = p_0(t - t_0) + |D| \left( \frac{1}{\tau^2} - p_0^2 \right) \frac{T}{T_R} + \theta_0 \quad (2.25)$$

which is the fundamental soliton. Here  $p_0$  is the frequency offset introduced deliberately into the solution to account for center frequency shift of the soliton. For  $p_0 \neq 0$ , the soliton simply acquires a group delay (Eq. 2.24) and an optical phase shift (Eq. 2.24) due to the presence of GVD. Note that  $\tau$  here is the soliton pulse width, which is related to the FWHM pulse width by  $\tau_{\text{FWHM}} = \tau * 1.7627$ . The nonlinear phase  $\Phi_0$ , which a soliton gains per roundtrip time, can be expressed by

$$\Phi_0 = \frac{1}{2} \delta A_0^2 = \frac{|D|}{\tau^2}, \quad (2.26)$$

Note that this phase is uniform across the whole soliton spectrum, not contradicting to the  $p_0$  dependence in Eq. 2.25. Another important property is the area theorem:

$$W = \int_{-\infty}^{\infty} |A_s|^2 dt = 2A_0^2 \tau = \frac{4|D|}{\delta \tau}, \quad (2.27)$$

which states the the product of the pulse energy  $W$  and the pulse width  $\tau$  is a constant that depends only on GVD and SPM. We can already see that the four parameters for describing the soliton pulses are pulse energy  $W$ , pulse timing  $t_0$ , optical phase  $\theta$ , and center frequency  $p$ . In the classic paper of Haus and Mecozzi, the noise in these four parameters arising from the quantum fluctuations (both from the spontaneous emission and cavity loss) are discussed with the use of soliton perturbation theory. In the next Section, soliton perturbation theory is briefly reviewed.

## 2.6 Modelocking: Soliton perturbation theory

The noise, which is typically smaller than the solitary pulse amplitude, can be treated as perturbations to the soliton solution (Eq. 2.23). We assume that the deviation of the pulse shape

from Eq. 2.23 is small when we include  $\mathbf{R}$ . That is, we allow small changes in the four fundamental quantities of a soliton: they are pulse energy ( $W$ ), timing ( $t$ ), center frequency ( $p$ ), and optical phase ( $\theta$ ). A component ( $a_c$ ) that is orthogonal in the linearized NSE to the soliton, which is dubbed continuum, is also included here. Note that the change of  $W$  is hidden in the variable  $A$ , which is the time-varying amplitude of the soliton field.

$$A(T, t) = (A \operatorname{sech}(x) + a_c(T, t)) e^{i\theta} \quad (2.28)$$

By inserting this ansatz into the master equation, a linearized set of equations of motion can be derived. Here we denote the changes in  $A(T, t)$ , including the changes in soliton and continuum.

$$T_R \frac{\partial}{\partial T} |\Delta \mathbf{A}\rangle = \hat{\mathbf{Q}} |\Delta \mathbf{A}\rangle + \mathbf{S} \quad (2.29)$$

The operator  $\hat{\mathbf{Q}}$  stands for the linearized effects including GVD, SPM and other effects included in  $\mathbf{R}$ . Note that in Haus and Mecozzi's paper [8], the whole master equation is linearized, whereas in some situations [30, 31], where continuum-induced instability rather than noise is the main concern, only the GVD and SPM actions are linearized, but  $\mathbf{R}$  is kept as a perturbation. This latter approach is useful for discussing periodic perturbation of soliton, and is mathematically compatible with the original soliton perturbation theory. The latter approach will be adopted in Chapter 6.

Here we continue following Haus's approach. The  $\mathbf{S}$  term represents noise sources; in particular, the quantum mechanical fluctuations from spontaneous emission will be discussed. The use of vector form in  $|\Delta \mathbf{A}\rangle = (\Delta A, \Delta A^*)^T$  and also in  $\mathbf{A}$  and  $\mathbf{S}$  here is to keep track of both the amplitude change  $\Delta A$  and its complex conjugate  $\Delta A^*$  since they are coupled together in NSE due to Kerr nonlinearity.

From the linearized master equation (Eq. 2.29), one can derive the following equations of motion for the pulse energy  $W$  [8, 31]:

$$T_R \frac{\partial W}{\partial T} = \left[ 2g - 2l + -\frac{2g}{3\Omega_g^2 \tau^2} - 2q - \frac{4\Gamma_{\text{TPA}} |A_0|^2}{3} \right] W + \langle \mathbf{f}_W^{(+)} | \mathbf{S} \rangle \quad (2.30)$$

This equation describes the change of pulse energy per roundtrip  $T_R(\partial W / \partial T)$ . The right-hand-side terms in the bracket are linear gain, linear loss, gain filtering, saturable loss, and two-photon

absorption. The coupling of continuum  $\mathbf{a}_c$  back to the soliton and the noise term is grouped in the last inner product. Here langle  $\langle \mathbf{f}_W^{(+)} |$  is the adjoint function of the derivative of the soliton solution (Eq. 2.23) with respect to the pulse energy, which allows the projection of soliton parameters changes.

For the timing ( $t$ ) equation of motion, we take the inner product of Eq. 2.29 with the adjoint function  $\langle \mathbf{f}_t^{(+)} |$ :

$$T_R \frac{\partial \Delta t}{\partial T} = -2|D|\Delta p + \langle \mathbf{f}_t^{(+)} | \mathbf{S} \rangle. \quad (2.31)$$

The first term arises from the coupling between center frequency and timing of a soliton, which is the origin of the Gordon-Haus timing jitter.

For center frequency, the restoring force comes from the finite bandwidth of the gain:

$$T_R \frac{\partial \Delta p}{\partial T} = -\frac{4g}{3\Omega_g^2 \tau^2} \Delta p + \langle \mathbf{f}_p^{(+)} | \mathbf{S} \rangle. \quad (2.32)$$

The optical phase is affected by the pulse energy change through SPM:

$$T_R \frac{\partial \Delta \theta}{\partial T} = \frac{2\Phi \Delta W}{W} + \langle \mathbf{f}_\theta^{(+)} | \mathbf{S} \rangle. \quad (2.33)$$

## 2.7 Noise in modelocked lasers: Haus-Mecozzi model

With the four equations of motion for soliton parameters, we can calculate the noise in these parameters caused by the intrinsic noise source of the laser, which is spontaneous emission. For this discussion, we assume  $a_c$  is negligible and only consider the noise source term  $\mathbf{S}$ .

Spontaneous emission fluctuations can be treated as white noise with the following autocorrelation, which can be verified to show that spontaneous emission contributes one noise photon per Hz bandwidth.

$$\langle S(T, t) S^*(T', t') \rangle = \theta \frac{2g}{T_R} h\nu \delta(T - T') \delta(t - t'), \quad (2.34)$$

where  $\theta$  is the noise enhancement factor ( $\theta = 1 + l_{\text{reabs.}}/g$ , where  $l_{\text{reabs.}}$  is the reabsorption loss when lasing; thus,  $\theta$  is close to 1 in a four-level laser but greater than 1 in a three-level laser),  $g$  is the saturated gain, and  $\nu$  is the center optical frequency.

The noise in the timing ( $t$ ) and optical phase ( $\theta$ ) of the soliton are directly related to the pulse repetition frequency ( $f_{\text{rep}}$ ) and carrier-envelope offset frequency ( $f_{\text{ceo}}$ ), since the optical frequency of one mode is as follows:

$$f_{\text{optical}} = n f_{\text{rep}} + f_{\text{ceo}}, \quad (2.35)$$

where  $n$  is the mode number. Therefore, the discussion here is focused on the power spectral density (PSD) of the timing and optical phase noise. For the timing noise, the direct contribution from spontaneous emission is from the projected term  $\langle \mathbf{f}_{\mathbf{t}}^{(+)} | \mathbf{S} \rangle$ . The one-sided (defined from frequency 0 to  $\infty$ ) PSD of the noise is [8, 24, 25]:

$$S_{\Delta t}(f) = \left( \frac{1}{2\pi f} \right)^2 \cdot \left( \frac{2g\theta h\nu}{T_{\text{R}}} \right) \cdot \left( \frac{\pi^2 \tau^2}{6W} \right), \quad (2.36)$$

where the first factor arises from the random walk nature of spontaneous emission, the second factor is the power contributed by spontaneous emission, and the last factor is a projection coefficient derived from  $\langle \mathbf{f}_{\mathbf{t}}^{(+)} | \mathbf{S} \rangle$ . Remember that  $g$  represents the amplitude gain, not intensity gain.

The indirect contribution of spontaneous emission to the timing error is from the combined effects of center frequency jitter and non-zero intracavity chromatic dispersion. Note that the center frequency error  $\Delta p$  is naturally damped by the finite gain bandwidth (Eq. 2.32), and its associated one-sided PSD is given by

$$S_{\Delta p}(f) = \left[ \frac{1}{(2\pi f)^2 + (4g/3\Omega_{\text{g}}^2 \tau^2)^2} \right] \cdot \left( \frac{2g\theta h\nu}{T_{\text{R}}} \right) \cdot \left( \frac{2}{3W\tau^2} \right). \quad (2.37)$$

It can be seen that finite gain bandwidth provides damping to the frequency jitter at low frequencies. With the center frequency jitter PSD, one can derive the indirect timing jitter caused by intracavity dispersion, which is known as Gordon-Haus jitter:

$$S_{\Delta t}^{\text{GH}}(f) = \left( \frac{4|D|^2}{T_{\text{R}}^2} \right) \cdot S_{\Delta p}(f) \quad (2.38)$$

For the optical phase fluctuations, we assume a known noise PSD of the relative intensity fluctuation (RIN) ( $S_{\Delta W}(f)$ ), which is experimentally measurable. Then the noise in the optical phase  $\Delta\theta$  is directly related to RIN through the Kerr effect (self-phase modulation):

$$S_{\Delta\theta}(f) = \left( \frac{4\Phi^2}{T_{\text{R}}^2} \right) \cdot S_{\Delta W}(f) \quad (2.39)$$



Note that RIN is typically dominated by the pump's RIN, which is much higher than the quantum noise contribution; at high frequencies, the intensity fluctuation is strongly filtered by a second-order low-pass filter due to the coupling between gain and photon.

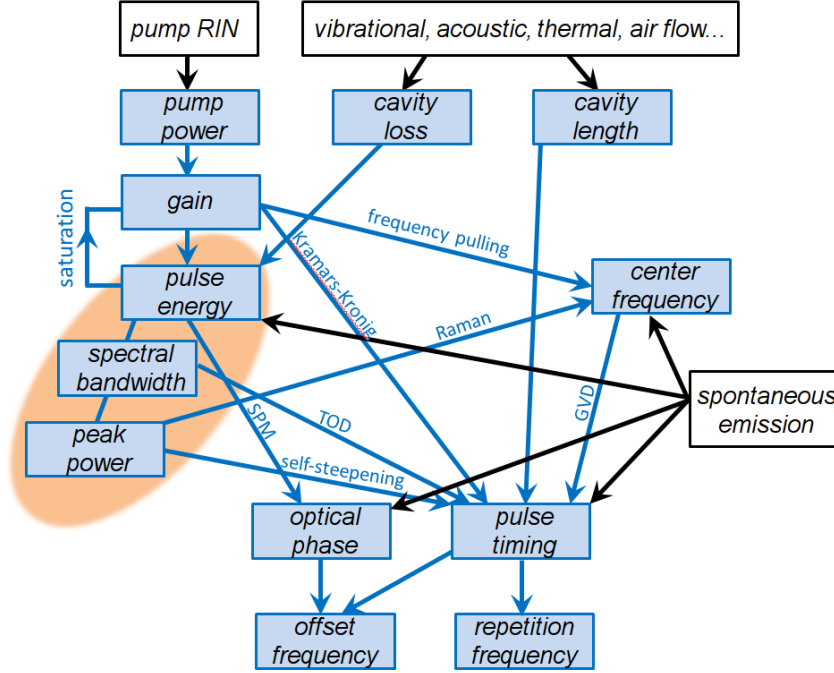


Figure 2.1: Diagram of the noise transfer pathways from the input to the output of a modelocked laser. Noise mostly enters through changes in pump power, cavity loss, or cavity length, shown on the top. The propagating pathways are indicated by arrows with the physical mechanism indicated. GVD: group velocity dispersion; TOD: third-order dispersion; SPM: self-phase modulation. Note that for a soliton laser, the three pulse parameters (pulse energy, spectral bandwidth, and peak power) are closely related through SPM and GVD. Spontaneous emission directly affects the four soliton parameters: pulse energy, center frequency, pulse timing, and optical phase.

In Fig. 2.1, all major contributions to the noise in the output of a modelocked laser are shown. Quantum noise, resulting from spontaneous emission, contributes directly to the pulse energy, optical phase, pulse timing, and center frequency; while classical noise, resulting from technical reasons, enters the laser through control knobs such as pump power, cavity loss, or cavity length. To minimize the free-running noise of a modelocked laser at its quantum limit, one has to reduce the power of spontaneous emission and its effect on the pulse at all costs, which implies reducing cavity loss (thus saturated gain), shortening the pulse width, and increasing the pulse

energy. Furthermore, one can soften the link from the noise source to the output, which implies reducing intracavity dispersion (Gordon-Haus) and nonlinearity (AM-PM through SPM). At low frequencies, the laser is typically swamped by classical noise, which should be isolated from the laser.

## Chapter 3

### Graphene as a saturable absorber for modelocking

In Chapter 2, the fundamentals of modelocking and noise in modelocked lasers are reviewed. The quantum limit of noise in free-running modelocked lasers can be revealed when technical noise sources in the environment are damped or well isolated from the laser. This quantum-limited noise level, in the case where it is dominated by direct ASE contribution, can be made intrinsically low in lasers that have the following qualities: short pulses, high intracavity power, and low cavity loss [8]. On the one hand, isolating the laser from the environment is relatively easy to achieve using a more compact cavity design, which implies a high repetition rate ( $> 1$  GHz). On the other hand, having a low quantum-limit noise level in high repetition rate lasers can be challenging mainly due to the  $T_R^{-2}$  scaling as shown in Eq. 2.38 and 2.39. One of the difficulties is the lack of a reliable modelocking mechanism that allows the generation of short pulses ( $\sim 100$  fs) in a high repetition rate laser. Effective absorbers, such as those based on a nonlinear lens (Kerr lens), excel at generating short pulses, of which a low-noise level can still be maintained at high repetition rates [32, 33]. This benefit comes at the cost of some coupling between the saturable absorption and cavity alignment, which prevents its use in hands-free, long-term applications. In fiber-based lasers, an artificial saturable absorber can be obtained by the dependence of polarization on peak intensity (nonlinear polarization rotation) [34, 35] or by interference of pulses between two counterpropagating pulses in a fiber loop (nonlinear loop mirror or nonlinear amplifier loop mirror) [36, 37]. Despite the intrinsically closed, compact nature of waveguides, these artificial absorbers can still have drifting parameters due to temperature changes. Another disadvantage in fiber systems is the high free-running noise

due to their high-loss-high-gain and high non-linearity/dispersion operation. Nevertheless, free-running noise can be removed with active feedback control, which will be discussed in Chapter 5. Here the discussion is focused on suitable real saturable absorbers for low-gain free-space solid-state lasers.

This Chapter discusses the use of graphene as a saturable absorber. First, an overview of current saturable absorber technologies is given, which is followed by a brief summary of motivation to investigate graphene's use as a saturable absorber in solid state lasers. Then a review of graphene's physical and optical properties will be given, with the focus on its band structure and optical absorption. After that, a study of the saturable optical absorption of graphene is described in detail: a model, characterization methods, and results are given. The other essential property of a saturable absorber—carrier dynamics—is also characterized. The result of modelocking a free space Er:Yb:glass laser with graphene is shown. Finally, a conclusion is drawn on graphene's pros and cons as a saturable absorber.

### 3.1 Overview of saturable absorbers

A saturable absorber is an optical element that absorbs less light when the light intensity is high, or an artificial mechanism that achieves the same effect. The discussion here focuses on the former—real saturable absorbers. Real saturable absorbers are advantageous for their decoupled saturable absorption from the design or alignment of the laser cavity, which generally allows for more stable, long-term operation of the laser compared to their artificial counterparts. The disadvantages that accompany this benefit are the long recovery time, narrow absorption spectral width, and optical damage at high pulse fluences.

The most commonly used saturable absorbers for modelocking solid state lasers today are semiconductor saturable absorbers. Initially, they were too lossy to be used directly as a reflecting mirror in a cavity therefore special cavity designs had to be applied. (Historical development can be found in [38]). Minimizing cavity loss is particularly important for solid state lasers because of their small gain emission cross section ( $\sim 10^{-20} \text{cm}^2$ ). The first practical low-loss versions of

semiconductor saturable absorber mirrors were demonstrated with a Bragg reflector that was integrated with a thin semiconductor layer with a bandgap matching the desired absorption optical band. This structure have been referred to as saturable Bragg reflectors (SBR) [39–41] or as semiconductor saturable absorbers mirrors (SESAM) [38, 42]. Both the linear and nonlinear absorption in SESAM can be engineered. Some variable parameters of a SESAM design are the position of the thin semiconductor layer, anti-reflective coating, and non-quarter-wave stack for dispersion compensation [43].

The design freedom of SESAM is valuable for modelocking solid state lasers without the onset of Q-switching instability since one can tailor the saturation fluence and modulation depth by the SESAM layer structure [44, 45], or by using two-photon absorption in the top few layers [22]. For compact lasers with a high repetition rate, it is still challenging to use SESAM for stable cw modelocking and sub-picosecond pulse generation at the same time due to the limit imposed by both the laser dynamics and semiconductor materials. A simple criterion for cw modelocking can be expressed as the the following [46] (derived from Eq. 2.18):

$$E_p^2 > E_{\text{sat,L}} \cdot E_{\text{sat,A}} \cdot \Delta R,$$

where  $E_p$  is the pulse energy,  $E_{\text{sat,L}}$  and  $E_{\text{sat,A}}$  are the saturation energy of the gain medium and saturable absorber, respectively, and  $\Delta R$  is the modulation depth of the saturable absorber. For generating sub-picosecond pulses, high  $\Delta R$  and short recovery time is favored in the case where saturable absorber is the main pulse shaping mechanism. However, the above criterion is hard to achieve since  $E_p$  is limited due to a high repetition rate, unless the average power can also be raised. A short recovery time is often obtained with the sacrifice of an increase in the non-saturable loss [38, 44], which further makes power scaling difficult. The long recovery time can be overcome by modelocking in the soliton regime, where group velocity dispersion (GVD) and self phase modulation (SPM) combined dominate in the pulse shaping process. The generated solitary pulses can be 10 to 20 times shorter than the recovery time of the saturable absorber [27, 30]. The existing few demonstrations of SESAM-modelocked solid state lasers at GHz repetition rates and

sub-picosecond pulses (including fiber lasers) have all been realized in this regime [47–50].

Consequently, real saturable absorbers with short recovery time and low saturation fluence (or energy) are attractive for modelocking high repetition rate lasers. Carbon nanotubes emerged as a new optical material that has sub-picosecond recovery time and reasonably low saturation fluence [51–54], despite their high nonsaturable to saturable loss ratio and optical damage by high peak power [55]. The demonstration of the carbon nanotube/polymer has paved the way to fabricating saturable absorbers with ease on almost any optical substrate [55], fiber ends, or tapered fibers [56], which is rather difficult, if not impossible, with SESAM’s epitaxy growth technology.

### 3.2 Why use graphene?

As a close carbon family member of carbon nanotubes, graphene also exhibits saturable absorption. Due to its unique band structure, its optical absorption and therefore saturable absorption is extremely broadband and featureless (mid-IR to visible wavelength). This potentially makes graphene a one-material-for-all-lasers candidate. Also, the recovery time in graphene is favorable because of its very fast carrier-carrier scattering and carrier-phonon scattering ( $< 100$  fs), which is followed by a  $\sim 1$  ps electron-hole recombination. The fast recovery component makes graphene a fast absorber for creating an ultrashort temporal loss window while the slow time component helps to self-start the modelocking. Compared to the growth of SESAM, the method for fabricating large area graphene requires a much simpler setup, accessible to non-experts. A graphene saturable absorber can be transferred from its growth substrate to almost any optical substrate. The first report of using graphene (a few layers in this case) as a saturable absorber also showed a low saturation intensity of graphene at  $\sim 1$  MW/cm<sup>2</sup> [57], which would be ideal for cw modelocking of GHz-repetition-rate lasers due to the low pulse energy.

### 3.3 Band structure of graphene

Graphene’s unique physical properties result primarily from two important characteristics: (1) Carriers are confined in a two-dimensional plane; (2) The lattice is a honeycomb structure,

which consists of two identical sublattices, as shown in Fig.3.1(a). Although electrons moving in such a lattice do not approach the speed of light at all, their motion at low energy is “relativistic” and simply resembles a massless particle, which has a linear relation between the energy and the momentum. In essence, the motion can be described by Dirac equation, but with the speed of light replaced by a 300 times smaller value, which is the Fermi velocity of electrons in graphene ( $v_F$ ).

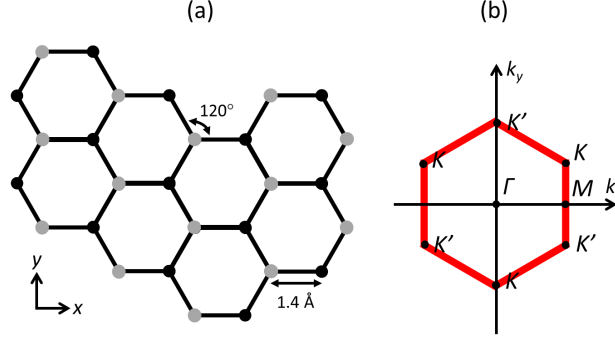


Figure 3.1: (a) Carbon lattice of graphene in real space. Black and gray circles represent two sublattices in the honeycomb structure. Note that one unit cell contains one black and gray atoms. The spacing between the nearest neighbor atom is  $a$ , which is around  $1.42\text{\AA}$ . (b) Reciprocal lattice of graphene in the first Brillouin zone. The  $K$  and  $K'$  points, also referred to as Dirac points, are where the electrons behave like massless particles.

The band structure of graphene was first studied by Wallace [58]. With the tight-binding approximation that includes the nearest neighbor hopping term, one can show that the energy-momentum relation is the following: [58, 59]

$$E(\mathbf{k}) \approx \pm E_{n,n} \cdot [3 + 2 \cos(\sqrt{3}k_y a) + 4 \cos(\sqrt{3}k_y a/2) \cos(3k_x a/2)]^{1/2},$$

where  $E_{n,n} = 2.8 \text{ eV}$  is the nearest neighbor hopping energy,  $\mathbf{k} = k_x \hat{x} + k_y \hat{y}$  is the wavevector of the crystal momentum ( $\mathbf{p}$ ), and  $a$  is the distance between two nearest neighbor carbon atoms. Expanding Eq. 3.3 around the Dirac points ( $K$  or  $K'$ ), one obtains

$$E(\mathbf{k}) = \pm E_{n,n} \cdot \frac{3a}{2} |\mathbf{k} - \mathbf{k}_{\text{Dirac}}| = \pm \hbar v_F |\mathbf{k} - \mathbf{k}_{\text{Dirac}}|.$$

Notice that this is a linear energy-momentum dispersion similar to what photons have, except here the speed of light is replaced by the Fermi velocity ( $v_F$ ), which is equal to  $E_{n,n} \cdot 1.5 \cdot a / \hbar \approx 9 \times 10^5 \text{ m/s}$ .

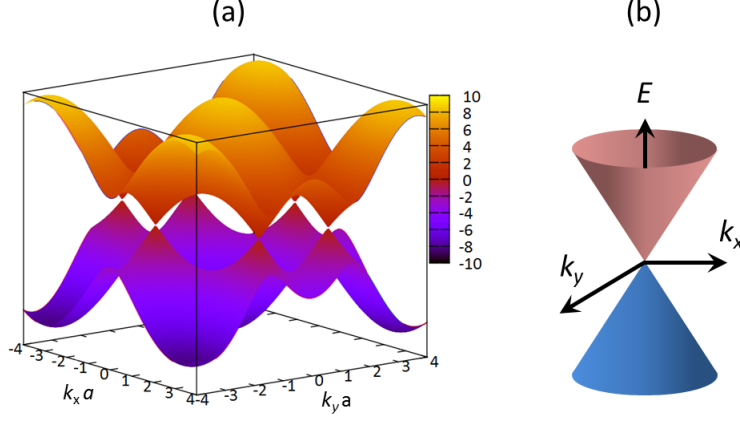


Figure 3.2: (a) Energy bands of graphene near the first Brillouin zone. The vertical axis is energy in eV. Note that two energy bands are plotted here. The band below the six Dirac points ( $K$  and  $K'$ ), which is the valence band, is fully filled in undoped graphene. The upper energy band is the conduction band. (b) Zoomed-in energy bands near one of the Dirac points. The slope of the cone is defined by the Fermi velocity ( $v_F$ ).

The density of states is linear in energy, which can be seen in the following relation:

$$\frac{dN}{dE} = \frac{dN}{d|\mathbf{k}'|} \frac{d|\mathbf{k}'|}{dE} = \frac{|\mathbf{k}'|}{\pi} \cdot \frac{1}{(\hbar v_F)} \cdot 2 = \frac{2E}{\pi(\hbar v_F)^2}.$$

Here  $N$  is the number of states per unit area and  $|\mathbf{k}'| = |\mathbf{k} - \mathbf{k}_{\text{Dirac}}|$  is relative wavevector with respect to  $K$  and  $K'$  points. Note that a factor of 2 is multiplied in because there are two Dirac cones in the first Brillouin zone.

In pristine graphene, the Fermi level lies exactly at the Dirac point because each carbon atom contributes one bonding electron and there are two atoms per unit cell so that the lowest band is exactly filled (spin degeneracy is two), making graphene a semimetal. When the Fermi level is above the Dirac point, the conductivity is dominated by electrons (n-doping); and when the Fermi level is below the Dirac point, the conductivity is dominated by holes (p-doping). The carrier density per unit area can be obtained by integrating Eq. 3.3:

$$n = \int_0^{E_F} \frac{2E}{\pi(\hbar v_F)^2} dE = \frac{E_F^2}{\pi(\hbar v_F)^2}.$$



### 3.4 Linear absorption in graphene

#### 3.4.1 Theoretical background

The optical interband absorbance of undoped graphene is characterized by a product of fundamental constants, which is  $\pi\alpha = 2.3\%$ , where  $\alpha$  is the fine structure constant, over a broad optical bandwidth. This universality absorption arises from the perfect cancellation of energy dependence in Fermi's golden rule and density of states:

$$\frac{\text{Absorbed power}}{\text{Incident power}} \propto \frac{|\langle\psi_f|H_1|\psi_i\rangle|^2 \cdot (\text{DoS}) \cdot (\hbar\omega)}{|E_0|^2}, \quad (3.1)$$

where the first term is the transition matrix element,  $H_1$  represents the electron-photon interaction Hamiltonian in first order perturbation theory, and  $\psi_f$  and  $\psi_i$  are the final and initial states. The product of the transition matrix element and the density of states (DoS) gives the transition probability per unit time.  $|E_0|$  is the electric field of the incident light.

For graphene, because of its massless Hamiltonian ( $H = v_F \mathbf{p}$ ), the interaction perturbation is given by  $H_1 = (v_F e/c) \cdot \mathbf{A}$ , where  $\mathbf{A}$  is the vector potential and its magnitude is given by  $|E_0|/\omega$ . By inserting these relations into Eq. 3.1 above, it can be found that the linear energy dependence in the density of states of graphene (Eq.3.3) cancels with an inverse square proportionality in the squared transition matrix element and the photon energy. Therefore the absorption is a constant over a broad bandwidth. In fact, this universal absorption does not only hold true for massless electrons in graphene but also for electrons in many conventional two-dimensional semiconductors (quantum wells) [60]. Note that in a textbook 3D semiconductor, the interaction Hamiltonian is instead given by  $H_1 = (e/c)\mathbf{p} \cdot \mathbf{A}$ , which results in an absorbance that is directly proportional to the density of states for massive electrons ( $H = |\mathbf{p}|^2/2m^*$ ), where  $m^*$  is the effective mass of electrons moving in a lattice.

The discussion thus far has only concerned pristine graphene, where the valance band is fully filled and the Fermi level is exactly at the Dirac point. There are changes in the optical absorption as the Fermi level (equivalently chemical potential) changes. This can be seen qualitatively in

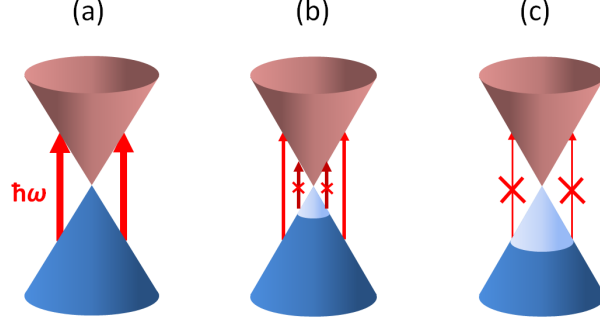


Figure 3.3: Red: conduction band; blue: valence band; Light blue: vacant states (hole-doping); arrows represent interband absorption of a photon. Note that at finite temperature, Fermi-Dirac statistics introduced some fuzziness to the interface between occupied (blue) and vacant states (light blue) (a) Absorption in undoped, pristine graphene is 2.3%. (b) Absorption at low photon energy is reduced due to hole doping. (c) With strong doping, the absorption is totally blocked.

Fig. 3.3, which shows the band structure of graphene near the Dirac cones and the transition probability of an interband absorption. In undoped graphene (Fermi level at Dirac point, shown in (a)), the absorption is given by  $\pi\alpha$ , and as the doping goes below the Dirac point (hole doping or p-doping), the absorption at low photon energies (precisely speaking, below twice the Fermi level) is more or less blocked due to the vacancies of initial states, shown in (b). As the doping is further increased, the blocked spectral region widens.

These doping induced changes in the optical absorption can be quantitatively predicted by considering the optical conductivity ( $\sigma$ ) of graphene as a function of optical frequency( $\omega$ ), chemical potential( $\mu$ ), and temperature( $T$ ) [61]:

$$\sigma = \sigma_0 \left[ \frac{1}{2} + \frac{1}{72} \frac{(\hbar\omega)^2}{t^2} \right] \left( \tanh \frac{\hbar\omega + 2\mu}{4k_B T} + \tanh \frac{\hbar\omega - 2\mu}{4k_B T} \right), \quad (3.2)$$

where  $\sigma_0$  is the optical conductivity of undoped graphene ( $\mu = 0$ ),  $t$  is the hopping parameter connecting first nearest neighbors in the tight-binding model for graphene,  $k_B$  is the Boltzmann constant,  $e$  is the electron charge,  $\hbar$  is the reduced Plank constant, and  $T$  is the temperature of the sample. For the following discussion, we neglect the term  $(\hbar\omega/t)^2$  since  $1/72 \times (\hbar\omega/t)^2 < 3 \times 10^{-3} \ll 1/2$  for the photon energies we work with ( $< 1.2$  eV).

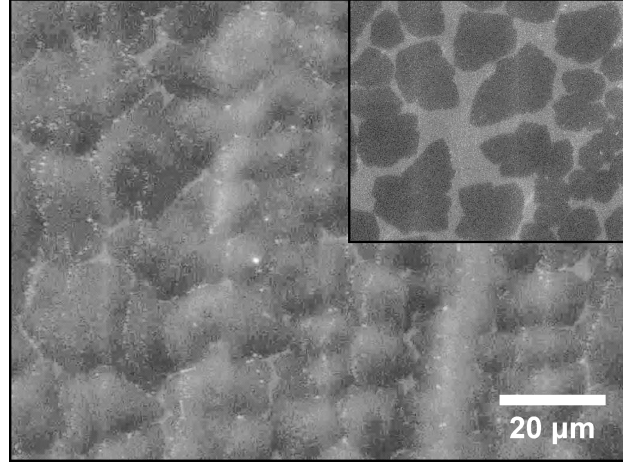


Figure 3.4: A scanning electron microscope image of graphene domains and boundaries. Inset: disconnected graphene domains that are grown without a second step of high methane flow rates. The domain sizes ( $100\text{-}400\text{ }\mu\text{m}^2$ ) are much larger than the laser beam size in our experiments and are sufficient for most laser applications.

### 3.4.2 Sample preparation and characterization

The graphene samples used in the experiment and throughout this thesis were grown on copper foils (Alfa Aesar #13382,  $25\text{ }\mu\text{m}$ ) by chemical vapor deposition (CVD) [62]. The CVD setup is described in detail in Appendix A. The total pressure in our CVD process was maintained at a level of 10 mTorr in order to obtain large domains of graphene [63]. The CVD process began with the annealing of the copper foils at  $1000^\circ\text{C}$  with 5 sccm  $\text{H}_2$  flow for 30 minutes. While the copper foils were maintained at  $1000^\circ\text{C}$ , graphene was grown with 1 sccm  $\text{H}_2$  and 1 sccm  $\text{CH}_4$  for 30 minutes, followed by a 5-minute phase of 1 sccm  $\text{H}_2$  and 10 sccm  $\text{CH}_4$  to fill gaps between domains [63]. Fig. 3.4 shows the domain sizes and boundaries of our CVD graphene. After the growth, the graphene on copper foils was spin-coated with polymethyl methacrylate (PMMA) for mechanical support during the wet-transfer processes, in which the copper foils were etched by ferric chloride (0.5M) solution, and the graphene was washed in deionized water several times before being transferred onto a microscope slide (VWR #48300-025).

The transferred graphene was baked in a tube furnace at  $300^\circ\text{C}$  for an hour with 50 sccm Ar flow, 5 sccm  $\text{H}_2$  flow (pressure  $\approx 30$  mTorr), reducing the doping that could result from adsorbates

such water molecules or other contaminants [64, 65]. Moreover, we found that this heat treatment can prevent the delamination of the graphene from the substrates in the following doping step, which we hypothesized to be caused by the removal of water molecules between the graphene layer and the substrate. Here we use nitric acid of low concentration ( $\leq 0.8$  wt%) to p-doped graphene [66]. The acid was drop-cast on the graphene surface and, after five minutes, blown dry by nitrogen. Various doping levels were achieved by nitric acid of concentrations from 0.1 to 0.8 wt%.

The linear absorption determines the maximum nonlinear modulation depth (or saturable loss) that graphene has. Since the linear absorption is reduced with a non-zero doping level, as predicted by the optical conductivity in Eq. 3.2, it is crucial that the doping level and linear absorption are characterized before the nonlinear absorption is studied. It should be noted that Fermi levels in graphene are often estimated from the gate voltage needed for obtaining the minimum electrical conductivity [67]. This method, however, brings complications of gate electrode implementation in transmissive samples.

We quantified the Fermi levels by graphene's infrared transmission spectra from 3000 nm to 900 nm with a spectrophotometer (Varian, Cary 500). The beam was 3 mm in diameter and at near-normal incidence to the graphene-substrate interface. A large beam size was used in order to average the spatial-dependent doping caused by the substrate and possibly by the dopants. The calibration of the transmission spectra was done by subtracting the spectrum of a blank microscope slide from all measurements.

The expected transmission loss of such samples can be predicted as the following. At normal incidence, the transmittance  $\mathcal{T}$  of graphene at the interface of air ( $n = 1$ ) and glass ( $n \approx 1.5$ ) is the following:

$$\mathcal{T} = \frac{4n_1n_2}{(n_1 + n_2 + \sigma/c\epsilon_0)^2} \approx \mathcal{T}_0 \left[ 1 - \frac{2\sigma}{c\epsilon_0(n_1 + n_2)} \right], \quad (3.3)$$

where  $c$  is the speed of light in vacuum,  $\epsilon_0$  is the vacuum permittivity, and  $\mathcal{T}_0 = 4n_1n_2(n_1 + n_2)^{-2} = 0.96$  is the transmittance at the same interface without graphene. The change of transmittance due

to the presence of graphene, including the two interfaces of a substrate, is then

$$\Delta\mathcal{T}_{total} = |\mathcal{T}\mathcal{T}_0 - \mathcal{T}_0^2| = \frac{2\sigma\mathcal{T}_0^2}{c\epsilon_0(n_1 + n_2)}. \quad (3.4)$$

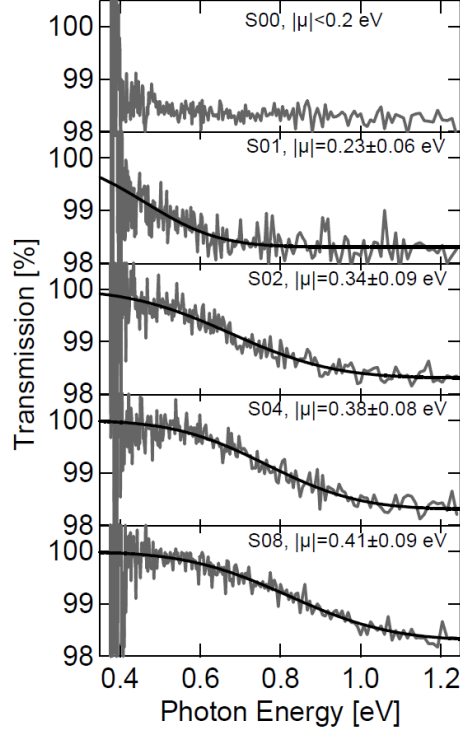


Figure 3.5: Transmission spectra of doped graphene as a function of photon energy. The doping level can be controlled by nitric acid of different concentrations. Gray line: measurement; black line: fit. From top to bottom, the curves represent (S00) baked graphene, (S01) baked and doped by 0.1wt% acid, (S02) baked and doped by 0.2wt% acid, (S04) baked and doped by 0.4wt% acid, (S08) baked and doped by 0.8wt% acid. Linear optical absorption at low photon energy decreases as the p-doping level increases. Note that chemical doping does not cause defects in graphene, as verified with Raman spectroscopy, shown in Appendix B.

Figure 3.5 shows the transmission spectra of graphene samples that are chemically p-doped to different levels. Due to spatial variations in the doping resulting from substrates and dopants, the curves in Fig. 3.5 possess a slow transition from occupied states to vacant states in the valence band, as shown in Fig. 3.3. Assuming that the distribution of these spatial variations follows a normal distribution, which has a mean value of  $\mu$  and a spread of  $\Delta\mu$ , we can fit the data in Fig. 3.5 by averaging the optical conductivity  $\sigma$  (Eq. 3.2) over this distribution. The chemical potentials

found are shown next to the curves in Fig. 3.5. The deviations  $\Delta\mu$ 's were found to be less than 0.09 eV, which could be further reduced with a smaller beam size and/or atomically flat substrate surfaces.

We have reproducibly observed that, as the concentration of nitric acid dopants increases, graphene becomes more p-doped. Furthermore, the optical absorption at low photon energies is reduced due to lack of electron population in the valence band. The baked sample (S00) shows nearly universal absorption at photon energies as low as 0.4 eV, which is limited by the spectral range of the spectrophotometer. It should be noted that the chemical doping process adopted here does not cause defects in graphene, as verified with Raman spectroscopy, shown in Appendix B.

### 3.5 Saturable absorption of graphene

The understanding of saturable absorber parameters is critical to the success of stable mode-locking and generation of short pulses. Besides the relaxation time scales of the saturable absorber, it is equally important to characterize how the absorption (equivalently reflection or transmission of the sample) changes as a function of pulse fluence or intensity over 2 to 3 decades. Due to the low saturable loss (typically less than 5%) of the saturable absorbers used for modelocking free space solid state lasers, it can be challenging to keep the non-linearity of the experimental setup to below this value. This is especially true for graphene since it possesses only  $\sim 2\%$  absorption when placed on a transparent glass. The characterization methods for both transmissive and reflective samples are discussed below.

#### 3.5.1 Experimental setup: differential transmission and pump probe

The experimental setup for measuring saturable absorption in this thesis is shown in Fig. 3.6, which is dubbed differential transmission (a) or reflectivity (b) depending on the sample preparation. For graphene placed on a glass slide, the method shown in (a) is suitable since it compares the transmitted power through the graphene sample with a reference beam. The signal is obtained by detecting the differential power with a balanced photodetector, and the intensity can be varied

with a dual-polarizer attenuator. For characterizing reflective samples such as graphene placed on a laser mirror or traditional SESAMs, the setup shown in (b) can be adopted, which was originally demonstrated in [68]. This method avoids the use of two photodiodes, which could add systematic errors. Instead, the detection is performed by one photodiode and a special chopping technique such that both the sample and reference beams can be sampled at almost the same time. The processing is done numerically after digitally sampling the step-function-like signals. Details can be found in [68]. For graphene samples on glass, we adopted the first method shown in (a).

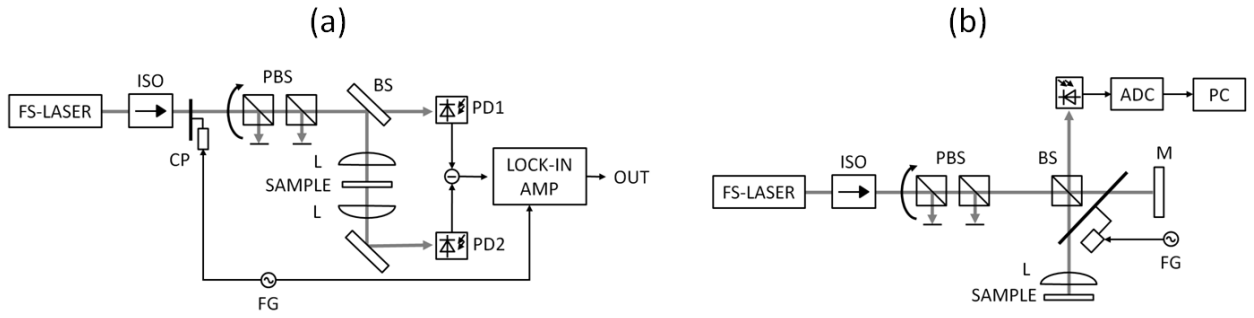


Figure 3.6: Differential transmission setup for characterizing the saturable absorption of graphene. Isolator: optical Faraday isolator; PBS: polarization beam splitter cube, two used as a power attenuator; BS: beam splitter; PD1 and PD2: identical photodiodes for balanced detection; L1 and L2: focusing lenses; Sample: graphene on a microscope slide; Chopper: mechanical chopper used with lock-in amplifier to reject part of the laser noise.

We used a soliton mode-locked Er:Yb:glass laser with a center wavelength of  $1.56 \mu\text{m}$ , pulse width 210 fs, and 86 MHz repetition rate. The beam diameter on the sample was  $(4.4 \pm 0.6) \mu\text{m}$ . For each measurement, the peak intensity of the pulse was varied logarithmically from 3 to over  $3000 \text{ MW/cm}^2$ , and the change of transmittance was recorded. Each sample was characterized at ten independent locations, and the fit parameters of all spots were averaged. Fig. 3.8(a) shows one of these measurements.

We also measured the relaxation time of photo-excited carriers in undoped graphene by a degenerate pump-probe setup with the aforementioned laser. As can be seen in Fig. 3.7(a), the pump and probe beams were counter-propagating, polarized  $90^\circ$  with respect to each other, and

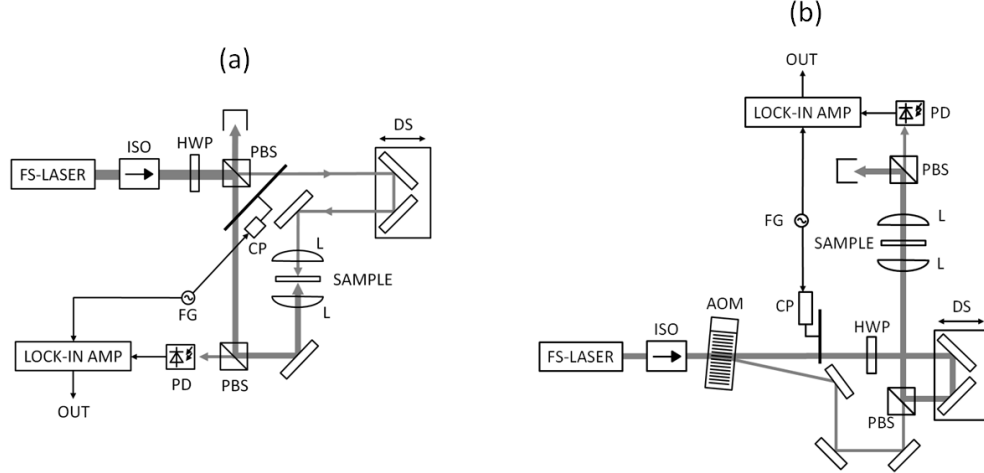


Figure 3.7: Degenerate pump probe setup for measuring carrier dynamics in graphene on a transparent substrate. Isolator: optical Faraday isolator; PBS: polarization beam splitter cube, two used as a power attenuator; BS: beam splitter; PD1 and PD2: identical photodiodes for balanced detection; L1 and L2: focusing lenses; Sample: graphene on a microscope slide; Chopper: mechanical chopper used with lock-in amplifier to reject part of the laser noise.

mechanically chopped at two different frequencies around 1 kHz. The change of probe power due to the pump was measured by a lock-in amplifier at a frequency equal to the sum of the two chopping frequencies. One variation of the setup is also shown in Fig. 3.7(b), where an acousto-optic modulator is used to shift the frequency of the probe beam to avoid the white-light type linear interference between the pump and probe in the photodetector, which could be an issue in the setup in (a) if polarization filtering is not sufficient. Alternatively, a Fourier transform and filter can be applied to the data containing the fast oscillating interference fringes and extract only the slow component, which contains desired carrier relaxation information. The original measurement was performed with the setup depicted in (a), the observed transmission transient of graphene is shown in Fig. 3.8(b).

### 3.5.2 Results and discussion

In graphene, photo-excited carriers relax within  $\sim 200$  fs via carrier-carrier scattering and carrier-phonon scattering [69–72]. Our pump-probe measurements also showed that the fast re-



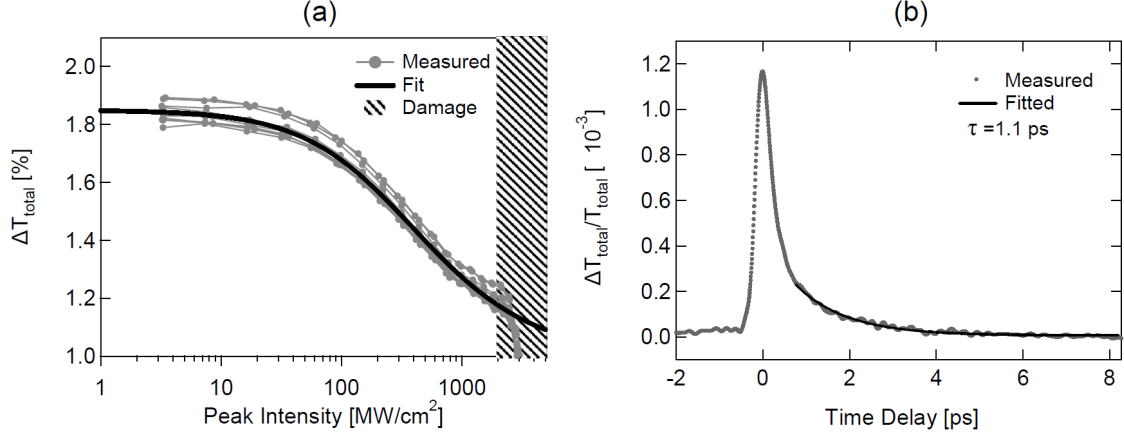


Figure 3.8: (a) The change of transmittance caused by as-transferred graphene as a function of pulse peak intensity. The gray curves are ten individual measurements at different locations on the same sample; the black solid line is the resulting curve from the average of ten individual fits through the data. (b) Transmission transient of graphene. The slow component of the relaxation time is 1.1 ps; the fast component is not resolved due to the long pulse duration ( $\sim 210$  fs).

laxation in graphene contributes significantly to the saturable absorption (Fig. 3.8(b)). To find the macroscopic parameters of a graphene absorber (saturation intensity or fluence, saturable loss, and non-saturable loss), care needs to be taken in fitting a correct theoretical model to experimental saturable absorption curves. The saturation of an absorber can be described by the following equation (Eq. 2.10):

$$\frac{dq(t)}{dt} = \frac{q_0 - q(t)}{\tau_A} - \frac{q(t)I(t)}{F_{\text{sat},A}}, \quad (3.5)$$

where  $q(t)$  is the saturable loss,  $q_0$  is the insertion loss,  $\tau_A$  is the relaxation time of the absorber,  $I(t)$  is the intensity of light, and  $F_{\text{sat},A}$  is the saturation fluence of the absorber. For simplicity, we first regard graphene as a fast saturable absorber (pulse width  $\gg \tau_A$ ). Given sech<sup>2</sup>-shaped pulses, the loss of absorber can be written as (Eq. 2.13)

$$q(S) = \frac{q_s}{\sqrt{S(1+S)}} \tanh^{-1} \left( \sqrt{\frac{S}{1+S}} \right) + q_{ns}, \quad (3.6)$$

where  $q_s$  is the saturable loss,  $q_{ns}$  is the non-saturable loss, and  $S$  is the ratio of the pulse peak intensity to the saturation intensity of the graphene absorber. Fig. 3.8(a) shows the nonlinear absorption curve of as-transferred and baked samples. Fitting Eq. 3.6 to the data, we found the

saturation intensity to be  $(250 \pm 80)$  MW/cm<sup>2</sup>, the insertion loss  $(1.85 \pm 0.08)\%$ , the saturable loss  $(0.85 \pm 0.04)\%$ . It should be noted that the insertion loss here refers to the change of transmittance due to the presence of graphene on the air-glass interface, and it is lower than the optical absorption of free-standing graphene ( $\pi\alpha = 2.3\%$ ). The insertion loss was comparable to the calculated change of transmittance  $\Delta\mathcal{T}_{total} = 1.7\%$  in Eq. 3.4. The extra loss could be attributed to the light scattering from graphene or non-graphitic carbon produced incidentally by the CVD process [73].

From a full numerical solution to Eq. 3.5, assuming  $\tau_A = 200$  fs,  $\text{sech}^2$ -shaped pulses with 210 fs (FWHM), we found that the saturation intensity was lower by a factor of 0.7 ( $I_{sat} = 175$  MW/cm<sup>2</sup>,  $F_{sat} = 35$   $\mu$ J/cm<sup>2</sup>), although in this regime, neither the saturation intensity nor fluence is a good macroscopic quantity of the absorber. One simply needs to refer to the pulse duration and the relaxation time of the absorber.

The saturation intensity we measured can be directly compared with the theoretical value calculated by Vasko [74]. For photon energies near 0.8 eV, the theoretical value is approximately 60 MW/cm<sup>2</sup>, and our measured value of  $(250 \pm 80)$  MW/cm<sup>2</sup> agrees roughly within a factor of 4. The discrepancy between our measurement and the theoretical value could be due to the reduced carrier relaxation time (Fig. 3.8(b)) caused by the lattice defects around domain boundaries or by the interaction with the substrate, which could add additional relaxation pathways. Note that none of these effects can lower the measured saturation intensity.

Our result also agrees very well with Sun et al. [75], who measured the saturation intensity for 1.55  $\mu$ m light to be 266 MW/cm<sup>2</sup> for monolayer and bilayer graphene flakes dispersed in polymers, but we found a large discrepancy between our results and the values reported by Bao et al. [57, 76, 77], Tan et al. [78], and Zhang et al. [79–81], who found a saturation intensity value of 0.6-0.7 MW/cm<sup>2</sup>. Even though their measured saturation intensity seemingly agrees with the model they suggested [57], their model merely accounted for the carrier recombination in direct band-gap semiconductors such as gallium arsenide, but is likely not adequate to describe zero-bandgap graphene.

It may be argued that the saturation intensity depends on the pulse duration used for characterization, but from a full numerical solution to Eq. 3.5, we found that as the pulse duration

increases from 200 fs to 10 ps, the saturation intensity decreases by a factor of at most 10, which could not explain this discrepancy.

According to Vasko's calculation, the saturation intensity strongly increases with the photon energy due to the proportionality between the relaxation rate and the density of states to which carriers are excited. Several experiments have also shown that the saturation intensity for 800 nm light is above 1 GW/cm<sup>2</sup>: Dawlaty et al. observed saturable loss but could not reach the saturation intensity even at pulse peak intensities higher than 1 GW/cm<sup>2</sup> (85 fs pulse duration) [69]; Xing et al. showed by z-scan measurements that the saturation intensity was near 4 GW/cm<sup>2</sup> [72]; and Breusing et al. did not observe any saturation with pulse fluence as high as 0.7 mJ/cm<sup>2</sup> (7 fs pulse duration) [71].

### 3.5.3 Saturable absorption in chemically-doped graphene

The transmission spectra of undoped and doped graphene are shown in Fig. 3.5. As the Fermi level was varied from close to the Dirac point to 0.4 eV below the Dirac point, the linear absorption at low photon energies decreased due to state blocking. The corresponding saturation of optical absorption at 1.55  $\mu\text{m}$  wavelength (0.8 eV) is shown in Fig. 3.9. As the doping level increased, the insertion loss of graphene decreased dramatically from 1.8% to 1%, which matched well with the measured linear absorption.

The non-saturable loss, however, did not increase with the doping level, suggesting that doping with nitric acid does not cause more defects or introduce more scattering loss to the graphene. The saturation intensity also remained roughly the same in doped graphene, which could be understood from the fact that the density of states and carrier relaxation time are not modified by hole-doping.

This flexibility in designing the saturable absorbers is essential to successful continuous-wave mode-locking in solid-state lasers [82]. Given the parameters of a specific laser, suitable parameters of the saturable absorber can be chosen to prevent Q-switching. SESAMs have been used widely in solid-state laser mode-locking because of their design freedom. For graphene absorbers, one

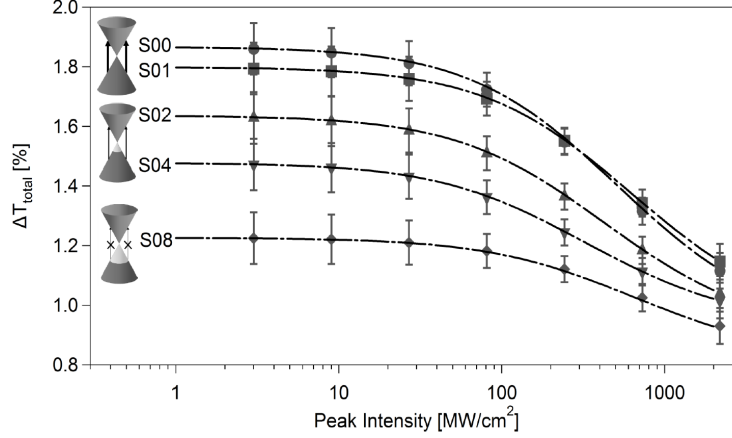


Figure 3.9: Transmission loss of doped graphene as a function of pulse peak intensity. For each doping level, one curve (dashed line) obtained by averaging the fit parameters of ten independent spots is shown. From top to bottom, the curves represent (S00) baked graphene, (S01) baked and doped by 0.1wt% acid, (S02) baked and doped by 0.2wt% acid, (S04) baked and doped by 0.4wt% acid, (S08) baked and doped by 0.8wt% acid. The three cones show the band structure of graphene at different doping levels. Upper cone: conduction band; Dark lower cone: electron-filled valence band; and light-colored area: hole-occupied states.

can exploit the doping effect to tailor the modulation depth in monolayer graphene, and if higher insertion loss is desired, stacked multilayer graphene can be used.

Even though the parameters of a saturable absorber can be tailored to specific values in order to prevent Q-switching, the allowed range of parameters is often quite limited, and the parameters of the laser such as gain cross section and pump power also need to be taken into account. In certain situations, using active feedback to suppress Q-switching can be favorable compared to designing absorbers. It has been demonstrated that the laser output power can be directly used to feedback-control the intracavity loss or gain [83, 84]. For graphene absorbers, it is possible to implement an external electric field to modulate the carrier density [62, 85], or essentially the Fermi level, so that the insertion loss can be controlled by electronics. The relation between the carrier density( $n$ ) and Fermi level( $E_F$ ) in graphene is given by

$$n = \frac{1}{\pi} \left( \frac{E_F}{\hbar v_F} \right)^2, \quad (3.7)$$

where  $v_F$  is the Fermi velocity ( $\sim 10^6$  m/s). To achieve the maximal modulation of insertion loss in a laser with a center wavelength of  $1.55 \mu\text{m}$ , the desired Fermi level is 0.4 eV below the Dirac

point, corresponding to a carrier (hole) density of approximately  $10^{13} \text{ cm}^{-2}$ . To achieve this level of carrier density in a normal electrical-gating configuration with 100 nm dielectric of  $\epsilon \approx 4$ , one has to apply nearly 100 Volts. Doping graphene with chemicals prior to applying electric fields can thus avoid the use of strong field and avoid dielectric breakdown. This pre-doping would be particularly important for applications in lasers with wavelengths in the near-infrared and visible regions, where the state-blocking is not trivial to achieve solely by electric-field gating.

### 3.6 Optical damage of graphene

The modulation depth and the saturation intensity of graphene are comparable to those of SESAMs [38]. However, the full modulation depth could not be exploited due to the onset of permanent damage for pulse peak intensities higher than  $2 \text{ GW/cm}^2$ . We found that the damage resulted from the high peak power of the laser rather than from the heat due to the average power. This was confirmed by observing the damage with the laser under two conditions: (1) cw mode-locking regime and (2) continuous-wave regime. While the average power was the same in both regimes, the peak power was 50,000-times higher in the mode-locked regime. Despite having the same average power as in the cw modelocked regime, no damage was observed when the laser was operated in the continuous-wave regime. To further investigate the damage mechanism, the graphene sample was purged with argon, excluding the possibility of oxygen interacting with graphene under high pulse intensity. It was found that the damage threshold did not increase in this oxygen-free environment. We thus assume that the damage could have originated from the interaction of the high electric fields with graphene and possibly its residual surface contaminants or non-graphitic carbon left over from growth and transfer [73].

### 3.7 Modelocking of an Er:Yb:glass laser with graphene

Modelocking a low gain solid state laser was achieved with a CVD graphene sample transferred to a laser broadband mirror. The CVD growth process is similar to the one described in Section 3.4.2. The only difference is that graphene was directly transferred onto a broadband laser

mirror. Fig. 3.10(a) shows a photo of transferred graphene on a broadband, dielectric-coated mirror. Fig. 3.10(b) shows a microscopic picture of the transferred graphene, and it can be seen that graphene is uniform over most of the region. Only a few dark spots exist possibly due to multi-layer graphene or copper etchant residue. The uniformity of this large-area graphene reduces the non-saturable scattering loss of laser light. Also, focused laser light can be aligned on the sample easily without using a microscope, which is important for applications in solid-state bulk lasers.

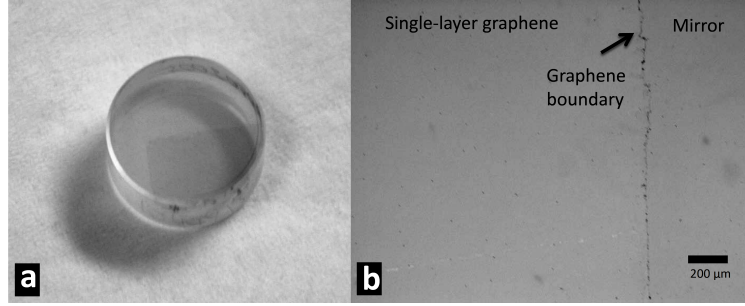


Figure 3.10: (a) Graphene saturable absorber mirror: Directly transferred graphene on a broadband laser mirror with 1/2 inch diameter. The contrast of the picture is enhanced for clarity. (b) Optical microscopic view of single-layer graphene on a laser mirror showing good uniformity.

We built a laser based on Er:Yb:glass (Kigre Inc.: QX/Er, 1%Er, 20%Yb, 1.6 mm plate under Brewster angle). The laser glass was directly diode pumped by a pigtailed single transversal mode and single wavelength 980 nm laser diode. The cavity was an astigmatically compensated, X-fold cavity with an additional focus on one of the end mirrors, which was replaced by the graphene-based saturable absorber mirror (Graphene-SAM), as shown in Fig. 3.11(a). The chromatic dispersion of the cavity was dominated by the anomalous second-order dispersion of the laser glass. All cavity mirrors were commercial, low-dispersion broadband mirrors. The pulse repetition rate was 88 MHz. At an output coupling ratio of 0.4% and a pump power of about 130 mW stable mode-locking at 4.5 mW output power ( $\sim 1.1$ W intracavity power) at a center wavelength of around 1550 nm was obtained. The mode-locked spectrum is shown in Fig. 3.11(b). From an autocorrelation measurement, we inferred a pulse duration of 260 fs, assuming a Gaussian pulse shape. The beam diameter on the saturable absorber was  $\sim 30 \mu\text{m}$ , resulting in a maximum peak-intensity of  $\sim 6$

GW/cm<sup>2</sup>.

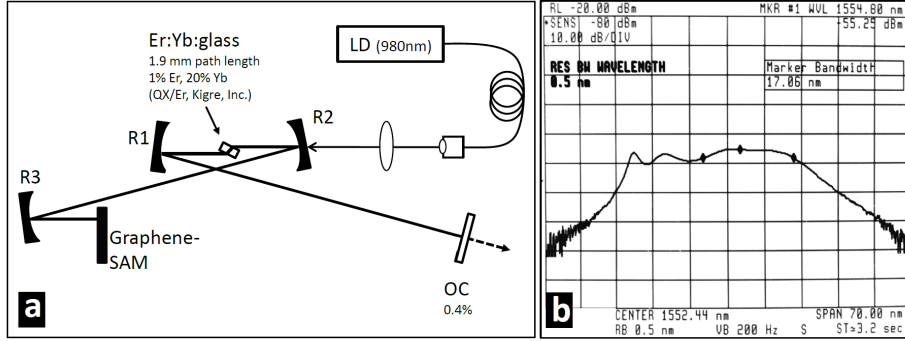


Figure 3.11: (a) Diode-pumped Er:Yb:glass laser cavity configuration. R1, R2, and R3 are concave broadband laser mirrors with ROC = 100 mm, 100 mm, and 50 mm, respectively. (b) Output optical spectrum. Spectral width  $\sim 17$  nm at a center wavelength of around 1550 nm. Resolution bandwidth: 0.5 nm.

### 3.8 Conclusion

In this Chapter, we reviewed the basic optical properties of graphene. Graphene has a linear energy to momentum relaxation for its carriers, which can be either holes or electrons (ambipolar), depending on the Fermi level. Both its linear and nonlinear optical absorption can be modified by changing the doping level, which was demonstrated here with a chemical mean but an electrical gating method will be the topic of Chapter 4.

Graphene as a saturable absorber exhibits a saturation intensity of  $(250 \pm 80)$  MW/cm<sup>2</sup> for 1.5  $\mu$ m light, which is comparable to some reported values but a large discrepancy (two orders of magnitude) exists still to date between this result and the results reported by the first graphene modelocking result. Due to the onset of optical damage at above 2 GW/cm<sup>2</sup>, the operating intensity range for graphene is rather tight, and long term operation with graphene could not be achieved in our Er:Yb:glass laser. At mid-IR wavelengths, graphene may serve as a better saturable absorber than at near-IR wavelengths because of its lower saturation intensity, which scales with the photon energy in a nonlinear fashion due to the lower density of states and higher photon flux per unit

optical power at long wavelengths.

Graphene may not rival, at least for now, the well-established SESAM technology at near-IR wavelengths due to its high saturation intensity and susceptibility to optical damage, despite its very short relaxation time and ease of fabrication. In the next Chapter, the use of graphene as an active device will be discussed. Based on its tunable linear optical absorption, coupled with its high saturation intensity (suitable for high peak power applications), graphene could serve as a fast electro-optic loss modulator for laser applications with extremely broad optical and electrical bandwidths.



## Chapter 4

### Graphene as an electro-optic modulator

#### 4.1 Motivation

As discussed in Chapter 3, graphene is a single sheet of carbon atoms arranged in a honeycomb structure. A unique property of this two-dimensional lattice structure is that the electrons are nearly massless due to their linear dispersion relation between energy and crystal momentum [86]. Moreover, free-standing graphene absorbs electromagnetic radiation ranging from THz waves to visible light, with a wavelength-independent range of:  $\pi\alpha = 2.3\%$ , where  $\alpha$  is the fine structure constant [87].

An very important consequence of its band structure is that the density of states around the Dirac point, where the conduction and valence bands in graphene meet, is close to zero. This property makes the optical absorption of graphene at low photon energies very sensitive to the occupation of electronic states near the Dirac point, which is mostly subject to finite temperature-induced broadening and/or substrate-induced doping [88]. Since the carrier-density in graphene can also be actively controlled by an external electric field in a field-effect-transistor-like structure [67], one can utilize the doping-dependent optical absorption to gain active control over the linear optical properties of graphene at mid-IR wavelengths [85, 89].

To exploit this tunable absorption in graphene for electro-optic modulation in the near-IR or visible portion of the spectrum, one needs to substantially increase the carrier density and/or the interaction between the light and the graphene. Efforts have been made to evanescently couple light in a silicon waveguide to graphene [90]. Despite its high modulation speed ( $\sim 1$  GHz), a

waveguide-type modulator limits the range of applications. In particular free-space applications that require low insertion loss, such as amplitude modulation in a high-Q laser cavity or in an active interferometer, would suffer from the inevitable coupling loss to the optical waveguide.

In this Chapter, we show the fabrication and characterization of a new type of graphene-based electro-optic modulators with low insertion loss, high modulation speeds, and large active areas for free-space laser applications, particularly for intracavity use in low loss solid state lasers.

Because of the ultra-thin character of graphene, new types of electro-optic modulators can be realized using graphene as a loss-tunable layer embedded inside a multilayer structure. With the advantage of the large design freedom that multilayer coatings offer, parameters of these graphene-based modulators, such as their insertion loss and modulation depth, can be optimized to meet the requirements of the application at hand.

The electro-optic modulators that we demonstrate here are, to the best of our knowledge, the first graphene-based modulators that are fabricated in a planar, reflective-type structure that can be readily deployed in lasers or active interferometers to gain direct control over their intra-cavity dynamics. This could enable active mode-locking, carrier-envelope phase control, or suppression of noise and Q-switching instabilities [23, 91]. These novel graphene devices are not only advantageous due to their compactness, but also due to their polarization insensitivity, ultra-low phase distortion, and their low drive-voltage requirements compared to established LiNbO<sub>3</sub>-based modulators. Since these devices can be made with a large active area with uniform modulation, they enable scaling for high-power applications.

## 4.2 Physics of electro-absorption modulation in graphene

The absorption of graphene is determined by its optical conductivity [61]. This has been discussed in Section 3.4:

$$\sigma = \sigma_0 \frac{1}{2} \left( \tanh \frac{\hbar\omega + 2\mu}{4k_B T} + \tanh \frac{\hbar\omega - 2\mu}{4k_B T} \right), \quad (4.1)$$

where  $\sigma_0 = e^2/4\hbar$  is the optical conductivity of undoped graphene (i.e. with a Fermi-energy  $E_F = 0$ ),  $k_B$  is the Boltzmann constant,  $e$  is the electron charge,  $\hbar$  is the reduced Plank constant,  $T$  is the effective carrier temperature, and  $\omega$  is optical frequency. The absorbed optical power in graphene is approximately proportional to its optical conductivity. A change in graphenes Fermi level therefore changes the optical absorption at certain optical frequencies [85, 90].

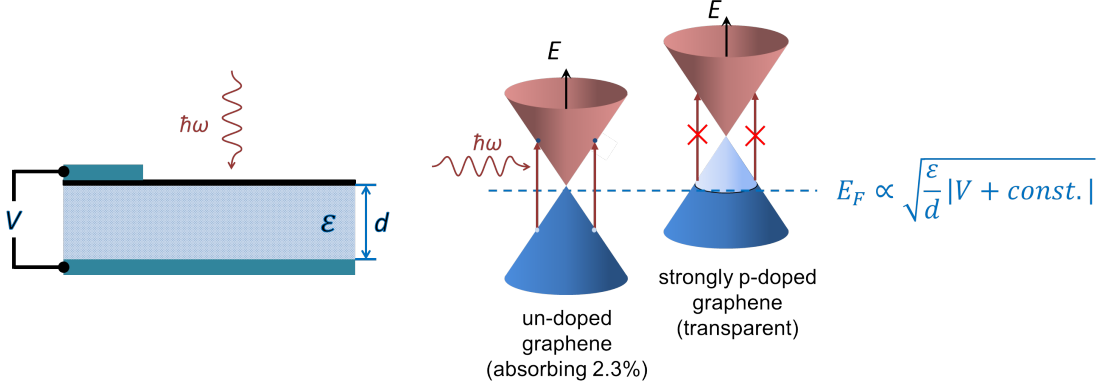


Figure 4.1: Tuning of the optical absorption of graphene by electric field-gating. Left: Graphene on a gated dielectric with thickness  $d$  and dielectric constant  $\epsilon$ . Right: Excitation of electrons from the valence band (blue cones) to the conduction band (red cones) through absorption of a photon. The absorption is blocked when graphene is strongly doped (either n- or p-doped; only p-doping is shown here). For a given voltage higher or lower  $d$  result in larger tuning of  $E_F$ . ‘const’ refers to the negative value of the charge-neutrality voltage of the device.

The charge density of electric-field-gated graphene (see Fig. 4.1, left) scales linearly with the applied voltage ( $V$ ) and the dielectric constant ( $\epsilon$ ), and it is inversely proportional to the thickness ( $d$ ) of the dielectric (parallel-plate capacitor model). The charge density relates to the Fermi energy ( $E_F$ ) of graphene and further to the applied voltage by

$$E_F \propto \sqrt{|n + n_0|} \propto \sqrt{\frac{\epsilon}{d}} |V + V_0|,$$

where  $n_0$  is the doping concentration present in graphene due to the graphene-substrate interaction. To simplify the understanding of the voltage-dependence of the device, one could think of this doping concentration  $n_0$  as being caused by an auxiliary voltage  $V_0$ . As the magnitude of the Fermi energy approaches half the photon energy  $\hbar\omega$ , the optical conductivity in graphene changes from

$\sigma_0$  (corresponding to the aforementioned 2.3% optical absorption) to  $\sigma_0/2$ . For  $|E_F| > \hbar\omega$  the conductivity and the optical absorption approach zero (see Fig.4.1, right).

Graphene on dielectric substrates is typically only shallowly p-doped ( $\sim 100 - 200$  meV) [88]. Therefore, fairly high voltages are required for shifting the Fermi energy beyond the desired half of the photon energy ( $\hbar\omega \sim 400$  meV for telecommunications wavelengths). For example, 200 meV pre-doped graphene on a 100 nm silicon dioxide layer ( $\epsilon = 3.9$ ) requires  $\sim 55$  V to reach an  $E_F \sim 400$  meV. The use of high-k dielectrics such as  $\text{Ta}_2\text{O}_5$  ( $\epsilon = 22$ ) can thus substantially decrease the required drive voltage ( $< 10$  V in the example above).

### 4.3 Device implementation

#### 4.3.1 Design

Fig. 4.2(a) shows the structure of a graphene electro-optic modulator. A sapphire substrate was first coated with a 20-nm titanium adhesion layer and a 100-nm silver film by thermal evaporation. A 20-nm layer of silicon nitride was coated readily after the deposition of the silver in order to prevent oxidization. The resulting silver film provides high reflectivity ( $> 98\%$ ) for infrared light at normal incidence and also functions as a back gate electrode. Tantalum pentoxide ( $\text{Ta}_2\text{O}_5$ ) was deposited on the silver mirror as the gate insulator by dc reactive magnetron sputtering with a tantalum target.

The thickness of this  $\text{Ta}_2\text{O}_5$  layer is one of the design degrees of freedom that can be used to tailor the optical properties of the device to the required specifications. By placing the graphene at the appropriate location in the standing wave that is formed between the incident light and the light that was reflected from the silver back-gate electrode, one can tailor the insertion loss and achievable modulation strength of the device. Hence, a careful adjustment of the thickness of the  $\text{Ta}_2\text{O}_5$  layer can alter the graphene absorption from essentially zero (if the optical thickness of the  $\text{Ta}_2\text{O}_5$  layer is chosen to be  $\lambda/2$ ) to approximately 8% (for  $\lambda/4$ ).

For any multilayer structure with embedded graphene, modified Fresnel transfer matrices can

be used to calculate the insertion loss of the structure and the effective optical absorption of the graphene. The transmission and reflection coefficients at normal incidence of a planar dielectric interface (initial and final medium with index  $n_1$  and  $n_2$ , respectively) with undoped graphene are [61]

$$\begin{aligned} t_{12} &= \frac{2n_1}{(n_1 + n_2 + \pi\alpha)}, \\ r_{12} &= \frac{(n_2 - n_1 + \pi\alpha)}{(n_2 + n_1 + \pi\alpha)}. \end{aligned} \quad (4.2)$$

For the whole device structure shown in Fig. 4.2, the relevant refractive indices are: 2.1 for the 225 nm thick  $\text{Ta}_2\text{O}_5$  layer; 1.8 for the 20 nm thick  $\text{SiN}_x$  layer; and  $n = 0.51 + 10.8i$  for silver at 1.55  $\mu\text{m}$  wavelength. Using the Fresnel transfer-matrix method we find that the total insertion loss (including graphene absorption) of the modulator shown in Fig. 4.2(b) is 5.1% and the electric field-induced modulation depth is 2.1%; assuming the graphene could be fully bleached.

The maximum reflectivity of this simple design is limited by the reflectivity of silver mirror. If further reduction of the insertion loss is required, for example for applications inside a high-quality-factor optical cavity, one could add a top reflector formed by a stack of dielectric quarter wave layers. For instance, by adding a single layer of quarter-wave thickness ( $\text{TiO}_2$ ,  $n = 2.5$ ) on the graphene would reduce insertion loss down to less than 3.0%, and more than half of this loss could still be actively controlled.

#### 4.3.2 Fabrication

We used monolayer synthetic graphene of large, connected single-crystal domains with sizes 20  $\mu\text{m}$  grown by low-pressure chemical vapor deposition (CVD) on a copper foils [92]. A large sheet of graphene ( $\sim 1\text{cm}^2$ ) was subsequently wet transferred from the copper foil onto the  $\text{Ta}_2\text{O}_5$  layer with the mechanical support of spin-coated polymethyl methacrylate (PMMA) film. After the transfer and removal of the PMMA film the device was baked in a  $\text{N}_2$  (90%) and  $\text{H}_2$ (10%) atmosphere at ambient pressure and 200 °C. for an hour. This baking removed the residual PMMA and water from the wet-transfer process. The use of CVD-grown graphene enables the fabrication

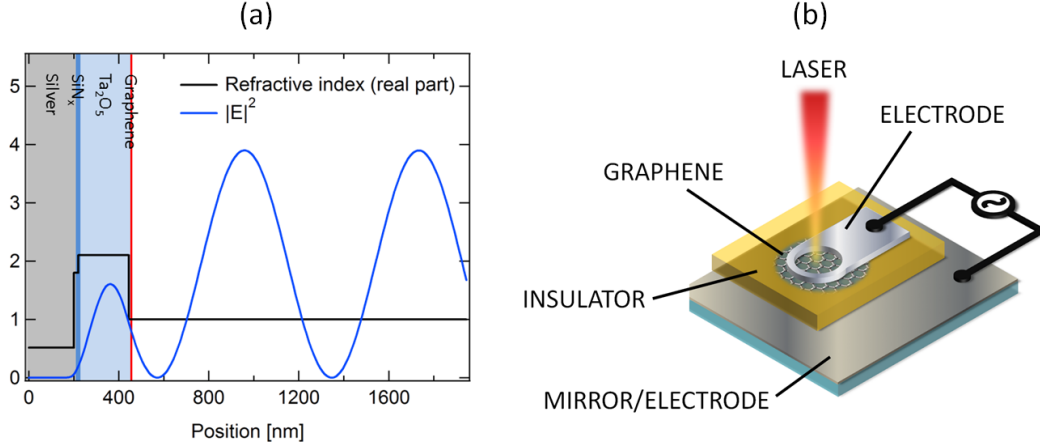


Figure 4.2: (a) Electric-field-square distribution (blue line) in the multilayer structure for  $1.55 \mu\text{m}$  wavelength light at normal incidence. ( $|E|^2$  was normalized to 1 for the travelling incoming wave). The black curve represents the refractive index of each layer. Here, the layer thickness of  $\text{SiN}_x$  is 20 nm;  $\text{Ta}_2\text{O}_5$  is 225 nm, and  $|E|^2$  on graphene is 0.94, yielding a maximum loss of 5.1%, of which 2.1% are absorbed by the undoped graphene. (b) Sketch of the device structure. Silver functions as the back gate and mirror. A 225-nm-thick  $\text{Ta}_2\text{O}_5$  layer serves as the gate insulator and the substrate for the graphene. The top contact on the graphene is formed by a ring-shaped Ti/Al electrode. Graphene outside the top contact annulus was removed by oxygen plasma to minimize the device capacitance.

of graphene modulators with large active areas; something that would likely be impossible with exfoliated graphene. Even though CVD-grown graphene has domain sizes around  $20 \mu\text{m}$ , and the domain boundaries substantially increase the electrical sheet resistance, we show in the following sections that the modulation effect from these modulators exhibit good uniformity over the whole active area.

To electrically contact the graphene we used a lift-off process to deposit a metal-annulus consisting of a 20 nm titanium wetting layer and a 200 nm aluminum conductive layer. The contact resistance between these top electrodes and the graphene was measured to be 200-500 Ohms, which is believed to limit the current speed of the device due to the resulting RC time constant. The top contacts were chosen in the depicted ring-shape (Fig. 4.2(b)), as this shape provides a good compromise between the low-pass effects caused by the contact and sheet resistance, yet it does not substantially add to the capacitance of the device. With this top-contact geometry, the device

capacitance scales approximately linearly with the device active area, and hence, we expect that larger devices will likely exhibit a slower electrical response. After the top electrode deposition, excess graphene outside of the ring electrodes were removed by oxygen plasma to minimize the parasitic parallel capacitor that would otherwise be generated by the excess graphene outside the top-contact annulus. All the following characterization was done at ambient conditions with graphene exposed to air.

### 4.3.3 Characterization

We characterized the modulation depth of our graphene modulators by a continuous-wave laser at  $1.55\ \mu\text{m}$  wavelength. The modulation effect over the whole area of the device is characterized with two linear motorized stages arranged in an orthogonal x-y configuration. The laser beam was focused onto the device with a spot size  $\sim 5\ \mu\text{m}$  diameter. The reflected beam was sent into a photodiode, and the amplitude modulation and phase changes were extracted with a lock-in amplifier while the stages were scanning in discrete steps (step size  $2\ \mu\text{m}$ ) Fig. 3. In addition to these 2D scans, we also measured the frequency response of the modulator at a fixed location inside the active area with two lock-in amplifiers (Stanford Research SR830 for measurements from 0.1 Hz to 100 kHz, and a Stanford Research SR844 for measurements from 25 kHz to 100MHz; Fig. 4a). During all these measurements the light intensity on the device was kept low ( $< 5\text{kW}/\text{cm}^2$ ), such that no nonlinear optical absorption could occur in the graphene sample.

Fig. 4.3 shows the two-dimensional scans for various modulation frequencies. It can be seen that the whole active area with a diameter of 100  $\mu\text{m}$  has high spatial uniformity, especially when considering that the used CVD-graphene has domain sizes of  $\sim 20\ \mu\text{m}$ , and that several photolithographic and wet fabrication processes were performed on the graphene surface. The two-dimensional maps also show that the performance of the device remains essentially the same over the whole tested frequency range from 100 kHz up to 50 MHz, despite the slightly increased RF background above 10MHz.

The measured insertion loss of the modulator was found to be 7%, of which 2% were from

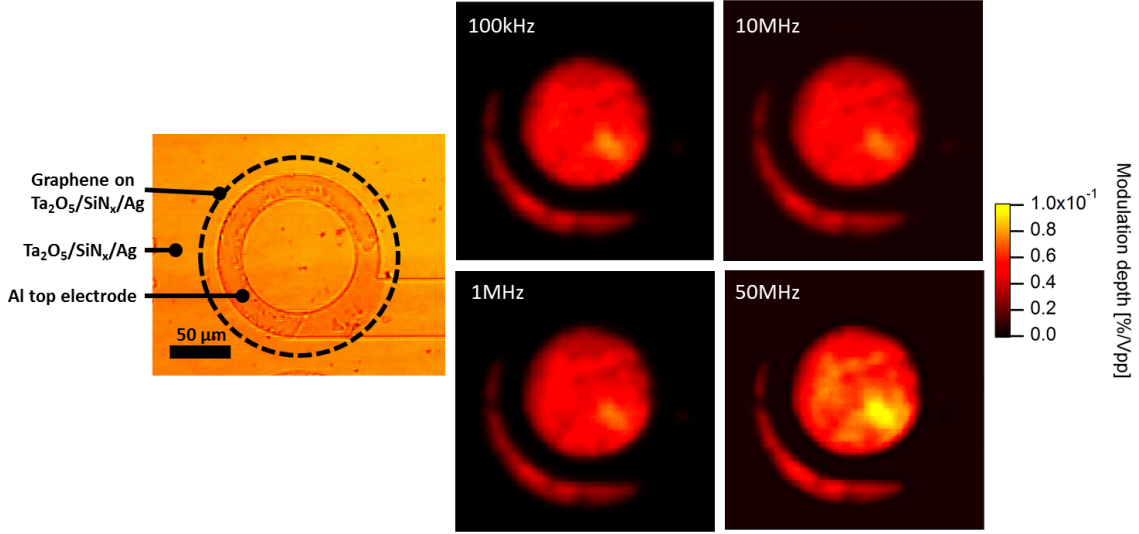


Figure 4.3: (Left) Optical microscope image of the modulator. (Right) Modulation depth measured by two-dimensional scans over the active area of the graphene modulator at various driving frequencies. The modulation depth is calibrated to the incident laser power; the driving voltage was 1Vpp (square wave).

the absorption of graphene. This slightly higher insertion loss compared to the calculated value based on the aforementioned transfer-matrix method could be attributed to the scattering loss from graphene and small thickness errors in the deposition steps. Nearly 50% of the insertion loss of the graphene could be modulated with only 5 Vrms.

To verify the aforementioned design freedom we fabricated a second device with a quarter-wave layer of Ta<sub>2</sub>O<sub>5</sub>. For that device the insertion loss was found to be 15% with 7% modulation depth, which is in excellent agreement with the calculated values above. In this device the modulation was an astonishing 1% (or 0.1dB) per 1 Vrms. This is particularly impressive when considering that this strong modulation occurs within the single atomic layer graphene. Since the full modulation effect occurs in the one atomic layer, one can expect that this constitutes a pure amplitude modulator, i.e. an amplitude modulator with negligible parasitic phase modulation.

The frequency response of the modulator is shown in Fig. 4.4. The modulator has an estimated capacitance around 7 pF and contact resistance of the order of 200 Ohm, which corresponds to a theoretical -3dB corner of 114 MHz. The -3dB corner was indeed not observed for frequen-



cies up to 100 MHz. Frequency measurements above 100 MHz were hindered by RF coupling and impedance mismatch. It should be noted that we observed a slight roll-off of in the modulator response at frequencies below 1Hz. We hypothesize that this decrease could be attributed to a hysteresis caused by the substrate or the water molecules in the substrate, as observed previously in graphene transistors [13].

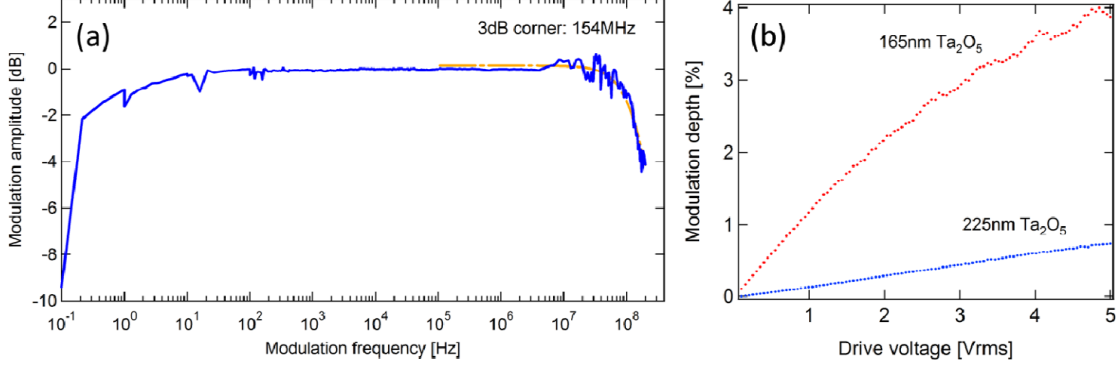


Figure 4.4: (a) Frequency response of the graphene modulator with 225-nm Ta<sub>2</sub>O<sub>5</sub> dielectric (blue: experimental, orange: fit). The 3dB corner was found to be 154 MHz. The small fluctuations of the modulation amplitude near the frequency corner were found to be caused by RF background coupling. An amplitude roll-off at frequencies lower than 1 Hz was observed and believed to be related to the hysteresis effects caused by the underlying oxide layer [13]. (b) Modulation depth as a function of the RMS amplitude of the 100 kHz driving sine wave. The driving voltage was 1V<sub>pp</sub> (square wave).

## 4.4 Integration with a III-V semiconductor saturable absorber mirror

### 4.4.1 Motivation

Modelocking-based frequency combs have been evolving rapidly in the last two decades from the classic Ti:sapphire bulk lasers to compact fiber-based lasers. This decades long effort in miniaturizing combs has reached a point where portable and fieldable applications are possible [93,94]. When one considers the available modelocking techniques that are feasible for turn-key, polarization-maintaining, and self-starting operation, the use of semiconductor saturable absorber mirrors (SESAMs) is favored in many cases. While the use of SESAM allows straightforward mod-

clocking of a compact laser, two fast actuators are needed to suppress the noise in both the pulse repetition frequency ( $f_{\text{rep}}$ ) and the carrier envelope offset frequency ( $f_{\text{ceo}}$ ). For metrological, long-term ( $> 1\text{ s}$ ) applications, slow actuators are often sufficient. However, when short-term stability ( $1\text{ }\mu\text{s}$ – $1\text{ s}$ ) is of concern, high bandwidth is required, for instance in the generation of ultralow-noise microwaves by direct frequency division, or in the generation of high-order harmonics with an enhancement cavity. To stabilize  $f_{\text{rep}}$ , one can use a fast piezo or a lithium-niobate-based modulator that controls the cavity length, with up to  $\sim 300\text{ kHz}$  bandwidth. Stabilize  $f_{\text{ceo}}$  by the traditional method of pump power modulation has fairly limited bandwidth due to the long stimulated gain lifetime. A number of high-bandwidth approaches have been shown, including extra-cavity error correction with an acoustic-optic modulator ( $f_{\text{-3dB}} \sim 250\text{ kHz}$ ) [95], intracavity loss modulation with a graphene modulator ( $f_{\text{-3dB}} \sim 1\text{ MHz}$ ) [96] (Chapter 5), and opto-optical modulation with a SESAM ( $f_{\text{-3dB}} \sim 100\text{ kHz}$ ) [97]. We demonstrate a new generation of graphene electro-optic modulators that are integrated with a SESAM. This monolithic device provides electro-optic loss modulation from graphene as well as nonlinear saturable loss from an erbium-doped InGaAs quantum well. We envision the use of this novel device in compact, fieldable frequency combs where ultralow ( $< 100\text{ mrad}$ ) integrated phase noise level is required, such as a portable low-noise microwave generator.

#### 4.4.2 Fabrication and characterization

The structure of the device is shown in Fig. 4.5. The device consists of 24 pairs of GaAs/AlAs  $\lambda/4$  layers that form a highly reflective mirror, a low temperature grown 10-nm-thick InGaAs:Er quantum well, a cap GaAs layer, and a graphene modulator. The quantum well absorber was designed for modelocking at the center wavelength of 1560 nm, and ultrafast recombination centers were introduced in the absorber by erbium doping during the molecular-beam epitaxy for fast recovery time. With a 1560 nm, 80 fs, 88 MHz modelocked laser and a pump-probe setup, the recovery time was found to be bi-exponential, with time constants around 1 ps and 5 ps, while the saturable and non-saturable loss ratio was found to be 0.88% and 0.42%, respectively, which is favorable for modelocking ultra-low-loss bulk lasers. We have successfully used this SESAM in

Er:Yb:glass lasers for sub-100 fs pulse generation, with repetition rates ranging from 80 MHz to 500 MHz. The cap layer, 110 nm of GaAs, is slightly doped during the growth, and the doping concentration is estimated to be around  $10^{15} \text{ cm}^{-3}$ . This layer serves as a transparent electrode for the graphene modulator. The graphene modulator has a 50-nm-thick  $\text{Ta}_2\text{O}_5$  as the gate insulator, 100-nm top gold contact, and monolayer graphene transferred from a chemical-vapor-deposition-grown sample. Note that one can choose the thickness of the high-k dielectric to tailor the insertion loss contributed by graphene and the corresponding modulation depth. In this particular device,

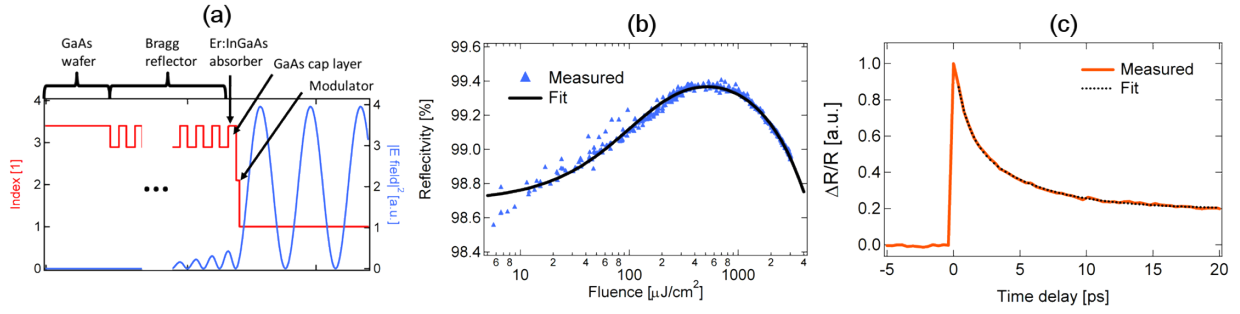


Figure 4.5: (a) Schematic of the device structure. The electric field is calculated for 1560 nm wavelength of light. (b) Reflectivity of the as-grown semiconductor saturable absorber as a function of incident pulse fluence. Saturable loss and non-saturable loss is 0.88% and 0.42%, respectively, and the saturation fluence is  $62 \mu\text{J}/\text{cm}^2$ . The laser used for characterization emits 80 fs pulses at 88 MHz repetition rate. (c) Pump probe characterization of the carrier relaxation dynamics in the absorber. The relaxation times are found to be  $\sim 1$  ps and  $\sim 5$  ps with a bi-exponential fit.

high uniformity of modulation depth (0.04% with 5 Vrms amplitude applied) was observed across an aperture of  $\sim 120 \mu\text{m}$ , shown in Fig. 4.6(b), which was characterized by raster scanning a tightly focused low-power continuous-wave laser centered at 1550 nm while recording the percentage of modulation in the reflected optical power. Fig. 4.6(c) shows the high reflectivity of the device. The added loss from graphene was estimated to be 0.7%, and the total insertion loss of the device is 2%, with 1.3% contributed from the SESAM (Fig. 4.6(c)). For this demonstration, the doping concentration in the cap GaAs layer was originally not designed for high conductivity, and consequently the modulation bandwidth, which is RC-limited, is around 2 kHz due to the large sheet resistance ( $\sim 1 \text{ M}\Omega/\square$ ) of the GaAs layer. It should be straightforward to increase the doping concentration

in our future epitaxy growth such that megahertz bandwidth can be realized for frequency comb stabilization.

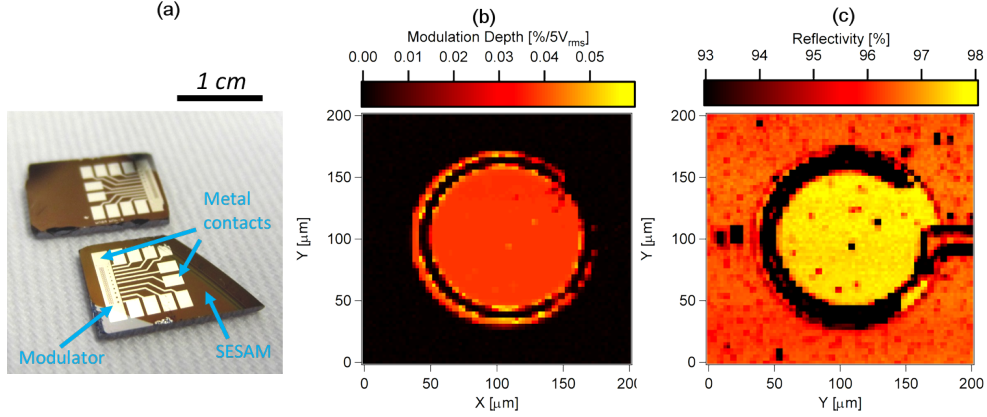


Figure 4.6: (a) Photo of the fabricated graphene modulators on SESAM. (b) A 2-d heat map of the modulation depth for one modulator with 5 Vrms ac signal applied to the device at around 1.4 kHz. The diameter of the modulator is around 120 m. (c) A 2-d heat map of the reflectivity for the same modulator. The active area has a reflectivity of around 98%, of which 1.3% loss is from the absorber and 0.7% loss from the graphene modulator.

## 4.5 Conclusion

In this Chapter, an electro-optic (or in a more precise term: electroabsorption) modulator based on monolayer graphene is shown. Its operation is based on the change of optical conductivity due to changes in the carrier density or equivalently Fermi level or doping level. This effect can be achieved by applying an electric field through an insulator, which acts as a gate dielectric, as what is done similarly in a field-effect transistor. The charge densities in graphene cannot be changed dramatically due to the onset of dielectric breakdown at high field strength; however, since the density of states of graphene at low photon energies are low, its optical absorption is reasonably sensitive to the field-induced charges. Obviously, this effect is more pronounced for long wavelength of light, unless one can dope graphene prior to applying an electric field, such as using chemical means or substrate-induced effects, which might be realized in the near future.

The device is realized with the use of chemical vapor deposition graphene, which provides a

large area for optical applications. The resulting device has an electrical bandwidth over 100 MHz and broad optical bandwidth, although in this experiment only a few wavelengths were tested. The design freedom arising from the choice of dielectric thickness allows one to tailor the insertion loss and modulation depth of the modulator for a particular application.

Due to the limited modulation depth one can obtain in this thin film structure, the device is clearly not suitable for optics communication applications. However, its low loss, low dispersion, and pure amplitude modulation with negligible parasitic phase modulation makes it well suited for modulating the power in a laser cavity, with the device acting as a reflecting mirror. This will be the topic of the next Chapter.

## Chapter 5

### Stabilization of frequency comb with a graphene modulator

Optical frequency combs have become an essential tool in metrology and spectroscopy [14,15]. For applications that require a fully stabilized comb, both the repetition rate ( $f_{\text{rep}}$ ) and the carrier-envelope-offset frequency ( $f_{\text{ceo}}$ ) need to be stabilized [10,11]. The traditional way of stabilizing  $f_{\text{ceo}}$  is feeding back the phase error signal to the pump power of the laser. The achievable bandwidth of this method is, however, limited by the coupling between gain and pulse energy of the laser, which is governed by the stimulated lifetime of the gain medium. Fast corrections to  $f_{\text{ceo}}$  can be done with an extracavity, feed-forward acoustic-optic modulator [98,99]. Sub-MHz loop bandwidth was documented, which was limited by the propagation delay of the acoustic waves in the modulator crystal. Despite the fact that this method could add spatial dispersion and limit the output power, it was proven to be well suited for generating slip-free few-cycle pulses from low-noise Ti:sapphire lasers.

High locking bandwidths of  $f_{\text{ceo}}$  can be reached without resorting to extracavity techniques, as has been pointed out theoretically [26]. Cavity loss modulation, unlike pump power modulation, leads to an immediate change in pulse energy; therefore, its bandwidth is not limited by the stimulated gain lifetime but rather by the cavity roundtrip time, as can be seen from Fig. 2.1. There has been no realization of this loss modulation scheme for stabilizing  $f_{\text{ceo}}$  due to the lack of high-speed electro-optic modulators (EOMs) that are suitable for intracavity, pure loss modulation. Traditional lithium-niobate EOMs act only as a phase modulator in fiber lasers for  $f_{\text{rep}}$  stabilization [100–102]. Intracavity acousto-optic modulator (AOM) may be suitable in some situations; however,

as discussed above, the bandwidth is fairly limited due to the finite propagation speed of acoustic waves.

In this Chapter, we demonstrate the effectiveness of an ultra-thin, graphene-based electro-optic loss modulator [103] that enables record high  $f_{\text{ceo}}$  locking bandwidths ( $>1$  MHz) without adverse effects on the laser performance. We also report an excellent residual in-loop phase noise of 144 mrad (0.3 Hz-3.5 MHz) in a Tm-doped fiber oscillator owing to the large bandwidth of intracavity loss modulation. This new scheme is particularly useful for fiber lasers, which usually exhibit much higher levels of phase noise than solid-state lasers due to their high cavity loss, large intracavity net-dispersion, and large optical nonlinearity.

## 5.1 Theoretical background: Transfer functions

In mode-locked lasers, the high bandwidth of cavity loss modulation can be understood by considering the equations of motion that govern the coupling between gain and pulse energy. The response of a laser to external perturbations can be found by linearizing the equations of motion. With this knowledge, one can analyze how a change in gain and pulse energy lead to a change in  $f_{\text{rep}}$  and  $f_{\text{ceo}}$  [26].

We derive here the transfer functions of pump and loss modulations to a laser's output power and show their difference in bandwidths. The following two coupled equations describe the dynamics of gain and pulse energy, which are linearized about their steady-state values (see Eq. 2.1 and Eq. 2.15):

$$T_R \frac{\partial}{\partial t} \begin{bmatrix} \Delta E_p \\ \Delta g^P \end{bmatrix} = \mathbf{A} \begin{bmatrix} \Delta E_p \\ \Delta g^P \end{bmatrix} + \mathbf{B} \begin{bmatrix} \Delta l^P \\ \Delta P_{\text{pump}} \end{bmatrix} \quad (5.1)$$

Here  $\mathbf{A}$  and  $\mathbf{B}$  are given by

$$\mathbf{A} = \begin{bmatrix} -\frac{\partial q^P}{\partial E_p} E_p & E_p \\ -\frac{g^P}{E_{\text{sat,L}}} & -\frac{T_R}{\tau_L} - \frac{E_p}{E_{\text{sat,L}}} \end{bmatrix}, \mathbf{B} = \begin{bmatrix} -E_p & 0 \\ 0 & \frac{\eta T_R}{E_{\text{sat,L}}} \end{bmatrix} \quad (5.2)$$

where  $T_R$  is the cavity roundtrip time,  $g^P$  and  $l^P$  are the roundtrip power gain and loss (note that  $g^P = 2g$  and  $l^P = 2l$ ),  $q^P = 2q$  is the nonlinear power loss as a function of the pulse energy

( $E_p$ ),  $E_{\text{sat,L}}$  is the gain saturation energy,  $\tau_L$  is the spontaneous gain relaxation time,  $\eta$  is the conversion efficiency from pump power to signal power, and  $P_{\text{pump}}$  is the pump power. Note that  $A_{22} = -T_R/T_G$ , where  $T_G$  is the stimulated gain lifetime. For simplicity, we assume  $\eta$  is independent of  $g^P$ . By Laplace transforms, one readily get the following transfer functions. For pump power modulation:

$$\frac{\Delta E_p(s)}{\Delta P_{\text{pump}}(s)} = \frac{A_{11}B_{22}}{s^2T_R^2 - s\text{Tr}(\mathbf{A})T_R + \det(\mathbf{A})}, \quad (5.3)$$

and for loss modulation:

$$\frac{\Delta E_p(s)}{\Delta l(s)} = \frac{B_{11}(sT_R - A_{22})}{s^2T_R^2 - s\text{Tr}(\mathbf{A})T_R + \det(\mathbf{A})}, \quad (5.4)$$

where  $s$  is the Laplace complex variable.

Both transfer functions have the same poles. For typical high-gain, high-loss fiber lasers in the condition where relaxation oscillation is overdamped by the saturation of self-amplitude modulation, the poles are approximately at frequencies

$$\omega_1 \approx T_G^{-1} \left( \frac{\partial q^P}{\partial E_p} E_p \right)^{-1} \quad (5.5)$$

and

$$\omega_2 \approx T_R^{-1} \left( \frac{\partial q^P}{\partial E_p} E_p \right) \quad (5.6)$$

The bandwidth of pump modulation is limited by the two poles, which arise from the damped relaxation oscillation. Beyond the frequencies of these two poles, the transfer function is similar to a second-order low pass filter. The transfer function of cavity loss modulation has an frequency zero located at  $\omega_0 = T_G^{-1}$ , which pushes the bandwidth to the higher frequency pole  $\omega_2$ . This limit is scalable with the repetition rate. A bulk Ti:sapphire laser with 10 GHz repetition rate, for example, responds to cavity loss modulation up to  $\sim 100$  MHz. Note also that cavity loss modulation behaves like a first-order low pass filter at high frequencies, with its phase lag approaching  $\pi/2$  instead of  $\pi$  as in the case of pump modulation. This is the fundamental advantage of using the cavity loss as a control knob.

Despite the high bandwidth and low phase delay provided by the method of cavity loss modulation, it cannot be achieved with electro-optic crystals due to their strong coupling to  $f_{\text{rep}}$ . We





minimally ( $<1\%$ ).

### 5.3 Experimental results: phase locking of carrier-envelope-offset frequency

The frequency responses of output power to pump and loss modulations were measured with an HP89441A vector signal analyzer, shown in Fig. 5.2. Pump power modulation had a 3 dB corner at 89 kHz, whereas the loss modulation from the graphene modulator had a higher corner at 600 kHz and slower roll-off. By fitting Eq. (5.3) and (5.4) to the data, the laser parameters were found (see Fig. 5.2 caption) and are close to the experimental values. Note that the absolute phase variation in loss modulation scheme ( $\pm 90$  degrees) can be fully compensated by lag/lead circuits, whereas in pump modulation scheme (0 to -180 degrees), the phase cannot be fully compensated.

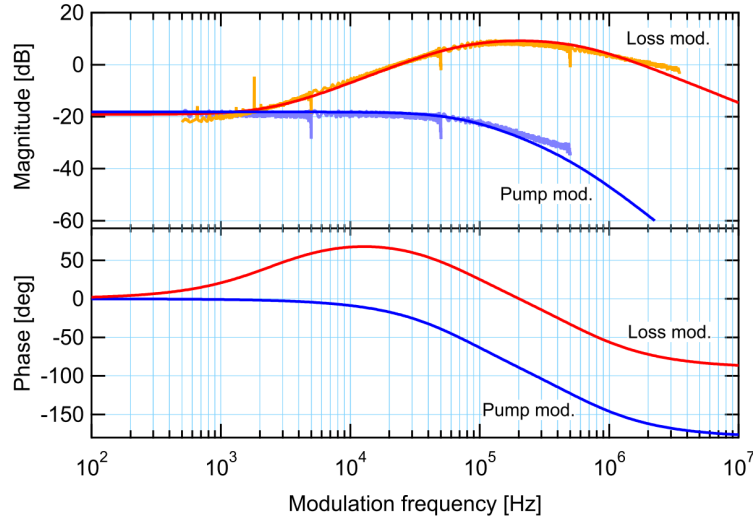


Figure 5.2: (Top) The frequency responses of output power to pump power and loss modulation. Thin lines are measured traces and thick lines are fitted transfer functions calculated from Eq. (3) and (4). The following laser parameters are used in fitting the Tm:fiber data:  $E_p=1.1\text{ nJ}$ ;  $T_R=10\text{ ns}$ ;  $P_{\text{pump}}=1\text{ W}$ ;  $\eta=15\%$ ;  $E_{\text{sat,L}}=8.5\mu\text{ J}$ ;  $\tau_L=535\mu\text{ s}$ ;  $E_p(\frac{\partial q}{\partial E_p})=0.04$ . (Bottom) Calculated phase response of the same fitted model shown in the top figure. Negative values represent phase lag. Loss modulation has a gain of -1 at low frequencies.

We detected  $f_{\text{ceo}}$  by an in-line f-2f interferometer at  $\sim 1100$  nm after amplifying the power from the oscillator to  $\sim 200$  mW. Phase error detection was performed using an analog phase detector (Minicircuits ZRPD-1), followed by a 10 MHz low-pass filter. We phase-locked the  $f_{\text{ceo}}$  beat to a

stable RF synthesizer with a low time-delay loop filter. The stabilization was performed both with and without a division-by-4 pre-scaler.

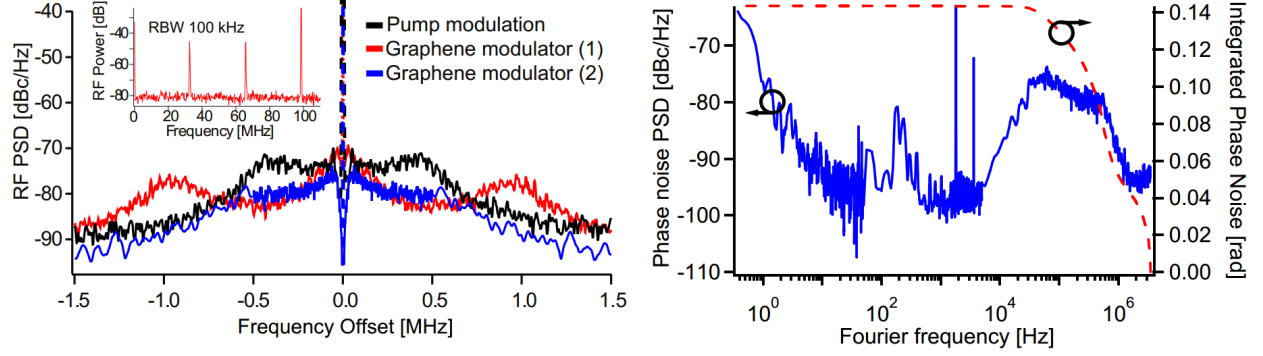


Figure 5.3: (Top) In-loop RF spectra of phase-locked  $f_{ceo}$  beats recorded when locked with pump current modulation and with the graphene modulator. Inset: free-running  $f_{ceo}$  and repetition rate at 100 MHz. (Bottom) Residual phase noise spectral density (Graphene modulator (2)). The integrated phase noise is 144 mrad over the full span.

The results of the  $f_{ceo}$  stabilization are shown in Fig. 5.3. The free-running linewidth of the  $f_{ceo}$  beat was estimated to be around 50 kHz (Fig. 5.3, inset). With the traditional pump power modulation alone, we achieved stable phase-locking of the  $f_{ceo}$ . After optimization of the feedback-loop we were able to concentrate 95.1% of the RF power in the coherent carrier, corresponding to 224 mrad integrated phase noise. The RF power in the carrier and the phase noise is related by [105]

$$\text{Fractional power in the carrier} = e^{-\Delta\phi_{rms}^2}. \quad (5.7)$$

in the case of small phase modulation.

Due to the aforementioned limitation in the pump-modulation scheme, even with a good loop-filter design the servo bump could not be pushed much beyond 400 kHz. By feeding back to the graphene modulator, we achieved much larger modulation bandwidths. Initially, we observed a servo bump at  $\sim 1$  MHz (curve “Graphene modulator (1)”), with optimized loop filter settings, we found  $\sim 98\%$  of the RF power in the coherent carrier and the complete absence of any servo bumps (curve “Graphene modulator(2)”). In this optimized setting, we measured a record low integrated residual phase noise of 144 mrad (0.3 Hz-3.5 MHz). Note that this value represents

the in-loop performance and may underestimate the actual out-of-loop phase noise. We found the laser-dynamics-limited crosstalk ( $\Delta f_{\text{rep}}/\Delta f_{\text{ceo}}$ ) to be  $< 7 \times 10^{-7}$ , which was smaller than that of pump power modulation and allowed for tighter simultaneous locking of  $f_{\text{rep}}$  and  $f_{\text{ceo}}$ . Due to the limited DC response ( $< 1$  Hz) of the current modulator, we still required a slow feedback to the pump power of the laser for long-term operation. Alternatively, the long-term stability could be guaranteed by a thermal feedback to an intra-cavity fiber grating [106]. Currently the performance is limited by the locking electronics and the intracavity frequency response of the modulator. With an improved design of the laser parameters, even better phase noise performance may be achieved. Working towards a compact frequency comb, we have also applied the graphene modulator for high bandwidth stabilization of a 500 MHz Tm: fiber laser, reaching an integrated phase noise of  $\sim 400$  mrad in the carrier-envelope-offset frequency [107]. An all polarization-maintaining Er: fiber frequency comb was also demonstrated recently using the graphene modulator [108].

## 5.4 Conclusion

To the best of our knowledge, this work presents the first successful  $f_{\text{ceo}}$  stabilization of an optical frequency comb by means of a pure intra-cavity loss modulator. The phase noise of the stabilized  $f_{\text{ceo}}$  beat frequency was 144 mrad, a record low value for a fiber-laser frequency comb. This was enabled by a novel low-insertion loss graphene electro-optic modulator, allowing feedback bandwidths far beyond the current limit imposed by the stimulated gain-lifetime. Due to their low insertion loss and their ultra-compact design, these modulators could empower a new breed of monolithic, phase-locked combs with GHz fundamental pulse repetition rates. We also envision the use of the hybrid SESAM/Graphene device, shown in Section 4.4, in a portable frequency comb where polarization-maintaining, self-starting, and long-term-stable operation is required [94].

## Chapter 6

### Laser dynamics: backaction of continuum on soliton and its implications on the transfer function of a modelocked laser

#### 6.1 Motivation

Mode-locked lasers combined with phase-locking techniques have revolutionized optical clocks and precision measurements [13, 109–111]. The basic but powerful technique that has driven these advances in fundamental science is indeed active feedback control, which rids a laser’s output of phase or timing fluctuations. Ideally the ultimate noise level is determined by the coherence of external references, such as a narrow-linewidth laser or a low-noise microwave oscillator. In practice, the effectiveness of this active stabilization relies strongly on the available in-loop gain and bandwidth, both of which not only depend on the properties of the actuator (such as controlling the pump power or cavity length) but also on the complex dynamics of pulse evolution, gain-photon coupling, and cross-talk between actuators. The latter often sets the upper bound of the bandwidth, even though the former may still function beyond that limit. A complete understanding of laser dynamics is therefore indispensable if one wants to tackle the noise, either technical (pump power, acoustic, and vibrational noises) or quantum mechanical (amplified spontaneous emission or ASE), which nearly always have contributions beyond the limit of servo bandwidth set by laser dynamics. It is worth noting that although mode-locked lasers serve as an extremely quiet optical flywheel at short time scales [112], there exists a frequency region ( $\sim 100\text{kHz}$ – $10\text{MHz}$ ) where technical or ASE-driven noise is present but feedback performance can be limited by either the laser dynamics or the actuators.

We study here an intrinsic resonance at radio frequencies(RF) in a mode-locked laser's transfer function, which lies in the aforementioned frequency range of interest and may be of concern if quantum-limited noise is desired from DC to the Nyquist frequency. This phenomenon exists in lasers where solitary pulse formation [30, 113–115] plays a non-negligible, if not dominant, role in the pulse-shaping process. We focus our discussion on cases where solitary pulse formation is stronger than self-amplitude modulation, but in cases where the latter dominates such as in a Kerr-lens mode-locked Ti:sapphire laser, this RF resonance also exists due to the presence of self-phase modulation(SPM) and anomalous group velocity dispersion(GVD). It should be noted that soliton mode-locking is nowadays the most adopted method to build compact frequency combs owing to its two main advantages: allowing a simple and compact cavity and able to generate sub-picosecond pulses with near-zero chirp [116–119].

## 6.2 Theoretical background

The generation and propagation of soliton and the dispersive waves (or continuum) can be described by the soliton perturbation theory based on the Haus master equation [120]. In Haus's and many of the followers' work, the generation and back-action of the continuum is assumed negligible. However, under certain circumstances, the existence of continuum cannot be neglected and is indeed crucial for understanding laser dynamics. A well-known example is the Kelly sidebands, which appear in the optical spectrum of a laser [121]. While Kelly sidebands occur when the pulse acquires a large amount of nonlinear phase per roundtrip, the RF resonance we describe here requires little such phase. For best noise performance, this is an important regime to study because of the reduced nonlinear coupling from amplitude to phase noise.

To the best of our knowledge, this RF resonance was first discussed by Katz et al. [122], who found an energy oscillation by numerically simulating the pulse propagation in the context of statistical light mode theory. The characteristic frequency was found to be determined by the evolving phase difference between the soliton and the continuum. Experimentally it was first observed by Hartl et al. [123] in a soliton fiber laser, and its characteristic frequency was confirmed.

However, it has not been discussed so far what effects in the Haus master equation cause this oscillation. The fact that the electric fields of the soliton and the continuum are evolving and interacting does not imply energy variations, and indeed we find that it is critical to have reverse saturable absorption such as gain filtering(GF) or two-photon absorption(TPA), which provide intensity-dependent energy dissipation. These two effects are ubiquitous in mode-locked lasers, thus this continuum-induced oscillation is unavoidable. Moreover, an oscillation in the pulse energy implies that there exists an energy exchange between the pulse and the gain medium, similar to a laser's relaxation oscillation. Therefore, full consideration of the gain dynamics is required for a better agreement between theory and experiment than if one assumes that energy flows only between the soliton and the continuum, as adopted in [122]. In the following discussion, we derive analytically the effect of this resonance on the laser's transfer function, based on a model extended from soliton perturbation theory. Then we compare the analytic results to numerical simulations and experiments.

### 6.3 Analytic approach

For most mode-locked lasers, the pulse shaping mechanism can be described by the master equation developed by Haus, if the pulse change per roundtrip is small. That is,

$$T_R \frac{\partial A}{\partial T} = \left[ -iD \frac{\partial^2 A}{\partial t^2} + i\delta |A|^2 A \right] + \mathbf{R}A, \quad (6.1)$$

where  $A = A(T, t)$  is the slowly-varying field envelope, with  $T$  and  $t$  being the time variables at a time scale of the roundtrip time ( $T_R$ ) and pulse duration respectively. The terms in the bracket are GVD and SPM that lead to the formation of solitary pulses, where  $D$  is the total group delay dispersion per roundtrip and  $\delta$  is the SPM coefficient.  $\mathbf{R}$  represents perturbations that shed energy into the continuum. With  $\mathbf{R} = 0$ , the equation becomes the nonlinear Schrödinger's equation(NLSE), and its simplest closed-form solution is

$$A_s(T, t) = A_0 \operatorname{sech}(t/\tau) e^{i\Phi \frac{T}{T_R}}, \quad (6.2)$$

where  $A_0$  is the amplitude,  $\tau$  is the soliton pulse width. After every roundtrip, the soliton acquires a phase shift  $\Phi$ , given by  $|D|/\tau^2$ . To consider perturbations, we express the the field as

$$A(T, t) = [A_0 \operatorname{sech}(t/\tau) + a_c] e^{i\Phi \frac{T}{T_R}}, \quad (6.3)$$

where  $a_c$  is the continuum field. Assuming  $a_c$  is small, Eq. 6.1 can then be linearized by plugging in Eq. 6.3.

Following the definitions and notations used in the soliton perturbation theory in [?], the continuum field  $|a_c\rangle$  can be written as

$$|a_c\rangle = \int_{-\infty}^{\infty} dk [g_c(k) |f_k\rangle + \bar{g}_c(k) |\bar{f}_k\rangle], \quad (6.4)$$

where  $k = \omega\tau$ , and  $\omega$  is the offset from soliton's center frequency.  $|f_k\rangle$  and  $|\bar{f}_k\rangle$  are the solutions to the linearized NLSE. To first order in  $a_c$ , the spectral components  $g_c(k)$  are dictated by the following equation of motion:

$$T_R \frac{\partial g_c(k)}{\partial T} = \gamma(k) \cdot g_c(k) + \langle f_k^{(+)} | \mathbf{R} A_0 \operatorname{sech}(t/\tau) \rangle, \quad (6.5)$$

where  $\gamma(k)$  determines how the continuum propagates over time and is given by  $[-i\Phi(1 + k^2) - l_c(k)]$ . Here  $l_c(k)$  is the net amplitude loss per roundtrip of the continuum. The second term on the right side denotes the excitation of continuum by  $\mathbf{R}$ . We are utilizing the orthogonality between the solutions to NLSE and its adjoint counterpart  $f_k^{(+)}$  to project out the amplitudes [31, 120, 124]. The inner product  $\langle u(t) | v(t) \rangle$  is defined as  $\frac{1}{2\tau} \int_{-\infty}^{\infty} u(t) v(t) dt$ .

Given the perturbation  $\mathbf{R}$ , we can find the corresponding spectral components  $g_c(k)$ . Here we consider periodic perturbations from lumped cavity elements, which include linear gain/loss, gain filtering, and a saturable absorber containing a TPA layer. That is,

$$\mathbf{R} = \left[ g - l + \frac{g}{\Omega_g^2} \frac{\partial^2}{\partial t^2} - q - \Gamma_{\text{TPA}} |A|^2 \right] \sum_{m=-\infty}^{\infty} \delta(T - mT_R), \quad (6.6)$$

where  $g$ ,  $l$ , and  $q$  are the amplitude gain, loss, and saturable loss per roundtrip,  $\Omega_g$  is the half-width half-maximum of the gain bandwidth, and  $\Gamma_{\text{TPA}}$  is the TPA coefficient that has taken the absorption coefficient, effective layer thickness, and mode area into account.



By integrating Eq. 6.5, we obtain

$$g_c(k) = \frac{1}{T_R} \left[ \frac{A_0 g}{6\Omega_g^2 \tau^2} + \frac{A_0^3 \Gamma_{\text{TPA}}}{12} \right] \text{sech} \left( \frac{k\pi}{2} \right) \frac{e^{\gamma(k) \frac{T}{T_R}}}{1 - e^{\gamma(k)}}, \quad (6.7)$$

which is periodic in time  $T$  and is defined here for  $0 \leq T < T_R$ . The total field, shown in Eq. 6.3, oscillates and its amplitude and phase evolution is completely determined by  $\gamma(k)$ . The amplitude decay is dictated by  $l_c(k)$ , which results mainly from the loss of the absorber, and the phase evolution is dictated by the nonlinear phase shift  $\Phi$ . This oscillation is intrinsic in a soliton mode-locked laser with periodic perturbation from lumped optical elements. So far no external perturbation such as pump power change has been introduced into the system. Note also that we ignore the effect of the saturable loss because the absorber is typically used at a highly saturated regime, therefore contributing negligible amount to the continuum. Eq. 6.7 summarizes how the generated continuum depends on the strength of GF and TPA.

Since we are concerned with the changes in intracavity power, we use the projection trick again to find  $\langle f_w^{(+)} | \mathbf{R} f_k \rangle$ , which is the action of the generated continuum onto the pulse energy. Here  $f_w^{(+)}$  is the adjoint of the derivative of  $A_s$  with respect to pulse energy, which is defined by  $W_s = \int_{-T_R/2}^{T_R/2} |A_s(T, t)|^2 dt$ . The linear gain and loss terms in  $\mathbf{R}$  cause no changes in  $W_s$  because  $|f_w^{(+)}\rangle$  and  $|f_k\rangle$  are mutually orthogonal. Therefore, the only terms that can lead to any back-action on the soliton are GF and TPA. For GF only,

$$\langle f_w^{(+)} | \mathbf{R} f_k \rangle = \left[ -\frac{g(1+k^2)^2 \pi}{2\Omega_g^2 \tau} \right] A_0 \text{sech} \left( \frac{k\pi}{2} \right), \quad (6.8)$$

and for TPA only,

$$\langle f_w^{(+)} | \mathbf{R} f_k \rangle = \left[ -\frac{\Gamma_{\text{TPA}}(1+k^2)^2 \tau \pi}{4} \right] A_0^3 \text{sech} \left( \frac{k\pi}{2} \right). \quad (6.9)$$

Combining Eq. 6.7, 6.8, and 6.9, we can obtain the total effect of the steady-state continuum on the soliton pulse energy, which is

$$\langle f_w^{(+)} | \mathbf{R} a_c \rangle = \int_{-\infty}^{\infty} dk \langle f_w^{(+)} | \mathbf{R} f_k \rangle \cdot 2\text{Re}[g(k)]. \quad (6.10)$$

This adds an RF oscillatory term that is characteristic of the propagation constant  $\gamma(k)$  of the continuum. Since the integrand of Eq. 6.10 is peaked at  $k = 0$ , the RF power oscillation peak

frequency is given by the imaginary part of  $\gamma(0)$ :

$$f_{\text{res}} = \frac{1}{T_R} \frac{\Phi}{2\pi} = \frac{|D|}{2\pi T_R \tau^2}, \quad (6.11)$$

which is the beat frequency between soliton and continuum due to their different phase accumulation rate. The off-center spectral components of continuum oscillate at higher frequencies than Eq. 6.11, forming a single-sided tail of the RF resonance (Fig. 6.1). It should be noted that Eq. 6.10 contains all the spectral information (k-axis) and thus allows one to derive the lineshape of the RF resonance, not only the resonant frequency as shown previously in [122, 123].

To perform the lineshape calculation, we consider this oscillatory term in the picture of energy-gain coupling and transfer properties from pump to the output power. That is, we consider the equation of motion for the total energy with this added back-action. Note that the total intracavity energy, denoted here by  $W$ , equals  $\left[W_s + \int_{-T_R/2}^{T_R/2} |a_c|^2 dt\right]$  because the cross interference term vanishes due to the orthogonality between soliton and continuum.

$$T_R \frac{\partial W}{\partial T} = \langle f_w^{(+)} | \mathbf{R} A_0 \text{sech}(t/\tau) \rangle + \langle f_w^{(+)} | \mathbf{R} a_c \rangle, \quad (6.12)$$

where  $\langle f_w^{(+)} | \mathbf{R} A_0 \text{sech}(t/\tau) \rangle$  can be calculated to be  $(2g - 2l - \frac{2g}{3\Omega_g^2 \tau^2} - 2q - \frac{4}{3} A^2 \Gamma_{\text{TPA}})W$ . Also, the equation of motion for the gain is

$$T_R \frac{\partial g}{\partial T} = (-\alpha - g) \frac{T_R}{\tau_L} - g \frac{W}{E_{\text{sat,L}}} + \frac{\eta P_{\text{pump}} T_R}{E_{\text{sat,L}}}, \quad (6.13)$$

where  $\alpha$  is the loss without pump (non-zero for three-level systems),  $\tau_L$  is the upper state lifetime,  $E_{\text{sat,L}}$  is the saturation energy of the gain medium,  $\eta$  is the pump-to-signal light conversion efficiency, and  $P_{\text{pump}}$  is the pump power. We now linearize Eq. 6.12 and 6.13 around their steady state values, allowing only small perturbations in  $P_{\text{pump}}$ . The response of the laser is then found by Laplace transforming the linearized coupled equations. We obtain

$$\frac{\Delta W(s)}{\Delta P_{\text{pump}}(s)} = \left[ (s T_R)^2 - (s T_R) \mathbf{Tr}(\mathbf{A}) + \mathbf{det}(\mathbf{A}) \right]^{-1}, \quad (6.14)$$

where  $s$  is the Laplace frequency and  $\mathbf{A}$  is a 2x2 matrix with elements being

$$\begin{aligned}
A_{11} &= -\frac{\partial q}{\partial W}W - \frac{4g}{3\Omega_g^2\tau^2} - \frac{2}{3}\frac{W}{\tau}\Gamma_{\text{TPA}} - \mathcal{L}\{\langle f_w^{(+)}|\mathbf{R}_{ac}\rangle\}/W, \\
A_{12} &= W, \\
A_{21} &= -g/E_{\text{sat,L}}, \\
A_{22} &= -T_{\text{R}}/\tau_{\text{L}} - W/E_{\text{sat,L}},
\end{aligned} \tag{6.15}$$

where  $\mathcal{L}$  denotes Laplace transform. Eq. 6.14 summarizes the effect of the continuum's back-action by its manifestation as a resonance peak in the transfer function. It should be emphasized that this power oscillation can be excited not only by an external force, such as pump power modulation as shown here, but also by the laser's internal noise, such as ASE. Latter case is similar to the discussion in [122]. Our idealized, noiseless model ignores ASE, and therefore, at this non-physically quiet steady state, the RF oscillation would not be observable in the power spectrum, since the continuum generation is assumed small and cannot compete with the strong damping from the laser gain. However, the transfer functions obtained in this noiseless approach are useful for predicting the physically correct noise behavior of the laser's output when combined with the noise spectral distribution at the input (for example the pump's relative intensity noise).

## 6.4 Numerical simulation

To examine the applicability of the analytic theory, we performed both numerical simulations and experiments. We used a split-step Fourier transform method to simulate the evolution of solitons based on Haus master equation (Eq. 6.1). The transfer function, as derived in Eq. 6.14, was obtained by recording the pulse energy over time after perturbing the pump power with a one-pixel impulse function. The transient response in pulse energy was then Fourier transformed to obtain both the amplitude and phase response. We compare, for clarity here, the analytic theory and the numerical simulation in the cases where either GF or TPA is dominant in stabilizing the laser against Q-switching.

In Fig. 6.1, the transfer functions obtained from the analytic theory and numerical simulations

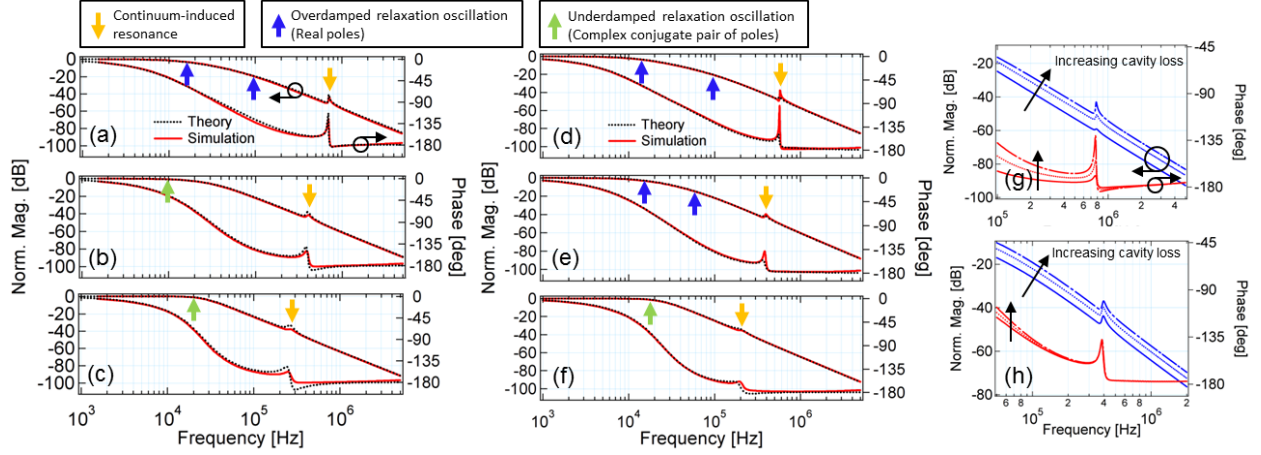


Figure 6.1: Transfer functions of pump power modulation to output power in the case of (a)-(c) GF and (d)-(f) TPA. Figure (g) and (h) show the distinct behavior of the continuum-induced peak in the case of GF and TPA respectively. Parameters of the laser are the following:  $|D| = 200 \text{ fs}^2$ ,  $\delta = 1.7 \times 10^{-7} \text{ rad/Watt}$ ,  $\Omega_g/2\pi = 3.5 \text{ THz}$  in (a)-(c) and  $70.7 \text{ THz}$  in (d)-(f),  $\Gamma_{\text{TPA}} = 0 \text{ Watt}^{-1}$  in (a)-(c) and  $1.3 \times 10^{-8} \text{ Watt}^{-1}$  in (d)-(f),  $T_R = 10 \text{ ns}$ ,  $\tau_L = 8 \text{ ms}$ ,  $E_{\text{sat,L}} = 382 \mu\text{J}$ ,  $l = 1 \%$ ,  $q_0 = 0.25 \%$ , and  $I_{\text{sat}} = 100 \text{ MW/cm}^2$ . The pump power is decreased from (a) to (c) and from (d) to (f), and the corresponding soliton parameters ( $W, \Phi$ ) are (a)  $72 \text{ nJ}$ ,  $43.7 \text{ mrad}$ ; (b)  $53 \text{ nJ}$ ,  $24.5 \text{ mrad}$ ; (c)  $43 \text{ nJ}$ ,  $16.0 \text{ mrad}$ ; (d)  $63 \text{ nJ}$ ,  $35.0 \text{ mrad}$ ; (e)  $52 \text{ nJ}$ ,  $23.6 \text{ mrad}$ ; (f)  $37 \text{ nJ}$ ,  $12.0 \text{ mrad}$ . Figure (g) and (h) use the same parameters as (a) and (d) respectively, except cavity loss  $l$  is varied from  $0.5 \%$  to  $1.5 \%$ , while  $W$  and  $\Phi$  are maintained by changing  $P_{\text{pump}}$ .

are shown. The parameters used in the theory and simulation are all the same, and there are no fitting parameters. It can be seen that the resonance frequency predicted by Eq. 6.11 indeed agrees well with the simulation. Moreover, as the pump power is reduced from (a) to (c) in both GF and TPA, the magnitude of this resonance decreases because of the longer pulse duration and therefore less affected by GF or TPA. For the same reason, the relaxation oscillation peak has a reverse trend. It is also evident that the applicability of the soliton perturbation theory decreases as the nonlinear phase shift per roundtrip decreases with the pump power. In the weak soliton pulse shaping regime, one should instead treat SPM and GVD as perturbations to an absorber-shaped solution.

Fig 6.1(g) and (h) shows the change in the continuum-induced peak with the cavity loss, or equivalently the saturated gain in the case of GF and TPA, respectively. While GF sheds more energy into continuum and allows stronger back-action to the pulse energy as the cavity loss

increases, TPA is totally independent of this, as can also be seen from Eq. 7, 8, and 9.

Even though the magnitude of the continuum-induced peak is rather insignificant, the phase response has a large jump that could pose a restriction on one's ability to feedback control the laser's output. For good noise performance, one desires the highest power and shortest pulse duration possible, which are cases shown in Fig. 6.1(a) and (d). In this regime, however, the continuum-induced peak is rather large.

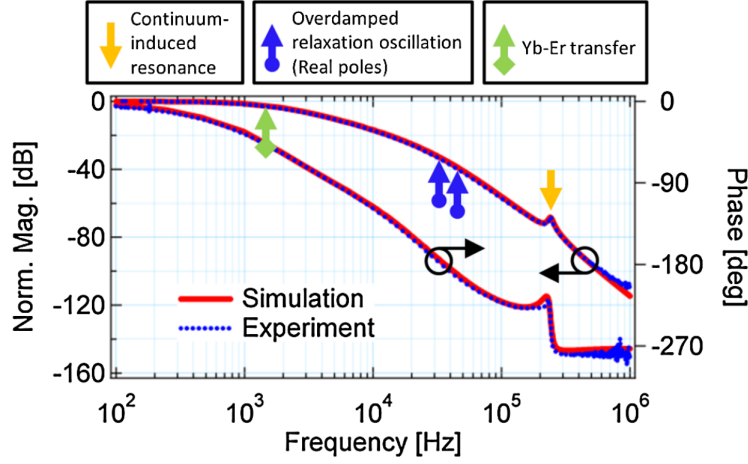


Figure 6.2: Experimental and simulated transfer functions of pump power modulation to output power. Laser parameters used in the simulation are the following:  $|D| = 79 \text{ fs}^2$ ,  $\text{TOD} = 2052 \text{ fs}^3$ ,  $\delta = 3.2 \times 10^{-7} \text{ rad/Watt}$ ,  $\Omega_g/2\pi = 4.3 \text{ THz}$  (Lorentzian),  $\Gamma_{\text{TPA}} = 2.7 \times 10^{-8} \text{ Watt}^{-1}$ ,  $T_R = 4 \text{ ns}$ ,  $\tau_L = 7.8 \text{ ms}$ ,  $E_{\text{sat,L}} = 584 \mu\text{J}$ ,  $l = 0.96 \%$ ,  $q_0 = 0.20 \%$ ,  $I_{\text{sat}} = 400 \text{ MW/cm}^2$ ,  $W = 8.8 \text{ nJ}$ , and  $\Phi = 6.4 \text{ mrad}$ . A pole at around 1 kHz is present due to Föster transfer from ytterbium to erbium [125].

## 6.5 Experimental results

The same physics was experimentally observed in a free-space Er:Yb:glass laser with a center wavelength of 1560 nm. The laser was built with a X-folded linear cavity configuration with the gain medium placed at its Brewster angle and pumped by a single-mode laser diode at 980 nm wavelength. The mode-locking was started and stabilized by a semiconductor saturable absorber. The intracavity dispersion was around  $-80 \text{ fs}^2$ , mainly from the gain medium, which allowed soliton mode-locking. When mode-locked, the laser emitted 200fs (FWHM) pulses at a repetition rate of

250 MHz. The nonlinear phase  $\Phi$  gained by the solitary pulse was around 10 mrad. The pump transfer function was measured with a network analyzer, and calibration against the pump diode response was performed. As shown in Fig. 6.2, excellent agreement was found between the experiment and numerical simulation. The parameters used for the simulation were obtained from direct measurements ( $W$ ,  $\tau$ ,  $T_R$ ,  $l$ ,  $q$ , center wavelength, and mirror dispersion), from references (Er:Yb:glass), and from a best effort of estimation ( $\Omega_g$ , beam cross section, gain medium dispersion). The best-effort estimates were then adjusted within their known bounds to approximate the measured quantities. We found that transfer functions with the continuum-induced peak set stringent restrictions on the fitting parameters, which may be useful for estimating intracavity dispersion up to the third order. Due to the appreciable amount of third-order dispersion, we could not directly apply the analytic results. Numerical approach is more appropriate and less obscure in this case, as has been discussed in [126].

## 6.6 Conclusion

In conclusion, an intrinsic power oscillation emerges in soliton mode-locked lasers. The oscillation occurs as a result of (1) the field oscillation caused by the back-action of the continuum on the soliton and (2) dissipative effects such as GF and TPA. The oscillation frequency is determined by the evolving phase difference between the soliton and the continuum. We have presented an analytic theory based on an extended soliton perturbation theory that fully accounts for this phenomenon; meanwhile, excellent agreement was found between our analytic/numerical models and experiment. The physics presented here applies to most femtosecond sources, although the resonance's contribution to the total noise may be small due to the strong damping from the gain medium. It is nevertheless crucial to keep the back-action of continuum in check especially when technical noise suppression over the full RF spectrum is desired. We believe that with the improved understanding of laser dynamics we presented here will not only advance the research of light sources with record-low noise performance, such as required for low-noise microwave generation, but also help the realization of robust, field-able frequency combs in the near future.

## Bibliography

- [1] A. H. Zewail, “Femtochemistry: Atomic-scale dynamics of the chemical bond using ultrafast lasers (nobel lecture),” *Angewandte Chemie International Edition* **39**, 2586–2631 (2000).
- [2] T. Udem, J. Reichert, R. Holzwarth, and T. W. Hänsch, “Absolute optical frequency measurement of the cesium  $d_1$  line with a mode-locked laser,” *Phys. Rev. Lett.* **82**, 3568–3571 (1999).
- [3] P. M. Paul, E. S. Toma, P. Breger, G. Mullot, F. Aug, P. Balcou, H. G. Muller, and P. Agostini, “Observation of a train of attosecond pulses from high harmonic generation,” *Science* **292**, 1689–1692 (2001).
- [4] W. Denk, J. Strickler, and W. Webb, “Two-photon laser scanning fluorescence microscopy,” *Science* **248**, 73–76 (1990).
- [5] R. R. Gattass and E. Mazur, “Femtosecond laser micromachining in transparent materials,” *Nature Photonics* **2**, 219–225 (2008).
- [6] M. D. Perry, B. C. Stuart, P. S. Banks, M. D. Feit, V. Yanovsky, and A. M. Rubenchik, “Ultrashort-pulse laser machining of dielectric materials,” *Journal of Applied Physics* **85** (1999).
- [7] K. M. Davis, K. Miura, N. Sugimoto, and K. Hirao, “Writing waveguides in glass with a femtosecond laser,” *Opt. Lett.* **21**, 1729–1731 (1996).
- [8] H. Haus and A. Mecozzi, “Noise of mode-locked lasers,” *IEEE Journal of Quantum Electronics* **2** (1993).
- [9] H. Haus, “Mode-locking of lasers,” *IEEE Journal of Selected Topics in Quantum Electronics* **6**, 1173–1185 (2000).
- [10] S. A. Diddams, D. J. Jones, J. Ye, S. T. Cundiff, J. L. Hall, J. K. Ranka, R. S. Windeler, R. Holzwarth, T. Udem, and T. W. Hänsch, “Direct link between microwave and optical frequencies with a 300 THz femtosecond laser comb,” *Phys. Rev. Lett.* **84**, 5102–5105 (2000).
- [11] D. J. Jones, S. A. Diddams, J. K. Ranka, A. Stentz, R. S. Windeler, J. L. Hall, and S. T. Cundiff, “Carrier-envelope phase control of femtosecond mode-locked lasers and direct optical frequency synthesis,” *Science* **288**, 635–639 (2000).
- [12] T. Udem, R. Holzwarth, and T. W. Hänsch, “Optical frequency metrology,” *Nature* **416**, 233–237 (2002).

- [13] S. T. Cundiff and J. Ye, “*Colloquium* : Femtosecond optical frequency combs,” *Rev. Mod. Phys.* **75**, 325–342 (2003).
- [14] S. A. Diddams, “The evolving optical frequency comb,” *J. Opt. Soc. Am. B* **27**, B51–B62 (2010).
- [15] N. R. Newbury, “Searching for applications with a fine-tooth comb,” *Nature Photonics* **5**, 186–188 (2011).
- [16] T. M. Fortier, M. S. Kirchner, F. Quinlan, J. Taylor, J. C. Bergquist, T. Rosenband, N. Lemke, A. Ludlow, Y. Jiang, C. W. Oates, and S. A. Diddams, “Generation of ultrastable microwaves via optical frequency division,” *Nature Photonics* **5**, 425–429 (2011).
- [17] C. Benko, T. K. Allison, A. Cingöz, L. Hua, F. Labaye, D. C. Yost, and J. Ye, “Extreme ultraviolet radiation with coherence time greater than 1 s,” *Nature Photonics* **8**, 530–536 (2014).
- [18] C. Salomon, D. Hils, and J. L. Hall, “Laser stabilization at the millihertz level,” *J. Opt. Soc. Am. B* **5**, 1576–1587 (1988).
- [19] J. L. Hall, M. S. Taubman, and J. Ye, “Laser stabilization,” in “*Handbook of Optics*,” (Optical Society of America, 2000), chap. 27.
- [20] R. Paschotta, “Noise of mode-locked lasers (Part II): timing jitter and other fluctuations,” *Applied Physics B-Lasers and Optics* **79**, 163–173 (2004).
- [21] N. R. Newbury and W. C. Swann, “Low-noise fiber-laser frequency combs (Invited),” *Journal of the Optical Society of America B* **24**, 1756 (2007).
- [22] T. R. Schibli, E. R. Thoen, F. X. Kärtner, and E. P. Ippen, “Suppression of Q-switched mode locking and break-up into multiple pulses by inverse saturable absorption,” *Electrical Engineering* **49**, 41–49 (2000).
- [23] T. R. Schibli, U. Morgner, and F. X. Kärtner, “Control of q-switched mode locking by active feedback,” *Opt. Lett.* **26**, 148–150 (2001).
- [24] R. Paschotta, “Noise of mode-locked lasers (part i): numerical model,” *Applied Physics B* **79**, 153–162 (2004).
- [25] R. Paschotta, “Noise of mode-locked lasers (part ii): timing jitter and other fluctuations,” *Applied Physics B* **79**, 163–173 (2004).
- [26] “Theory of the frequency comb output from a femtosecond fiber laser,” *IEEE Journal of Quantum Electronics* **41**, 1388–1402 (2005).
- [27] F. Kärtner, J. der Au, and U. Keller, “Mode-locking with slow and fast saturable absorbers—what’s the difference?” *IEEE Journal of Selected Topics in Quantum Electronics* **4**, 159–168 (1998).
- [28] H. Haus, “Theory of mode locking with a fast saturable absorber,” *Journal of Applied Physics* **07733**, 3049–3058 (1975).



- [29] H. A. Haus, J. G. Fujimoto, and E. P. Ippen, "Structures for additive pulse mode locking," [8, 2068](#) (1991).
- [30] F. Kärtner, I. Jung, and U. Keller, "Soliton mode-locking with saturable absorbers," *IEEE Journal of Selected Topics in Quantum Electronics* [2, 540-556](#) (1996).
- [31] F. X. Kärtner, D. Kopf, and U. Keller, "Solitary-pulse stabilization and shortening in actively mode-locked lasers," *J. Opt. Soc. Am. B* [12, 486-496](#) (1995).
- [32] A. Bartels, D. Heinecke, and S. A. Diddams, "Passively mode-locked 10 GHz femtosecond ti:sapphire laser," *Opt. Lett.* [33, 1905-1907](#) (2008).
- [33] M. Endo, A. Ozawa, and Y. Kobayashi, "Kerr-lens mode-locked Yb:KYW laser at 4.6 GHz repetition rate," *Opt. Express* [20, 12191-12197](#) (2012).
- [34] V. Matsas, T. Newson, D. Richardson, and D. Payne, "Self-starting passively mode-locked fibre ring soliton laser exploiting nonlinear polarisation rotation," *Electronics Letters* [28, 1391-1393](#) (1992).
- [35] M. E. Fermann, M. L. Stock, M. J. Andrejco, and Y. Silberberg, "Passive mode locking by using nonlinear polarization evolution in a polarization-maintaining erbium-doped fiber," *Opt. Lett.* [18, 894-896](#) (1993).
- [36] N. J. Doran and D. Wood, "Nonlinear-optical loop mirror," *Opt. Lett.* [13, 56-58](#) (1988).
- [37] M. E. Fermann, F. Haberl, M. Hofer, and H. Hochreiter, "Nonlinear amplifying loop mirror," *Opt. Lett.* [15, 752-754](#) (1990).
- [38] U. Keller, K. Weingarten, F. Kartner, D. Kopf, B. Braun, I. Jung, R. Fluck, C. Honninger, N. Matuschek, and J. Aus der Au, "Semiconductor saturable absorber mirrors (sesams) for femtosecond to nanosecond pulse generation in solid-state lasers," *Selected Topics in Quantum Electronics, IEEE Journal of* [2, 435 -453](#) (1996).
- [39] "Self-starting soliton modelocked Ti-sapphire laser using a thin semiconductor saturable absorber," *Electronics Letters* [31, 287](#) (1995).
- [40] S. Tsuda, W. H. Knox, E. a. de Souza, W. Y. Jan, and J. E. Cunningham, "Low-loss intracavity AlAs/AlGaAs saturable Bragg reflector for femtosecond mode locking in solid-state lasers." *Optics letters* [20, 1406-1408](#) (1995).
- [41] S. Tsuda, W. Knox, S. Cundiff, W. Jan, and J. Cunningham, "Mode-locking ultrafast solid-state lasers with saturable Bragg reflectors," *IEEE Journal of Selected Topics in Quantum Electronics* [2, 454-464](#) (1996).
- [42] U. Keller, "Recent developments in compact ultrafast lasers." *Nature* [424, 831-838](#) (2003).
- [43] G. Spuhler, R. Paschotta, D. Sutter, N. Matuschek, U. Keller, M. Moser, R. Hovel, V. Scheuer, G. Angelow, and T. Tschudi, "Double-chirped semiconductor mirrors for dispersion compensation in femtosecond lasers," *Technical Digest. Summaries of papers presented at the Conference on Lasers and Electro-Optics. Postconference Edition. CLEO '99. Conference on Lasers and Electro-Optics (IEEE Cat. No.99CH37013)* [2166](#) (1999).

- [44] F. X. Kaertner, L. R. Brovelli, D. Kopf, M. Kamp, I. G. Calasso, and U. Keller, "Control of solid state laser dynamics by semiconductor devices," *Optical Engineering* **34**, 2024-2036 (1995).
- [45] G. J. Spühler, K. J. Weingarten, R. Grange, L. Krainer, M. Haiml, V. Liverini, M. Golling, S. Schön, and U. Keller, "Semiconductor saturable absorber mirror structures with low saturation fluence," *Applied Physics B* **81**, 27-32 (2005).
- [46] C. Hönniger, R. Paschotta, F. Morier-Genoud, M. Moser, and U. Keller, "Q-switching stability limits of continuous-wave passive mode locking," *J. Opt. Soc. Am. B* **16**, 46-56 (1999).
- [47] I. Hartl, H. A. McKay, R. Thapa, B. K. Thomas, A. Ruehl, L. Dong, and M. E. Fermann, "Fully stabilized GHz Yb-fiber laser frequency comb," in "Advanced Solid-State Photonics," (Optical Society of America, 2009), p. MF9.
- [48] S. Pekarek, C. Fiebig, M. C. Stumpf, A. E. H. Oehler, K. Paschke, G. Erbert, T. Südmeyer, and U. Keller, "Diode-pumped gigahertz femtosecond Yb:KGW laser with a peak power of 3.9 kW," *Optics Express* **18**, 16320-16326 (2010).
- [49] D. Li, U. Demirbas, J. R. Birge, G. S. Petrich, L. A. Kolodziejski, A. Sennaroglu, F. X. Kärtner, and J. G. Fujimoto, "Diode-pumped passively mode-locked GHz femtosecond Cr:LiSAF laser with kW peak power," *Optics Letters* **35**, 1446-1448 (2010).
- [50] H. Chen, G. Chang, S. Xu, Z. Yang, and F. Kärtner, "3 GHz, fundamentally mode-locked, femtosecond Yb-fiber laser," *Optics letters* **37**, 3522-3524 (2012).
- [51] Y.-C. Chen, N. R. Raravikar, L. S. Schadler, P. M. Ajayan, Y.-P. Zhao, T.-M. Lu, G.-C. Wang, and X.-C. Zhang, "Ultrafast optical switching properties of single-wall carbon nanotube polymer composites at 1.55  $\mu\text{m}$ ," *Applied Physics Letters* **81**, 975-977 (2002).
- [52] J.-S. Lauret, C. Voisin, G. Cassabois, C. Delalande, P. Roussignol, O. Jost, and L. Capes, "Ultrafast carrier dynamics in single-wall carbon nanotubes," *Phys. Rev. Lett.* **90**, 057404 (2003).
- [53] S. Tatsuura, M. Furuki, Y. Sato, I. Iwasa, M. Tian, and H. Mitsu, "Semiconductor carbon nanotubes as ultrafast switching materials for optical telecommunications," *Advanced Materials* **15**, 534-537 (2003).
- [54] Y. Sakakibara, S. Tatsuura, H. Kataura, M. Tokumoto, and Y. Achiba, "Near-infrared saturable absorption of single-wall carbon nanotubes prepared by laser ablation method," *Japanese Journal of Applied Physics* **42**, L494 (2003).
- [55] T. Schibli, K. Minoshima, H. Kataura, E. Itoga, N. Minami, S. Kazaoui, K. Miyashita, M. Tokumoto, and Y. Sakakibara, "Ultrashort pulse-generation by saturable absorber mirrors based on polymer-embedded carbon nanotubes," *Opt. Express* **13**, 8025-8031 (2005).
- [56] K. Kieu and M. Mansuripur, "Femtosecond laser pulse generation with a fiber taper embedded in carbon nanotube/polymer composite," *Opt. Lett.* **32**, 2242-2244 (2007).
- [57] Q. Bao, H. Zhang, Y. Wang, Z. Ni, Y. Yan, Z. X. Shen, K. P. Loh, and D. Y. Tang, "Atomic-layer graphene as a saturable absorber for ultrafast pulsed lasers," *Advanced Functional Materials* **19**, 3077-3083 (2009).

- [58] P. R. Wallace, “The band theory of graphite,” *Phys. Rev.* **71**, 622–634 (1947).
- [59] A. H. Castro Neto, F. Guinea, N. M. R. Peres, K. S. Novoselov, and A. K. Geim, “The electronic properties of graphene,” *Rev. Mod. Phys.* **81**, 109–162 (2009).
- [60] H. Fang, H. a. Bechtel, E. Plis, M. C. Martin, S. Krishna, E. Yablonovitch, and A. Javey, “Quantum of optical absorption in two-dimensional semiconductors.” *Proceedings of the National Academy of Sciences of the United States of America* **110**, 11688–91 (2013).
- [61] T. Stauber, N. M. R. Peres, and A. K. Geim, “Optical conductivity of graphene in the visible region of the spectrum,” *Phys. Rev. B* **78**, 085432 (2008).
- [62] X. Li, W. Cai, J. An, S. Kim, J. Nah, D. Yang, R. Piner, A. Velamakanni, I. Jung, E. Tutuc, S. K. Banerjee, L. Colombo, and R. S. Ruoff, “Large-area synthesis of high-quality and uniform graphene films on copper foils,” *Science* **324**, 1312–1314 (2009).
- [63] X. Li, C. W. Magnuson, A. Venugopal, J. An, J. W. Suk, B. Han, M. Borysiak, W. Cai, A. Velamakanni, Y. Zhu, L. Fu, E. M. Vogel, E. Voelkl, L. Colombo, and R. S. Ruoff, “Graphene films with large domain size by a two-step chemical vapor deposition process,” *Nano Letters* **10**, 4328–4334 (2010).
- [64] M. Lafkioti, B. Krauss, T. Lohmann, U. Zschieschang, H. Klauk, K. v. Klitzing, and J. H. Smet, “Graphene on a hydrophobic substrate: Doping reduction and hysteresis suppression under ambient conditions,” *Nano Letters* **10**, 1149–1153 (2010). PMID: 20218633.
- [65] P. Joshi, H. E. Romero, A. T. Neal, V. K. Toutam, and S. A. Tadigadapa, “Intrinsic doping and gate hysteresis in graphene field effect devices fabricated on sio 2 substrates,” *Journal of Physics: Condensed Matter* **22**, 334214 (2010).
- [66] A. Kasry, M. A. Kuroda, G. J. Martyna, G. S. Tulevski, and A. A. Bol, “Chemical doping of large-area stacked graphene films for use as transparent, conducting electrodes,” *ACS Nano* **4**, 3839–3844 (2010).
- [67] K. S. Novoselov, A. K. Geim, S. V. Morozov, D. Jiang, Y. Zhang, S. V. Dubonos, I. V. Grigorieva, and A. A. Firsov, “Electric field effect in atomically thin carbon films,” *Science* **306**, 666–669 (2004).
- [68] D. J. Maas, B. Rudin, A.-R. Bellancourt, D. Iwaniuk, S. V. Marchese, T. Südmeier, and U. Keller, “High precision optical characterization of semiconductor saturable absorber mirrors,” *Opt. Express* **16**, 7571–7579 (2008).
- [69] J. M. Dawlaty, S. Shivaraman, M. Chandrashekhhar, F. Rana, and M. G. Spencer, “Measurement of ultrafast carrier dynamics in epitaxial graphene,” **92**, 042116 (2008).
- [70] H. Wang, J. H. Strait, P. A. George, S. Shivaraman, V. B. Shields, M. Chandrashekhhar, J. Hwang, F. Rana, M. G. Spencer, C. S. Ruiz-Vargas, and J. Park, “Ultrafast relaxation dynamics of hot optical phonons in graphene,” **96**, 081917 (2010).
- [71] M. Breusing, S. Kuehn, T. Winzer, E. Malić, F. Milde, N. Severin, J. P. Rabe, C. Ropers, A. Knorr, and T. Elsaesser, “Ultrafast nonequilibrium carrier dynamics in a single graphene layer,” *Phys. Rev. B* **83**, 153410 (2011).

- [72] G. Xing, H. Guo, X. Zhang, T. C. Sum, and C. H. A. Huan, “The physics of ultrafast saturable absorption in graphene,” *Opt. Express* **18**, 4564–4573 (2010).
- [73] M. Regmi, M. F. Chisholm, and G. Eres, “The effect of growth parameters on the intrinsic properties of large-area single layer graphene grown by chemical vapor deposition on Cu,” *Carbon* **50**, 134–141 (2012).
- [74] F. T. Vasko, “Saturation of interband absorption in graphene,” *Phys. Rev. B* **82**, 245422 (2010).
- [75] Z. Sun, T. Hasan, F. Torrisi, D. Popa, G. Privitera, F. Wang, F. Bonaccorso, D. M. Basko, and A. C. Ferrari, “Graphene mode-locked ultrafast laser,” *ACS Nano* **4**, 803–810 (2010). PMID: 20099874.
- [76] Q. Bao, H. Zhang, Z. Ni, Y. Wang, L. Polavarapu, Z. Shen, Q.-H. Xu, D. Tang, and K. Loh, “Monolayer graphene as a saturable absorber in a mode-locked laser,” *Nano Research* **4**, 297–307 (2011). 10.1007/s12274-010-0082-9.
- [77] Q. Bao, H. Zhang, J.-x. Yang, S. Wang, D. Y. Tang, R. Jose, S. Ramakrishna, C. T. Lim, and K. P. Loh, “Graphene-polymer nanofiber membrane for ultrafast photonics,” *Advanced Functional Materials* **20**, 782–791 (2010).
- [78] W. D. Tan, C. Y. Su, R. J. Knize, G. Q. Xie, L. J. Li, and D. Y. Tang, “Mode locking of ceramic Nd:yttrium aluminum garnet with graphene as a saturable absorber,” **96**, 031106 (2010).
- [79] H. Zhang, Q. Bao, D. Tang, L. Zhao, and K. Loh, “Large energy soliton erbium-doped fiber laser with a graphene-polymer composite mode locker,” **95**, 141103 (2009).
- [80] H. Zhang, D. Tang, R. J. Knize, L. Zhao, Q. Bao, and K. P. Loh, “Graphene mode locked, wavelength-tunable, dissipative soliton fiber laser,” **96**, 111112 (2010).
- [81] H. Zhang, D. Y. Tang, L. M. Zhao, Q. L. Bao, and K. P. Loh, “Large energy mode locking of an erbium-doped fiber laser with atomic layer graphene,” *Opt. Express* **17**, 17630–17635 (2009).
- [82] F. X. Kaertner, L. R. Brovelli, D. Kopf, M. Kamp, I. G. Calasso, and U. Keller, “Control of solid state laser dynamics by semiconductor devices,” **34**, 2024–2036 (1995).
- [83] T. R. Schibli, U. Morgner, and F. X. Kärtner, “Control of q-switched mode locking by active feedback,” *Opt. Lett.* **26**, 148–150 (2001).
- [84] N. Joly and S. Bielawski, “Suppression of q-switch instabilities by feedback control in passively mode-locked lasers,” *Opt. Lett.* **26**, 692–694 (2001).
- [85] F. Wang, Y. Zhang, C. Tian, C. Girit, A. Zettl, M. Crommie, and Y. R. Shen, “Gate-variable optical transitions in graphene,” *Science* **320**, 206–209 (2008).
- [86] K. S. Novoselov, D. Jiang, F. Schedin, T. J. Booth, V. V. Khotkevich, S. V. Morozov, and A. K. Geim, “Two-dimensional atomic crystals,” *Proceedings of the National Academy of Sciences of the United States of America* **102**, 10451–10453 (2005).

- [87] R. R. Nair, P. Blake, A. N. Grigorenko, K. S. Novoselov, T. J. Booth, T. Stauber, N. M. R. Peres, and A. K. Geim, “Fine structure constant defines visual transparency of graphene,” *Science* **320**, 1308 (2008).
- [88] K. F. Mak, M. Y. Sfeir, Y. Wu, C. H. Lui, J. A. Misewich, and T. F. Heinz, “Measurement of the optical conductivity of graphene,” *Phys. Rev. Lett.* **101**, 196405 (2008).
- [89] Z. Q. Li, E. a. Henriksen, Z. Jiang, Z. Hao, M. C. Martin, P. Kim, H. L. Stormer, and D. N. Basov, “Dirac charge dynamics in graphene by infrared spectroscopy,” *4*, 6–9 (2008).
- [90] M. Liu, X. Yin, E. Ulin-Avila, B. Geng, T. Zentgraf, L. Ju, F. Wang, and X. Zhang, “A graphene-based broadband optical modulator,” *Nature* **474**, 64–67 (2011).
- [91] N. Joly and S. Bielawski, “Suppression of q-switch instabilities by feedback control in passively mode-locked lasers,” *Opt. Lett.* **26**, 692–694 (2001).
- [92] X. Li, W. Cai, J. An, S. Kim, J. Nah, D. Yang, R. Piner, A. Velamakanni, I. Jung, E. Tutuc, S. K. Banerjee, L. Colombo, and R. S. Ruoff, “Large-area synthesis of high-quality and uniform graphene films on copper foils,” *Science* **324**, 1312–1314 (2009).
- [93] T. Wilken, M. Lezius, T. W. Hänsch, A. Kohfeldt, A. Wicht, V. Schkolnik, M. Krutzik, H. Duncker, O. Hellmig, P. Windpassinger, K. Sengstock, A. Peters, and R. Holzwarth, “A frequency comb and precision spectroscopy experiment in space,” in “CLEO: 2013,” (Optical Society of America, 2013), p. AF2H.5.
- [94] L. C. Sinclair, I. Coddington, W. C. Swann, G. B. Rieker, A. Hati, K. Iwakuni, and N. R. Newbury, “Operation of an optically coherent frequency comb outside the metrology lab,” *Opt. Express* **22**, 6996–7006 (2014).
- [95] C. Benko, A. Ruehl, M. J. Martin, K. S. E. Eikema, M. E. Fermann, I. Hartl, and J. Ye, “Full phase stabilization of a yb:fiber femtosecond frequency comb via high-bandwidth transducers,” *Opt. Lett.* **37**, 2196–2198 (2012).
- [96] C.-C. Lee, C. Mohr, J. Bethge, S. Suzuki, M. E. Fermann, I. Hartl, and T. R. Schibli, “Frequency comb stabilization with bandwidth beyond the limit of gain lifetime by an intracavity graphene electro-optic modulator,” *Opt. Lett.* **37**, 3084–3086 (2012).
- [97] M. Hoffmann, S. Schilt, and T. Südmeyer, “Ceo stabilization of a femtosecond laser using a sesam as fast opto-optical modulator,” *Opt. Express* **21**, 30054–30064 (2013).
- [98] R. J. Jones and J.-C. Diels, “Stabilization of femtosecond lasers for optical frequency metrology and direct optical to radio frequency synthesis,” *Phys. Rev. Lett.* **86**, 3288–3291 (2001).
- [99] S. Koke, C. Grebing, H. Frei, A. Anderson, A. Assion, and G. Steinmeyer, “Direct frequency comb synthesis with arbitrary offset and shot-noise-limited phase noise,” *Nature Photonics* **4**, 462–465 (2010).
- [100] D. Hudson, K. Holman, R. Jones, S. Cundiff, J. Ye, and D. Jones, “Mode-locked fiber laser frequency-controlled with an intracavity electro-optic modulator,” *Opt. Lett.* **30**, 2948–2950 (2005).

- [101] E. Baumann, F. R. Giorgetta, J. W. Nicholson, W. C. Swann, I. Coddington, and N. R. Newbury, “High-performance, vibration-immune, fiber-laser frequency comb,” *Opt. Lett.* **34**, 638–640 (2009).
- [102] Y. Nakajima, H. Inaba, K. Hosaka, K. Minoshima, A. Onae, M. Yasuda, T. Kohno, S. Kawato, T. Kobayashi, T. Katsuyama, and F.-L. Hong, “A multi-branch, fiber-based frequency comb with millihertz-level relative linewidths using an intra-cavity electro-optic modulator,” *Opt. Express* **18**, 1667–1676 (2010).
- [103] C.-C. Lee, S. Suzuki, W. Xie, and T. R. Schibli, “Broadband graphene electro-optic modulators with sub-wavelength thickness,” *Opt. Express* **20**, 5264–5269 (2012).
- [104] J. Bethge, J. Jiang, C. Mohr, M. Fermann, and I. Hartl, “Optically referenced tm-fiber-laser frequency comb,” in “Lasers, Sources, and Related Photonic Devices,” (Optical Society of America, 2012), p. AT5A.3.
- [105] J. Hall and M. Zhu, “An Introduction to phase stable optical sources,” in “Laser Manipulation of Atoms and Ions/Manipolazione Col Laser Di Atomi E Ioni (Proceedings of the International School of Physics), Enrico Fermi Course CXVIII.”, (1992).
- [106] I. Hartl, L. Dong, M. E. Fermann, T. R. Schibli, A. Onae, F. L. Hong, H. Inaba, K. Minoshima, and H. Matsumoto, “Fiber based frequency comb lasers and their applications,” in “Advanced Solid-State Photonics,” (Optical Society of America, 2005), p. WE4.
- [107] J. Jiang, C. Mohr, J. Bethge, A. Mills, W. Mefford, I. Hartl, M. E. Fermann, C.-C. Lee, S. Suzuki, T. R. Schibli, N. Leindecker, K. L. Vodopyanov, and P. G. Schunemann, “500 mhz, 58fs highly coherent tm fiber soliton laser,” in “Conference on Lasers and Electro-Optics 2012,” (Optical Society of America, 2012), p. CTh5D.7.
- [108] J. J. M. C. S. T. R. Kuse N, Lee C.-C. and F. M. E., “Ultra-low noise er frequency combs,” (2015 Joint Conference of the IEEE International Frequency Control Symposium & European Frequency and Time Forum, 2015).
- [109] D. J. Jones, S. A. Diddams, J. K. Ranka, A. Stentz, R. S. Windeler, J. L. Hall, and S. T. Cundiff, “Carrier-envelope phase control of femtosecond mode-locked lasers and direct optical frequency synthesis,” *Science* **288**, 635–639 (2000).
- [110] R. Holzwarth, T. Udem, T. W. Hänsch, J. C. Knight, W. J. Wadsworth, and P. S. J. Russell, “Optical frequency synthesizer for precision spectroscopy,” *Phys. Rev. Lett.* **85**, 2264–2267 (2000).
- [111] N. Newbury, “Searching for applications with a fine-tooth comb,” *Nature Photonics* **5**, 186–188 (2011).
- [112] A. J. Benedick, J. G. Fujimoto, and F. X. Kärtner, “Optical flywheels with attosecond jitter,” *Nature Photonics* **6**, 97–100 (2012).
- [113] L. F. Mollenauer and R. H. Stolen, “The soliton laser,” *Opt. Lett.* **9**, 13–15 (1984).
- [114] F. M. Mitschke and L. F. Mollenauer, “Ultrashort pulses from the soliton laser,” *Opt. Lett.* **12**, 407–409 (1987).



- [115] J. D. Kafka, D. W. Hall, and T. Baer, "Mode-locked erbium-doped fiber laser with soliton pulse shaping," *Opt. Lett.* **14**, 1269–1271 (1989).
- [116] H.-W. Chen, G. Chang, S. Xu, Z. Yang, and F. X. Kärtner, "3ghz, fundamentally mode-locked, femtosecond Yb-fiber laser," *Opt. Lett.* **37**, 3522–3524 (2012).
- [117] A. Bartels, D. Heinecke, and S. A. Diddams, "10-GHz self-referenced optical frequency comb," *Science* **326**, 681 (2009).
- [118] M. Endo, A. Ozawa, and Y. Kobayashi, "Kerr-lens mode-locked yb:kyw laser at 4.6-GHz repetition rate," *Opt. Express* **20**, 12191–12197 (2012).
- [119] S. Pekarek, A. Klenner, T. Südmeyer, C. Fiebig, K. Paschke, G. Erbert, and U. Keller, "Femtosecond diode-pumped solid-state laser with a repetition rate of 4.8 ghz," *Opt. Express* **20**, 4248–4253 (2012).
- [120] H. Haus and A. Mecozzi, "Noise of mode-locked lasers," *Quantum Electronics, IEEE Journal of* **29**, 983–996 (1993).
- [121] S. Kelly, "Characteristic sideband instability of periodically amplified average soliton," *Electronics Letters* **28**, 806–807 (1992).
- [122] M. Katz, O. Gat, and B. Fischer, "Noise-induced oscillations in fluctuations of passively mode-locked pulses," *Opt. Lett.* **35**, 297–299 (2010).
- [123] I. Hartl, A. Romann, T. R. Schibli, and M. E. Fermann, "Pulse train amplitude modulation due to continuum resonances in GHz soliton fiber lasers," in "CLEO/Europe and EQEC 2011 Conference Digest," (Optical Society of America, 2011), p. CF2\_3.
- [124] H. A. Haus, W. S. Wong, and F. I. Khatri, "Continuum generation by perturbation of soliton," *J. Opt. Soc. Am. B* **14**, 304–313 (1997).
- [125] S. Taccheo, P. Laporta, O. Svelto, and G. De Geronimo, "Theoretical and experimental analysis of intensity noise in a codoped erbium-ytterbium glass laser," *Applied Physics B* **66**, 19–26 (1998).
- [126] H. A. Haus, J. D. Moores, and L. E. Nelson, "Effect of third-order dispersion on passive mode locking," *Opt. Lett.* **18**, 51–53 (1993).
- [127] C. Berger, Z. Song, X. Li, X. Wu, N. Brown, C. Naud, D. Mayou, T. Li, J. Hass, A. N. Marchenkov, E. H. Conrad, P. N. First, and W. A. de Heer, "Electronic confinement and coherence in patterned epitaxial graphene," *Science* **312**, 1191–1196 (2006).
- [128] K. V. Emtsev, A. Bostwick, K. Horn, J. Jobst, G. L. Kellogg, L. Ley, J. L. McChesney, T. Ohta, S. A. Reshanov, J. Röhrli, E. Rotenberg, A. K. Schmid, D. Waldmann, H. B. Weber, and T. Seyller, "Towards wafer-size graphene layers by atmospheric pressure graphitization of silicon carbide." *Nature materials* **8**, 203–207 (2009).
- [129] Q. Yu, J. Lian, S. Siriponglert, H. Li, Y. P. Chen, and S.-S. Pei, "Graphene segregated on ni surfaces and transferred to insulators," *Applied Physics Letters* **93**, - (2008).

- [130] A. Reina, X. Jia, J. Ho, D. Nezich, H. Son, V. Bulovic, M. S. Dresselhaus, and J. Kong, "Large area, few-layer graphene films on arbitrary substrates by chemical vapor deposition," *Nano Letters* **9**, 30-35 (2009). PMID: 19046078.
- [131] I. Vlassiounk, M. Regmi, P. Fulvio, S. Dai, P. Datskos, G. Eres, and S. Smirnov, "Role of hydrogen in chemical vapor deposition growth of large single-crystal graphene," *ACS Nano* **5**, 6069-6076 (2011). PMID: 21707037.
- [132] L. Gao, W. Ren, J. Zhao, L.-P. Ma, Z. Chen, and H.-M. Cheng, "Efficient growth of high-quality graphene films on cu foils by ambient pressure chemical vapor deposition," *Applied Physics Letters* **97**, - (2010).
- [133] S. Bhaviripudi, X. Jia, M. S. Dresselhaus, and J. Kong, "Role of kinetic factors in chemical vapor deposition synthesis of uniform large area graphene using copper catalyst," *Nano Letters* **10**, 4128-4133 (2010). PMID: 20812667.
- [134] A. C. Ferrari, J. C. Meyer, V. Scardaci, C. Casiraghi, M. Lazzeri, F. Mauri, S. Piscanec, D. Jiang, K. S. Novoselov, S. Roth, and A. K. Geim, "Raman Spectrum of Graphene and Graphene Layers," *Physical Review Letters* **97**, 187401 (2006).
- [135] L. M. Malard, M. a. Pimenta, G. Dresselhaus, and M. S. Dresselhaus, "Raman spectroscopy in graphene," *Physics Reports* **473**, 51-87 (2009).
- [136] G. F. Dresselhaus, M. Dresselhaus, A. Jorio, and R. Saito, Raman Spectroscopy in Graphene Related Systems (2011).
- [137] A. C. Ferrari, "Raman spectroscopy of graphene and graphite: Disorder, electronphonon coupling, doping and nonadiabatic effects," *Solid State Communications* **143**, 47 - 57 (2007). Exploring graphene Recent research advances.
- [138] B. Krauss, T. Lohmann, D.-H. Chae, M. Haluska, K. von Klitzing, and J. H. Smet, "Laser-induced disassembly of a graphene single crystal into a nanocrystalline network," *Phys. Rev. B* **79**, 165428 (2009).
- [139] A. Das, S. Pisana, B. Chakraborty, S. Piscanec, S. K. Saha, U. V. Waghmare, K. S. Novoselov, H. R. Krishnamurthy, A. K. Geim, A. C. Ferrari, and A. K. Sood, "Monitoring dopants by Raman scattering in an electrochemically top-gated graphene transistor." *Nature nanotechnology* **3**, 210-215 (2008).
- [140] J. Yan, Y. Zhang, P. Kim, and A. Pinczuk, "Electric field effect tuning of electron-phonon coupling in graphene," *Phys. Rev. Lett.* **98**, 166802 (2007).
- [141] X. Dong, D. Fu, W. Fang, Y. Shi, P. Chen, and L. J. Li, "Doping single-layer graphene with aromatic molecules," *Small* **5**, 1422-1426 (2009).



## Appendix A

### Chemical vapor deposition of graphene

Monolayer graphene was first shown to stably exist in ambient environment by Novoselov et al. [86]. It was isolated from graphite by mechanical exfoliation. Although close to pristine quality can be achieved in exfoliated samples, it is nearly impossible to fabricate useful optical devices due to the small area of exfoliated sample (typically limited to  $\sim 1000 \mu\text{m}^2$ ). Large-area graphene can be obtained by thermal decomposition of SiC at an elevated temperature [127, 128]. While devices can be directly fabricated on SiC wafers, transferring graphene to suitable optical substrates has been difficult, if not impossible. On metals such as nickel, it has been demonstrated that carbon originally dissolved in the metal at high temperature can precipitate on the surface and form graphene when cooled. This process usually yields multilayer unless special attention is paid to the cooling process. [129, 130].

It was demonstrated by Li et al. [92] that monolayer graphene can be deposited by chemical vapor deposition (CVD) as in the case of nickel. However, the growth on copper foil results in a large coverage (more than 95% of the area) of monolayer graphene, likely due to the low solubility of carbon in copper. The grown graphene can then be easily transferred (also demonstrated in [92]) to almost any substrates that have proper adhesion to graphene such as glass or silicon wafers. Adhesion can be further improved by annealing the sample at raised temperature under vacuum or inert gas.

A conceptual diagram of CVD setup used in this Thesis is shown in Fig. A.1. High-purity gases (99.999%) are regulated independently and fed into a quartz (1 inch diameter) tube, which

is placed in a tube furnace. The pipelines are all stainless steel, and the gas regulators are metal sealed in order to avoid any hydrocarbon contamination in the upper stream. The downstream of the quartz tube is connected to a two-stage pump (turbo and dry scroll, base pressure  $< 1 \mu\text{Torr}$ ). All regulators are controlled by a programmed microcontroller. A motor that pulls the furnace away from the sample's location allows an automated quick cooling process. Both the motor and the vacuum pump are also controlled by the microcontroller, which received growth parameter from the PC. Copper foil samples are loaded on an inner tube, which has a slightly smaller diameter than 1 inch and can slide into the outer tube.

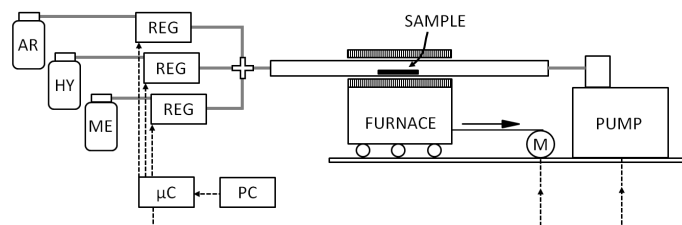


Figure A.1: Chemical vapor deposition system for growing monolayer graphene. AR: argon, HY: hydrogen, ME: methane, REG: gas regulator,  $\mu\text{C}$ : microcontroller, PC: personal computer for recipe entering and saving, M: motor for pulling furnace to cool the sample after growth, PUMP: vacuum pump, consisting of a turbo pump backed with a oil-free membrane pump.

A typical CVD growth process used in this Thesis is described in detail in the following.

- (1) Prepare a piece of copper foil (Alfa Aesar #13382,  $25 \mu\text{m}$  thick) that fits in the inner growth tube: To make the wet transfer process after growth less susceptible to failure, the foil should be reasonably flat and free of wrinkles. The copper foil should also be free of any protective coatings.
- (2) Heat up and anneal the copper foil under low flow of hydrogen: This step removes the copper oxide efficiently. Heating up to  $1000^\circ\text{C}$  usually takes about 70 minutes in our furnace. The pressure is typically in the 10 mTorr range (5 sccm of hydrogen). After the furnace reaches  $1000^\circ\text{C}$ , the copper foil is annealed for another 30 minutes. This generally increases the copper domain size.

- (3) Start the growth by flowing methane: to achieve large crystalline domains, a 1:1 ratio of hydrogen to methane flow (1 sccm) is employed. This results in low density of nucleation sites. Hydrogen also etches the boundary of graphene, causing the shape of graphene to approach hexagons, which is regarded as a sign for single-crystalline domains [131]. Depending on the gas flow rate and temperature, the time it takes to obtain full coverage of copper foil with graphene can vary substantially (1 minute to 4 hours). A second growth step with a higher methane flow (10 sccm) can be employed to speed up the nucleation rate after large domains are obtained [63].
- (4) Cooling the sample: due to carbon's low solubility in the copper foil, cooling rate does not seem to have effects on the precipitation of carbon on the copper surface, which may form multilayer graphene as in the case of nickel. We typically move the tube furnace out right after the growth is finished. The sample can be cooled down to room temperature in about an hour.

The CVD growth process mentioned above is performed using a vacuum pump, which can reach a base pressure of less than  $1\mu\text{Torr}$ . Typical pressure during growth and anneal phase is around 10 mTorr, depending on the gas flow rate. CVD can also be performed under ambient pressure, removing the need of a vacuum pump, but usually a high hydrogen flow or buffer gas such as argon is required [132, 133].

## Appendix B

### Raman spectra of graphene

In addition to optical absorption measurements, we examined the number of layers and defects of our graphene samples by their Raman spectra, which has been extensively studied and an invaluable tool in graphene research since the first isolation of monolayer graphene from graphite [134]. In the chemical doping experiment described in Chapter 3, we used Raman spectroscopy to confirm that chemical doping of graphene by nitric acid did not introduce defects. The interested reader may refer to [135–137] for detailed reviews in the field of Raman spectroscopy of graphene. Here a brief summary of graphene’s Raman spectrum is provided in Figure B.1.

Our measurements were performed on a home-built Raman microscope in epi-illumination and detection geometry, with excitation provided by a 633 nm HeNe laser (spot size  $\approx 1 \mu\text{m}$ , peak power  $< 1 \text{ kW/cm}^2$ ). The Raman scattered light is spectrally filtered with a  $160 \text{ cm}^{-1}$  cut-off filter (Semrock, LP02-633RU-25) and detected with a spectrometer with a 1200 g/mm (Newport, 53\*-220H) grating for single-peak measurements or a 600 g/mm grating (Newport, 53\*-350R) for measurements spanning the full relevant spectrum of graphene, and a liquid-nitrogen-cooled CCD camera (Princeton Instruments, Spec-10 2KB/LN).

The Raman spectrum of each sample was taken at five random locations. Peak positions and relative intensities were then extracted by fitting each peak to a Lorentzian distribution. We took the average of these values, combined with the statistical uncertainty of our spectrometer ( $< 2 \text{ nm}$ ) to attain mean peak positions and relative intensities and uncertainties. The statistical uncertainty is likely due to the spatial variation in doping concentration.

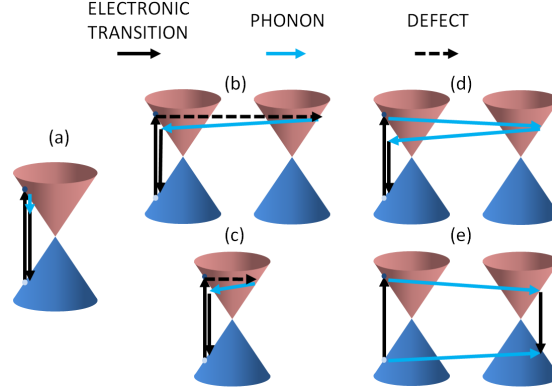


Figure B.1: (a) G peak ( $1582 \text{ cm}^{-1}$ ), originating from the vibration of one of the sublattices against the other one. This is the only first-order Raman process. (b) D peak, which is a second-order process and most importantly a signature of lattice defects. This occurs when the electron undergoes an elastic scattering due to a lattice defect (from  $K$  to  $K'$ ) followed by the emission of a phonon. (c) D' peak, similar to D but much weaker. The transition occurs within the same Dirac cone. (d) Double degenerate G' (or 2D) peak. This occurs by emitting two phonons. Thus, the frequency is about twice the frequency of D peak. (e) Triple degenerate G' (or 2D) peak. In monolayer graphene, this process is especially pronounced, even though it is a second-order process, because of its linear energy-momentum relation. Figure adapted from [135].

The peak power was kept low so as not to damage the sample or remove dopants with thermal effects [138]. To confirm that our measurements were non-intrusive, a short measurement ( $< 10$  seconds) was made before and after the longer (60–300 seconds), higher SNR, measurements to confirm no change in the spectrum.

Fig. B.2 shows the Raman spectra of our graphene samples. The undoped, only baked sample showed low  $I(D)/I(G)$  ratio ( $< 0.1$ ) and single Lorentzian 2D peak with a FWHM of  $35 \pm 3.5 \text{ cm}^{-1}$ . This suggests that our CVD-grown graphene is mostly defect-free and monolayer [134]. Our nitric-acid-doped graphene showed an upshift in the G band of  $5 \pm 3 \text{ cm}^{-1}$  and the 2D band of  $4 \pm 2 \text{ cm}^{-1}$ , a peak narrowing in the FWHM of the G band of between 2 and  $5 \text{ cm}^{-1}$ , and a decrease in the ratio  $I(2D)/I(G)$  from  $2 \pm 0.1$  to about  $1.6 \pm 0.3$  (from sample-a to sample-b). This agrees qualitatively with Raman measurements made on electrostatically doped graphene [139, 140] and graphene doped by organic molecules [141], although the G peak narrowing has not always been observed in chemically doped graphene.

As we increased level of p-doping to  $-400 \text{ meV}$  (sample-c), the G and 2D bands down-shifted

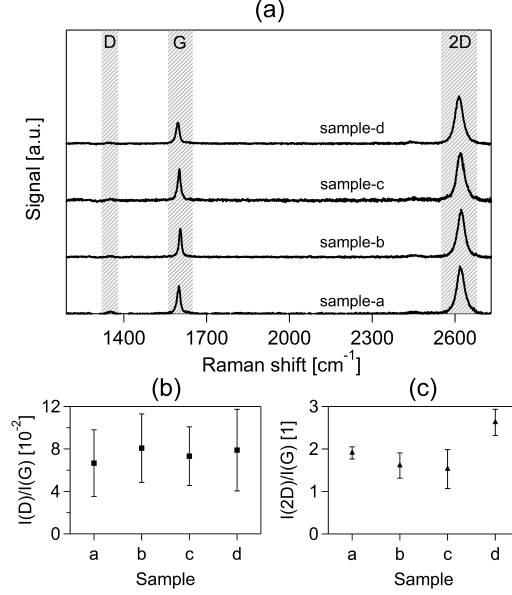


Figure B.2: (a) Representative Raman spectra of graphene samples used in the experiments. Sample-a: baked sample,  $E_F < 200$  meV; sample-b: doped sample,  $E_F \approx 200$  meV; sample-c: doped,  $E_F \approx 400$  meV; sample-d: baked after doped to  $E_F \approx 400$  meV. No significant changes of  $I(2\text{D})/I(\text{G})$  and  $I(\text{D})/I(\text{G})$  ratios were observed in samples-b,c,d, implying that nitric acid did not attack graphene and was removed by baking without damaging graphene. (b) All samples have small  $I(\text{D})/I(\text{G})$  ratios, which implies nearly defect-free graphene. (c) All samples have a  $I(2\text{D})/I(\text{G})$  ratio of about 2.

about halfway towards their original positions, which, to our knowledge, has not been observed in chemically doped graphene. However, doping graphene with nitric acid has not before been carefully studied, and the  $I(2\text{D})/I(\text{G})$  ratio, suggested to be an important measure of doping level, continued to decrease to about 1.5 as expected. We found no correlation between doping concentration and the  $I(\text{D})/I(\text{G})$  ratio, which is indicative of defects in graphene. We never found a mean  $I(\text{D})/I(\text{G})$  peak ratio above 0.12, and it should be noted that  $I(\text{D})$  was intentionally over-estimated because of the background noise. When we later baked our samples at  $100^\circ\text{C}$  for 1 hour to remove the adsorbants (sample-d), we found that the peak positions fully recovered and, in fact, downshifted by an additional  $2 \pm 2 \text{ cm}^{-1}$  for the 2D band and an additional  $1.3 \pm 0.7 \text{ cm}^{-1}$  for the G band. Furthermore, the  $I(2\text{D})/I(\text{G})$  peak ratio increased to about  $2.6 \pm 0.3$ . All of these changes after baking imply pristine graphene. It is likely that baking after doping removed the adsorbates that had accumulated on the graphene sheet in the time between initial sample preparation of the

undoped sample and its measurement in Raman. This would account for the seeming increase in purity after doping and baking.